6-1-2005

Experimental Investigation into the Aerodynamic Ground Effect of a Tailless Chevron-shaped UCAV

Brett L. Jones

EXPERIMENTAL INVESTIGATION INTO THE AERODYNAMIC GROUND EFFECT OF A TAILLESS CHEVRON-SHAPED UCAV

THESIS

Brett L. Jones, Ensign, USNR

AFIT/GAE/ENY/05-J04

DEPARTMENT OF THE AIR FORCE
AIR UNIVERSITY

AIR FORCE INSTITUTE OF TECHNOLOGY

Wright-Patterson Air Force Base, Ohio

AFIT/GAE/ENY/05-J04

EXPERIMENTAL INVESTIGATION INTO THE AERODYNAMIC GROUND
EFFECT OF A TAILLESS CHEVRON-SHAPED UCAV

THESIS

Presented to the Faculty

Department of Aeronautics and Astronautics

Graduate School of Engineering and Management

Air Force Institute of Technology

Air University

Air Education and Training Command

In Partial Fulfillment of the Requirements for the

Degree of Master of Science in Aeronautical Engineering

Brett L. Jones, BSE

Ensign, USNR

June 2005

AFIT/GAE/ENY/05-J04

EXPERIMENTAL INVESTIGATION INTO THE AERODYNAMIC GROUND
EFFECT OF A TAILLESS CHEVRON-SHAPED UCAV

Brett L. Jones, BSE
Ensign, USNR

Approved:

/signed/

_____   _____
Dr. Milton E. Franke (Chairman)   date

/signed/

_____   _____
Dr. Mark F. Reeder (Member)   date

/signed/

_____   _____
Lt Col Eric J. Stephen (Member)   date

AFIT/GAE/ENY/05-J04

Abstract

This experimental study adequately identified the ground effect region of an
unmanned combat air vehicle (UCAV). The AFIT 3' x 3' low-speed wind tunnel and a
ground plane were used to simulate the forces and moments on a UCAV model in ground
effect. The chevron planform used in this study was originally tested for stability and
control and the following extends the already existing database to incude ground effects.
The ground plane was a flat plate mounted with cylindrindrical legs. To expand the
capabilities of the AFIT 3' x 3' low-speed wind tunnel, hot-wire measurements and flow
visualization revealed an adequate testing environment for the use of the ground plane.

Examination of the flow through the test section indicated a significant difference
in test section transducer velocity and the hot-wire measured velocity. This disparity,
along with the velocity difference due to the ground plane, was accounted for as wind
tunnel blockage. In addition, the flow visualization revealed the horseshoe vortices that
built up on the front two mounted legs of the ground plane.

The ground effect region for the chevron UCAV was characterized by an increase
in lift, drag, and a decrease in lift-to-drag ratio. Previous studies of similar aspect ratio
and wing sweep noted these trends as well.

AFIT/GAE/ENY/05-J04

To my parents and sister for their love and support in every endeavor of my life and to my girlfriend for her patience and encouragement throughout this entire project.

Acknowledgements

I would like to thank the Air Vehicles Directorate of the Air Force Research Lab for their support and resources for this project. Also, I would like to thank my thesis advisor, Dr. Franke for his insightfulness and vast amount of experience. I would also like to express my sincere gratitude to Dwight Gehring, AFIT/ENY, and Jon Geiger, AFRL/VAAI, for their work. Mr. Gehring helped immensely with the set-up, calibration, and operation of the wind tunnel. Mr. Geiger is responsible for the Solid Works$^{©}$ drawings and coordinating the ground plane construction. Additionally, Randy Miller deserves the credit for the set-up and operation of the ENY rapid prototyping machine and Vincent Parisi, AFRL/HECV, for his assistance with the 3-D digitizing. I want to thank Dr. Reeder for taking the time out of his schedule to help me while in the tunnel along with LtCol Stephen, USAF, for helping me with the analysis and writing the vortex panel code. Lastly, I want to thank my Lord God for His strength and focus, without which, I would not have completed this project.

Brett L. Jones

Table of Contents

List of Figures

List of Tables

List of Symbols

Symbol	Name
a	Speed of Sound
A	Axial Force (Body Axis)
A_1	Balance Axial Sensor
AR	Aspect Ratio
b	Wing Span
C	Tunnel Test Area
$\bar{c}$	Wing Mean Chord
C_D	Drag Force Coefficient
CG	Center of Gravity
C_L	Lift Coefficient
$C_{L\alpha}$	Lift Curve Slope
C_m	Pitch Moment Coefficient
C_P	Pressure Coefficient
c_r	Wing Root Chord
D	Drag Force (Wind Axis)
e	Oswald's Efficiency Factor
h	Height Above Ground
k	Induced Drag Constant
L	Lift Force (Wind Axis)
ℓ_1	Balance Roll Moment Sensor
ℓ	Roll Moment
lb_f	Pounds Force
L/D	Lift-to-Drag Ratio
M	Mach Number
$\boldsymbol{m}$	Pitch Moment
N	Normal Force (Body Axis)
N_1 & N_2	Balance Normal Sensors
P	Test Room Pressure
q_∞	Free Stream Dynamic Pressure
R	Ideal Gas Constant
Re	Reynolds Number
S*	Side Force (Wind Axis)
S	Wing Area
S_1 & S_2	Balance Side Sensors
T	Test Room Temperature
U	Boundary Layer Velocity
U_∞	Free Stream Velocity
UCAV	Unmanned Combat Air Vehicle
Y	Side Force (Body Axis)
α, AOA	Angle of Attack ($\alpha = \theta$)
γ	Ratio of Specific Heats (c_p / c_T)
δ*	Displacement Thickness

δ_{lam}	Laminar Boundary Layer Thickness
δ_{turb}	Turbulent Boundary Layer Thickness
μ	Air Viscosity
ρ	Air Density
ϕ	Induced Drag Factor
ψ	Yaw Angle

EXPERIMENTAL INVESTIGATION INTO THE AERODYNAMIC GROUND
EFFECT OF A TAILLESS CHEVRON-SHAPED UCAV

I. Introduction

Section 1 – Ground Effect

Ever since the early days of aviation, pilots have experienced a phenomenon

while operating an aircraft very close to the ground. Either during take-off or landing,

any air vehicle will experience improved efficiency near the ground in the form of

increased lift. However, this poses a problem because most aircraft are not designed for

this flight condition and therefore can behave very awkwardly.

A typical aircraft is in-ground-effect (IGE) when it is within one wingspan of the

ground (1). The amount of ground effect experienced by an aircraft is dependent on the

induced drag. When the height of an aircraft is below one wingspan of the ground, the

induced drag significantly decreases due to the wingtip vortices interacting with the

ground (1). During normal flight, wingtip vortices are cylindrical in shape, but while

interfering with the ground, they tend to flatten out which improves the effective

wingspan and aspect ratio. Since aspect ratio has a strong inverse effect on induced drag,

an aircraft flying very near the ground will experience a reduction in induced drag

reducing the total drag of the aircraft (1).

In addition to a reduction in drag, an increase in lift and pitching moment are

characteristics of an aircraft in ground effect. The increase in lift along with the

reduction of drag significantly increases the lift-to-drag ratio, which intuitively increases

1

the overall aircraft efficiency. The discovery of this improved efficiency led to the development of Wing-In-Ground vehicles (2).

Section 2 – Wing-In-Ground Vehicles

Wing-In-Ground (WIG) vehicles take advantage of all the benefits of ground effect because they are designed to operate at very low altitudes. As knowledge and technology improved during the 20th century, WIG vehicles increased in popularity and many thought they were the future of marine transportation.

In the 1960's, Russian scientist Rostislav Alexeiev led the development of WIG boats. With his background in hydrofoil ship design, Alexeiev's research led to the development of ekranoplans. ('skimmer' in English) The Soviet Union saw the military potential in these vessels, and so Alexeiev received practically unlimited funding for his then top-secret project (2). Only a few years later, in 1966, Alexeiev unveiled the KM Caspian Sea Monster, a 550-ton WIG vehicle designed heavy loading and fast transportation over water. The KM was far more advanced than the ekranoplans developed earlier by Alexeiev mainly because its weight was 100 times that of the heaviest ekranoplan at that time. Several other crafts were developed and built for the Russian Navy in the decades to follow, but in the late 1980's, funding was lost due to the fall of the Soviet Union and the end of the Cold War (2).
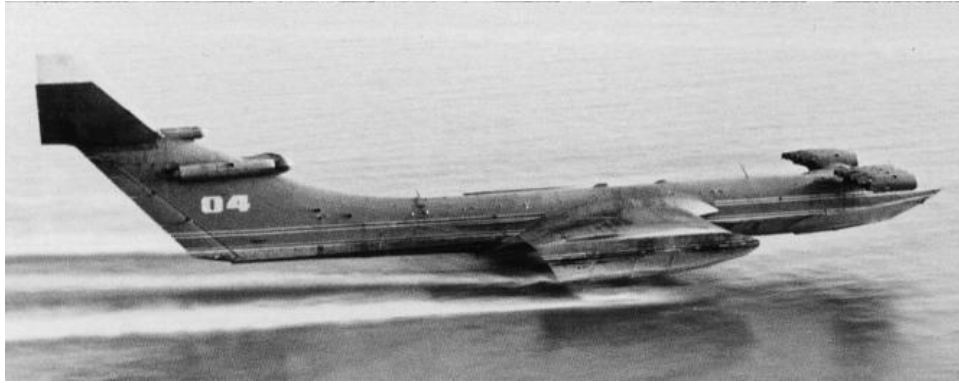
Figure 1: KM Caspian Sea Monster (2)

To meet the growing demands of the U.S. Army Mobility Command, Boeing

Phantom Works is evaluating a similar concept with the Pelican project. Like the

Russians concept of WIG vehicles, the Pelican would have twice the external dimensions

of the world's largest aircraft and would utilize ground effect to produce the necessary

lift-to-drag ratio for flight operations. It would have the cargo capacity to carry an entire

Army division of supplies and soldiers or up to 17 M-1 tanks (3). The WIG vehicle

concept could revolutionize marine transportation thanks to the beneficial effects of

flying low.

Section 3 – Unmanned Air Vehicles

Ever since the beginning of aviation, the concept of unmanned flight has intrigued

engineers and scientists. The first unmanned air vehicles (UAV) were built to be used as

guided missiles. The Kettering "Bug" and Sperry aerial torpedo were the first two

combat UAVs but were never used in operation due to inaccuracy. As technology

advanced, researchers investigated the use of radio and eventually television control links

to correct the erroneous navigation issues. During the last quarter-century, significant

advances in computing capabilities, electronics miniaturization, communications, guidance, navigation, and control have allowed for successful flight operations of the Global Hawk and Predator UAVs, which are currently being used daily in conflicts around the world (4).

The next development of unmanned flight is the unmanned combat air vehicle (UCAV). Currently, the primary program for UCAV exploration is the joint unmanned air systems (J-UCAS) program, which is a joint Darpa, Air Force, and Navy program. The J-UCAS program is designed to

> demonstrate the technical feasibility, military utility and operational value for a networked system of high performance, weaponized unmanned air vehicles to effectively and affordably prosecute 21st century combat missions, including Suppression of Enemy Air Defenses (SEAD), surveillance, and precision strike within the emerging global command and control architecture. (5)

The two leading UCAVs are the Boeing X-45 and the Northrop Grumman X-47. Each one has an unconventional configuration including a blended wing body with swept wings and no tail. Even though today's advanced control systems allow for such unconventional designs, the ground effect phenomenon still poses problems.

Section 4 – UAVs and Ground Effect

Understanding the location and the extent of the ground effect region is of particular interest for UAVs because of the shear fact that they are unmanned. Pilots use sight and feel when operating a conventional aircraft near the ground. During a landing, a pilot will normally flare the aircraft to ensure that the rear landing gear strikes first. If necessary, the pilot can make small adjustments to the aircraft attitude for the drag reduction and increase in lift while in the ground effect region. The pilot for a UAV

operates the craft from a Ground Control Station (GCS) and uses real time video and sensors. The removed operator or UAV pilot cannot feel the effects of the ground during take off and landing and depends entirely on the automatic control system. Therefore, it is important to identify the ground effect region in order to ensure safe flight. Normally, since the ground effect region is a small portion of time compared to the entire glide slope to land, it is not factored into the landing control system design. However, with sufficient data from flight tests or wind tunnel tests, the control engineer will make gain adjustments to account for the ground effect region (6).

Unmanned flight brought with it numerous mishaps near the ground. One of particular interest was on 22 April 1996, when the Lockheed Martin/Boeing RQ-3A DarkStar's fight control system did not properly account for ground effect. It 'porpoised' during take-off, pitched up, and stalled due to over-correction by ailerons (7).

Section 5 – Boeing AFRL/VAAA UCAV Program

In an effort to expand the database for unconventional aircrafts, Capt. Shad Reed of the Air Vehicles Directorate (VAAA) of the Air Force Research Laboratory (AFRL) conducted a low-speed wind tunnel investigation on three generic UCAV planforms. The test program defined the stability and control characteristics of moderately swept, low aspect ratio, tailless, blended wing body planforms. The three planforms tested were a chevron, lambda, and diamond shape. Their characteristics are found in reference (8). Of the three configurations tested, the chevron-shaped planform had the highest maximum lift coefficient, lift-to-drag ratio, and lowest minimum drag coefficient. However, due to the chevron planform's lack of fuselage, Reed concluded that subsystem

integration would be difficult since engines, weapons, and other components are normally located in the fuselage (8).

Despite Reed's conclusions about the possible subsystem integration problems of the chevron-shaped planform, a ground effects test is still of interest because improved technology can solve the apparent subsystem integration problems (8).

II. Literature Review

Section 1 – Ground Effect Theory

Since the beginning of flight, aircraft designers noticed the decrease in landing speed due to an increase in lift while in close proximity to the ground. Engineers conducted numerous wind tunnel and flight test experiments around the world in order to investigate this phenomenon called ground effect.

In 1922, Wieselsberger developed his famous theoretical equation for estimating the induced drag reduction of aircraft near the ground. He used Prandl's three-dimensional wing theory and the reflection method to establish a relatively simple relationship between height above ground and induced drag (9). His equation became the standard for predicting ground effect and was verified throughout the 1930s and 1940s in references 10-12, among others.

Another theoretical approach to estimating the decrease in induced drag due to the presence of the ground is to apply McCormick's induced drag factor. In his section on ground roll and takeoff distance, McCormick derived Equation [1] by replacing a rectangular wing with a simple horseshoe vortex modeled with its image so the vertical velocities cancel each other simulating the ground. The height was the distance between the reflection plane to the horseshoe vortices. McCormick then used the Biot-Savart Law to estimate the velocity induced at a point from each horseshoe vortex. This led him to identify a ratio between the induced drag in ground effect and the induced drag out-of-ground effect (13).

$$\phi = \frac{\left[16(h/b)\right]^2}{1+\left[16(h/b)\right]^2}$$ [1]

As discussed in Chapter I, ground effect is normally experienced at heights above ground less than one wingspan, and the effect is increased exponentially as the aircraft travels below half of a wingspan as demonstrated in references 17, 20, and 21. Equation [1], when when multiplied by the induced drag, provides a prediction for ground effect. Figure 2 is a plot of McCormick's induced drag factor.
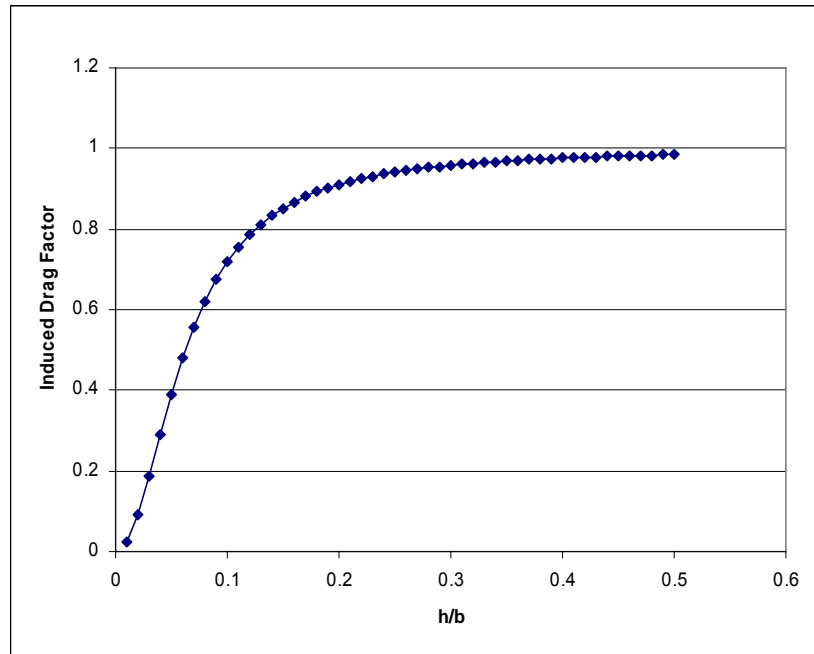

Figure 2: McCormick's Induced Drag Factor (13)

Section 2 – Static vs. Dynamic Wind Tunnel Testing

Experimental methods for ground effects have become more sophisticated during the past several decades. One of the first wind tunnel investigations was Raymond's

study at the Massachusetts Institute of Technology in 1921 (14). He analyzed ground effect by testing three different airfoils in a wind tunnel using a flat plate for a ground plane. He also attempted to create an imaginary ground plane by means of reflection. Both methods revealed similar results except at high angles of attack. This test confirmed that when near the ground, an airfoil will increase in lift and decrease in drag (14).

As testing techniques advanced, Raymond's flat plate method took the name of static wind tunnel testing. A static wind tunnel test involves a fixed ground plane height and model. Moving the model closer to the ground plane is normally how various heights above ground are tested. In order to validate these tests, test pilots flew ground effect testing routes, called 'fly-by' patterns. To determine the extent and location of the ground effect region, altitude and angle of attack were held constant. However, in 1967, William Schweikhard developed a method for measuring the ground effects of an aircraft as it approached a runway (15). A test pilot would maintain a constant angle of attack and power setting, but would let the sink rate vary; this ensured that lift, drag, and pitching moment were constant just before approaching the ground. Once in the ground effect region, flight test engineers measured any changes in flight path angle, velocity, or control surface deflection. They found that this flight test technique saved time and data analysis over standard fly-by or static tests (15).

In an effort to reduce flight test costs, engineers developed methods to dynamically test for ground effect in a wind tunnel. A dynamic wind tunnel test for ground effect attempts to better simulate a landing approach or a take off by manually or mechanically moving the model towards the ground plane. Chang et al. found relevance

9

in dynamic wind tunnel testing as he noted the disparity between static tests and landing data (16). He tested delta wings of 60, 70, and 75 deg sweep, the XB-70, and the F-104A both statically and dynamically. He, along with Baker et al., concluded that at heights of $h/b < 0.4$, the static wind tunnel results for the delta wings and XB-70 significantly over predicted the change in lift due to ground effect (17). However, he also pointed out that the amount of difference between static and dynamic results decreased as aspect-ratio increased. See Figure 3.
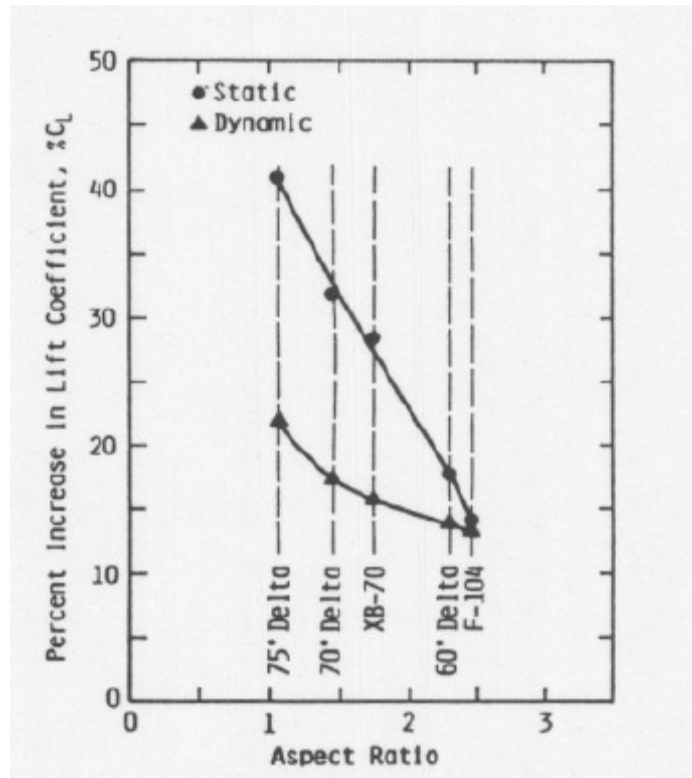

Figure 3: Incremental C_L vs. AR for static and dynamic ground effect at h/b=0.3 (17)

Additionally, Corda, et al. (18) performed a dynamic ground effect test on the F-15. Their results are mentioned because the chevron UCAV has a similar aspect ratio to that of the F-15. They fit the following equation to the dynamic ground effect tests for the delta wings presented in Figure 4:

10

$$\%\Delta C_{L,GE} = \left(\frac{0.2}{AR} + 0.04\right)*100 \qquad\qquad [2]$$

Equation [2] quanifies the relationship between percent increase in lift due to ground

effect and aspect ratio for a wing. Based on this prediction the chevron UCAV should

experience a 10.9% increase in lift due to ground effect.

More importantly, this relationship and results presented in Figure 4 suggest that a

staic ground effect test for the chevron UCAV should produce similar results as a

dynamic test.
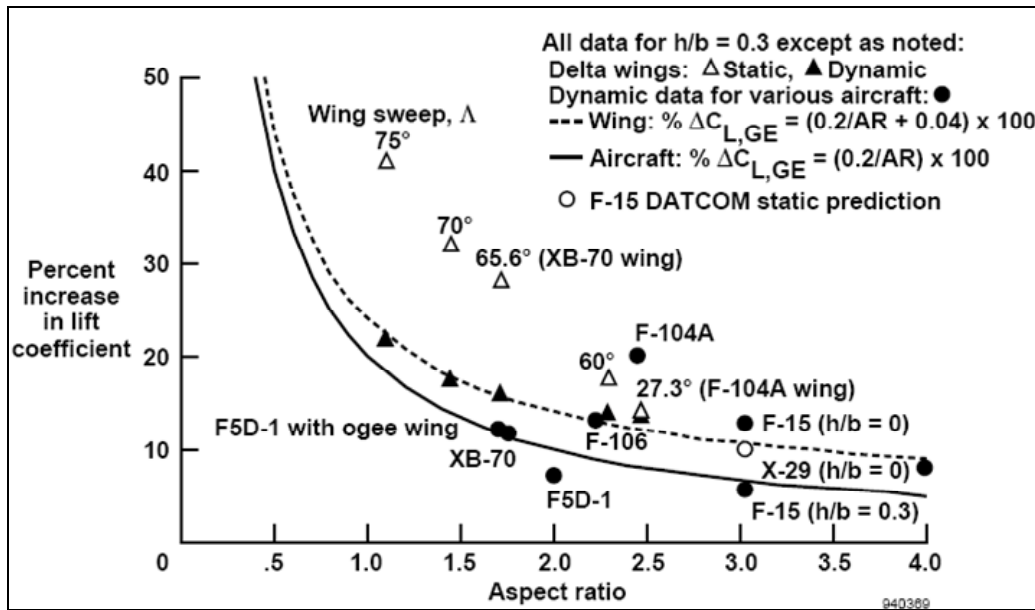
Figure 4: Percent Increase in C_L in Ground Effect vs. AR for Various Aircraft (18)

A common tool used to predict and verify ground effect tests is the U.S. Air Force

Data Compendium (DATCOM) (19). This analytical program uses equations, charts, and

flight data to predict stability and control characteristics of aircraft. Since the static

ground effect prediction for the F-15 lies almost directly on the curve based on dynamic

results for wings (Equation [2]), a static ground effect test for the chevron UCAV should produce similar results to that of a dynamic test.

Section 2.1 – Adverse Ground Effect

While ground effect is normally characterized by an increase in lift and a decrease in drag, not all aircraft configurations experience these beneficial traits. Lee, et al. (20) reported an increase in lift along with an increase in drag as height above ground decreased.

They performed dynamic and static wind tunnel tests on models of a 60 deg delta wing, F-106, and XB-70-1. Re was varied from $3x10^5$ to $7.5x10^5$ and height above ground ranged from h/b=1.6 to h/b=0.2 for all three models. Their focused primarily on the differences between the static and dynamic results, so no emphasis was placed on the increasing lift or drag. The C_D vs. (h/b) plot for the F-106 in Figure 5 represents their results.
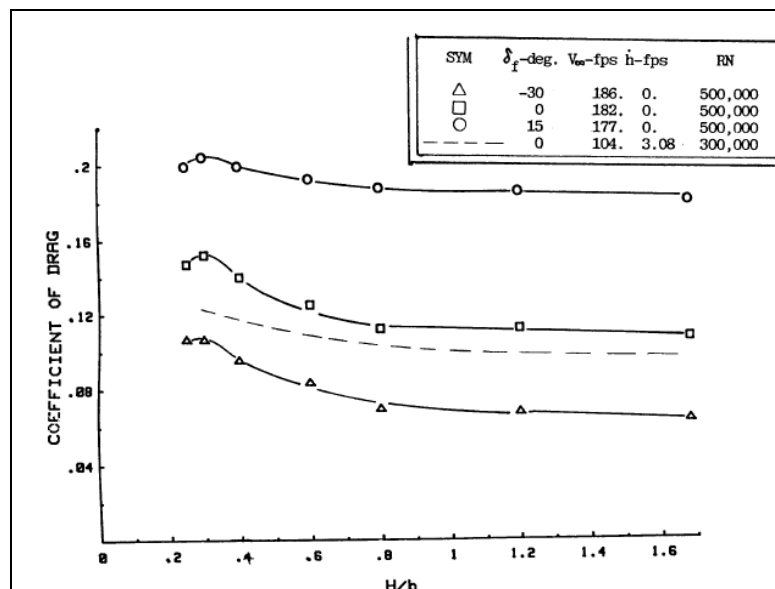

Figure 5: Adverse Ground Effect for the F-106 at an AOA = 14 deg (20)

12

Although Lee, et al. did not show any L/D results, the static data were extrapolated from their C_D vs. (h/b) plots (similar to Figure 5) and C_L vs. (h/b) for each model to analyze the trends. The 60 deg delta wing experienced a subtle decrease in L/D. The F-106 and XB-70-1 both experienced a decrease and a slight increase in L/D at the lowest height above ground. The downward trend of C_D between h/b=0.3 and 0.2 in Figure 5 was common for the XB-70-1 and explained the increase in L/D.

It is possible that aspect ratio and wing sweep played a role in these results. The 60 deg delta wing, F-106, and XB-70-1 had aspect ratios equal to 2.3, 2.4, and 1.78, respectfully. The F-106 had a wing sweep of 60 deg and the XB-70-1 had wing sweep of 65 deg. Again, these considerations were not discussed in their report, but are mentioned because the chevron UCAV has similar characteristics.

Similarly, the F-16 XL aircraft was flight tested and wind tunnel tested for ground effects by Curry (6). He found an increase in C_D as height above ground decreased and explained that an increase or a decrease in drag is possible for aircraft flying close to the ground. Curry and Owens (21) also discovered an increase in drag when the Tu-144 supersonic transporter flew in close proximity to the ground.

Section 3 – Boundary Layer Removal

One limitation using a ground plane in a wind tunnel to simulate ground effect is the boundary layer build-up across the top surface. Boundary layers form on any surface where a moving fluid has direct contact, so they cause an unrealistic test condition in

wind tunnels when a ground plane is used to simulate the ground. A boundary layer removal system is typically employed to resolve this issue.

One method of removing the boundary layer in a wind tunnel is to use a moving-belt ground plane. A moving-belt would better simulate an aircraft flying over the ground because the belt would spin at the same velocity of the air, which in turn removes the boundary layer.

While it seems that boundary layer removal with a moving-belt ground plane is essential to achieve proper flight dynamics, two different studies were conducted that showed the necessity of a moving-belt ground plane depends on the maximum lift coefficient of the air vehicle. Turner (22) investigated the use of conventional ground planes for ground effect wind tunnel testing. Specifically, he examined the possible use of endless-belt ground planes and determined the conditions under which it would be preferable. He concluded that the use of a moving-belt ground plane depended on spanwise lift coefficient and height above ground (22).
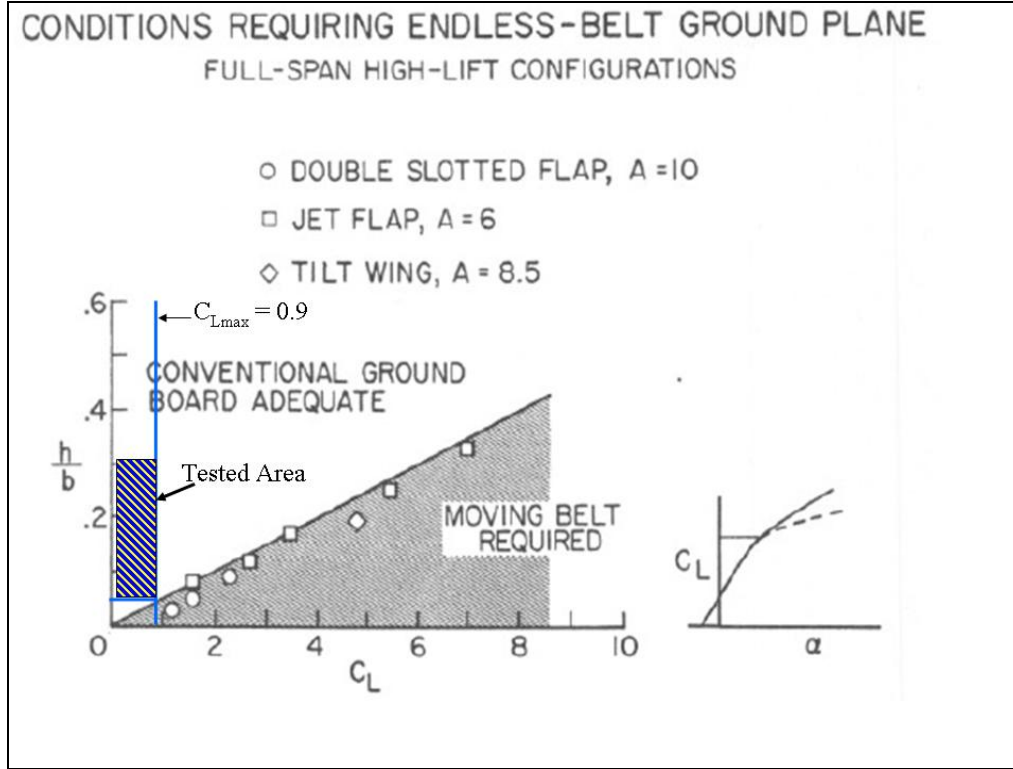
Figure 6: Conditions Requiring an Endless-belt Ground Plane (22)

The shaded box in Figure 6 indicates the region tested in the present study, and the C_L max line indicates the maximum lift coefficient found in Reed's study (8). Thus, according to Turner, a moving-belt ground plane was not required for this experiment.

Kemmerly and Paulson, Jr. did a similar study comparing the use of a conventional ground plane (23). While Turner studied high-lift, high-aspect-ratio models, Kemmerly and Paulson, Jr's study evaluated an F-18 and delta wing models. They concluded that if the condition in Equation [3] was satisfied, then an engineer must use a moving-belt ground plane to study ground effects.

$$\frac{(h/b)}{C_L} < 0.05 \qquad\qquad [3]$$

15

According to the heights used in this study and the maximum lift coefficient according to Reed, a conventional flat-plate ground plane without a moving-belt was adequate to properly measure ground effects, Table 1 shows that Equation [3] was not satisfied.

Table 1: Justification for a Flat-plate Ground Plane

h/b	C_L max *	(h/b) / C_L max	< 0.05 ?
0.3	0.9	0.33	No
0.15	0.9	0.17	No
0.1	0.9	0.11	No
0.05	0.9	0.06	No
* as denoted in Reed's study			

Section 4 – Goals of the Experimental Effort

Reed concluded that the chevron shaped planform performed the best with respect to aerodynamics and longitudinal/lateral stability. A ground effect analysis will further the investigation of the aerodynamics of an advanced aircraft configuration.

The goal of this effort is to:

- identify the ground effect region of the chevron-shaped planform with respect to height above the ground;

- expand the existing aerodynamic database for moderately swept, low aspect ratio, tailless, blended wing body UAVs;

- analyze the test section flow characteristics of the AFIT 3' x 3' wind tunnel with a ground plane;

- verify McCormick's equation for induced drag factor, and

- compare aerodynamic out-of-ground effect data with Reed's study.

The following will include an overview of the research considered, a description

of the equipment and procedures used, results and analysis of the experimental data,

concluding remarks, and recommendations.

III. Experimental Set-up & Procedures

The following chapter will explain the various resources and materials used to test the chevron-shaped UCAV in ground effect. It will also include an outline of the wind tunnel testing procedures.

Section 1 – UCAV Model

As mentioned previously, the wing planform used in this study was originally tested by Capt. Shad Reed of AFRL/VAAA. The original model was built by Dynamic Engineering, Inc. in 1996 and was tested in the Boeing St. Louis Low Speed Wind Tunnel (LSWT) and in the AFRL Subsonic Aerodynamic Research Laboratory (SARL). It was built out of Ren 450, a woodlike epoxy resin board, and 7075-T6 aluminum. Its dimensions can be found in Table 2.

Table 2: Original and Scaled UCAV Model Properties

Chevron UCAV Dimensions		
	Original Model	Scaled Model
Material	Ren 450 & Aluminum	Photopolymer Plastic
Wing Area, in^2	364.87	87.396
Span, in	32	16
Root Chord, in	14.85	7.42
MAC, in	13.35	5.20
Aspect Ratio	2.806	2.929
Leading Edge Sweep, deg	45	45

Figure 7: Original Chevron UCAV

The original chevron UCAV model (shown in Figure 7) has a 32-in wingspan, making it just small enough to fit it the AFIT 3' x 3' wind tunnel. Because its wingtips would extend too close to the test section walls to produce accurate results, so a scaled down version was created. The original electronic drawings could not be found, a 3-D scanner digitized the original model. The engineers and technicians of AFRL/Human Effectiveness Branch (HECV) allowed the author to use a 3-D digitizer and software to digitize the chevron UCAV model.
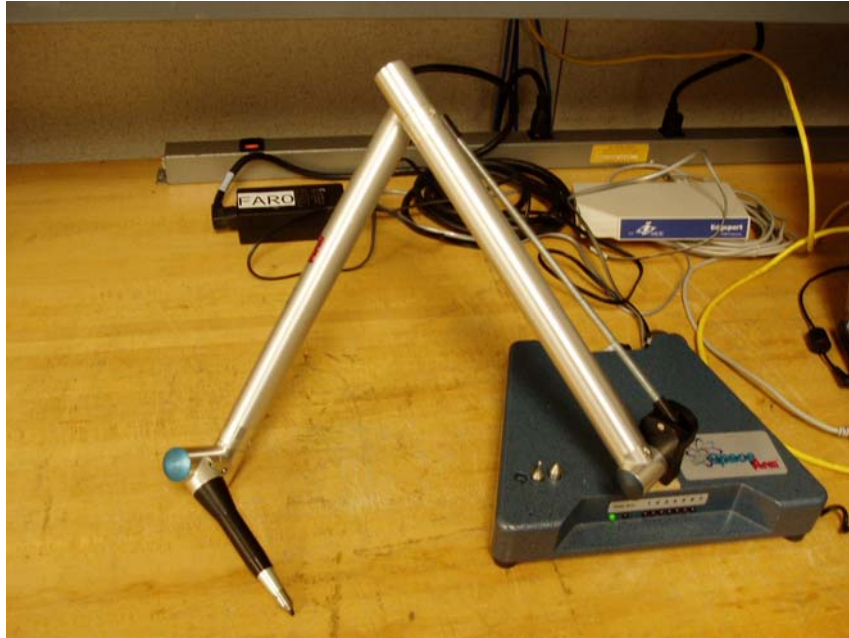
Figure 8: FARO Space Arm™

The digitizer set up included the FARO Space Arm™ (shown in Figure 8) along with Caliper 3D™ Version 2.43. After probe calibration, the pivoting arm was moved so that the probe touched the surface of the model. The points collected were transposed into an IGES file, which was then read into the drawing program Solid Works$^{©}$. Only points along the top surface of the right wing were collected. Since the chevron UCAV is perfectly symmetrical, the surfaces were mirrored across the centerline, and then again to form the bottom surface. Once the model was in Solid Works$^{©}$, the hole for the balance was added so that the model center of gravity (CG) was precisely located 2.5 inches from the back edge of the hole. A scaling factor of $\frac{1}{2}$ was selected, allowing the model to be small enough to fit into the wind tunnel, but large enough to compare and gather aerodynamic data.
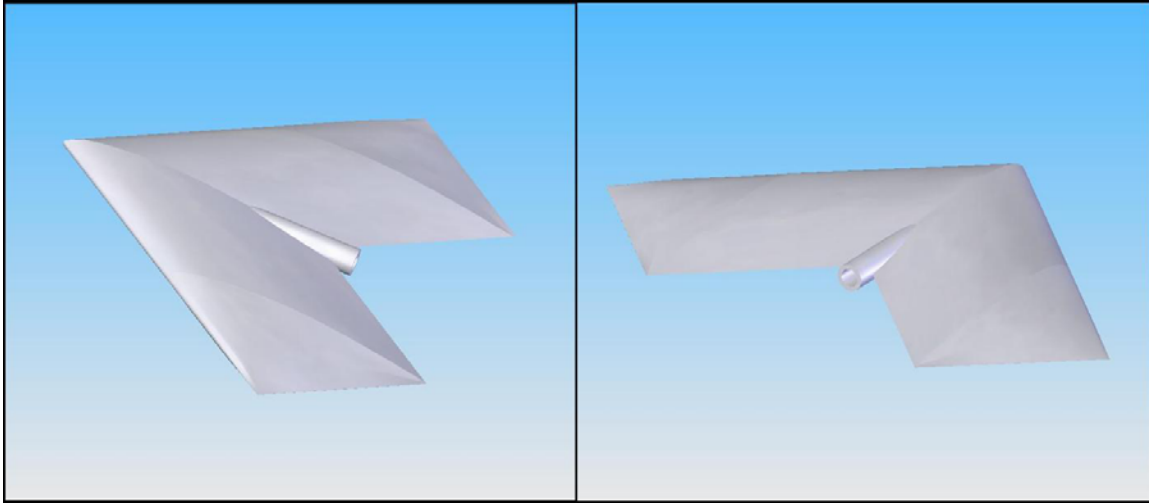
Figure 9: Solid Works Drawings of the $\frac{1}{2}$-scaled Chevron UCAV

The final step in producing the scaled-down version was converting the file

into *.stl* format and then printing it with the AFIT/ENY 3-D rapid prototyping machine.

The Stratasys Objet EDEN 333 rapid prototyping machine uses eight small jets that lay

down UV plastic (also known as photopolyer plastic) material and a gel-like UV plastic

for support material in 0.0006-in layers. The eight jets transverse across the printed

region in 2-in strips followed by a UV light which cures the plastic simultaneously (24).

The Full Cure 700 series photopolymer plastic model material can be machined, drilled,

and chrome-plated; used as a mold; and absorb paint (25). Three images of the scaled

down rapid prototyped model are shown in Figure 10 and Figure 11 . Refer to Appendix

A for more pictures.

Figure 10: $\frac{1}{2}$-Scaled Chevron UCAV Model
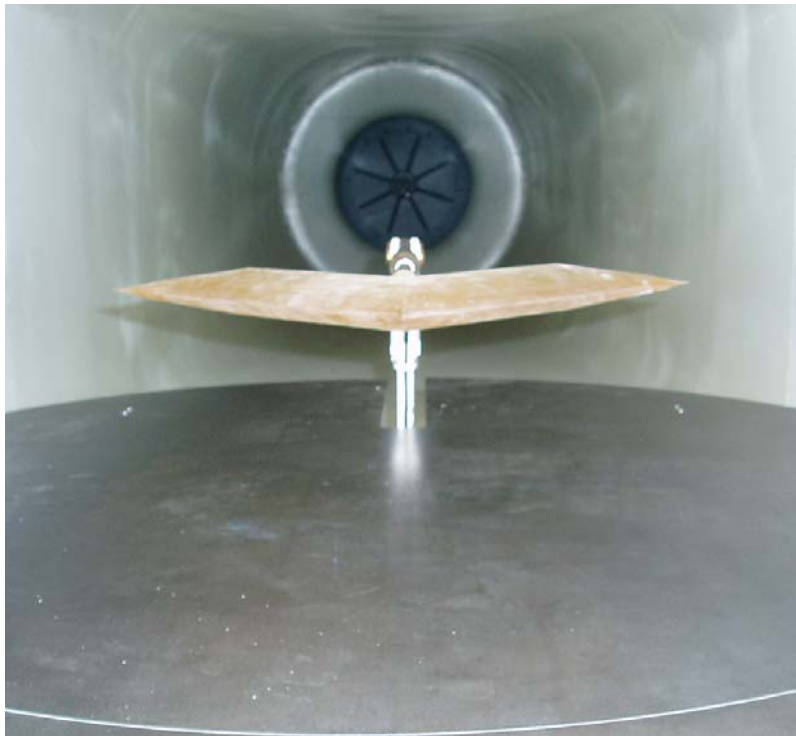
Figure 11: $\frac{1}{2}$-Scaled Chevron UCAV in Test Section

Section 2 – Wind Tunnel

Section 2.1 – Equipment

The AFIT 3' x 3' wind tunnel was fabricated by the New York Blower Company. It includes an ACF/PLF Class IV fan with a Toshiba Premium Efficiency (EQP III) fan motor, all controlled by the Siemens (13710) Adjustable Frequency Tunnel Controller. The fan motor and controller specifications can be found in Table 3.

Table 3: Fan and Controller Specifications

Specifications	
Fan Motor	**Controller**
3 phase induction	
4 Poles	
60 Hz	
230/460 Volts	460 Volts
444/222 Amps	315 Amps
200 Brake Horsepower	250 max HP
1785 RPM Operating Speed	
150 mph - Theoretical Max	
148 mph - Tested Max	

The tunnel is an Eiffel-type, open circuit configuration with a closed test section. The tunnel fan draws ambient air through the 122-in wide by 111-in tall by 70-in deep intake plenum, which internally has a quarter-inch aluminum honeycomb flow-straightener and steel mesh anti-turbulence screens. After the flow passes the last anti-turbulence screen it passes through the convergent portion of the tunnel, which is 95.5-in long and has a contraction ratio of 9.5:1.
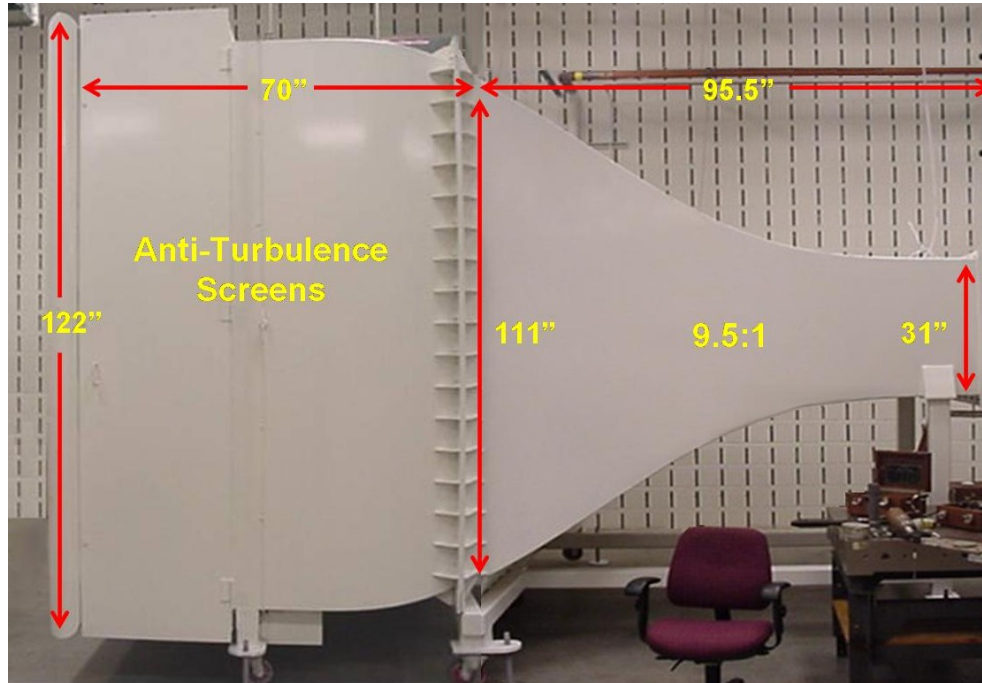
Figure 12: Wind Tunnel Intake and Convergent Sections with Dimensions (26)

After the convergent section, the flow passes through the test section. The test
section is octagonal in shape to eliminate the corner interference effects and has
dimensions of 31.5-in tall, 44-in wide, and 72-in long. The chevron UCAV has a span-
to-tunnel width ratio of 0.37, which is well below the recommended value of 0.8 (27). In
addition, the ground plane frontal area is 6.7% of the test-section cross-sectional area,
which is below the recommended value of 7.5% (27).

The model sting support is positioned in the test section through a slot in the
traverse circular plate. This remotely controlled device can vary the angle of attack of the
model from -25° to +25°. For yaw angle, the traverse circular plate rotates and moves the
entire sting mechanism and can be rotated from -20° to +20°.
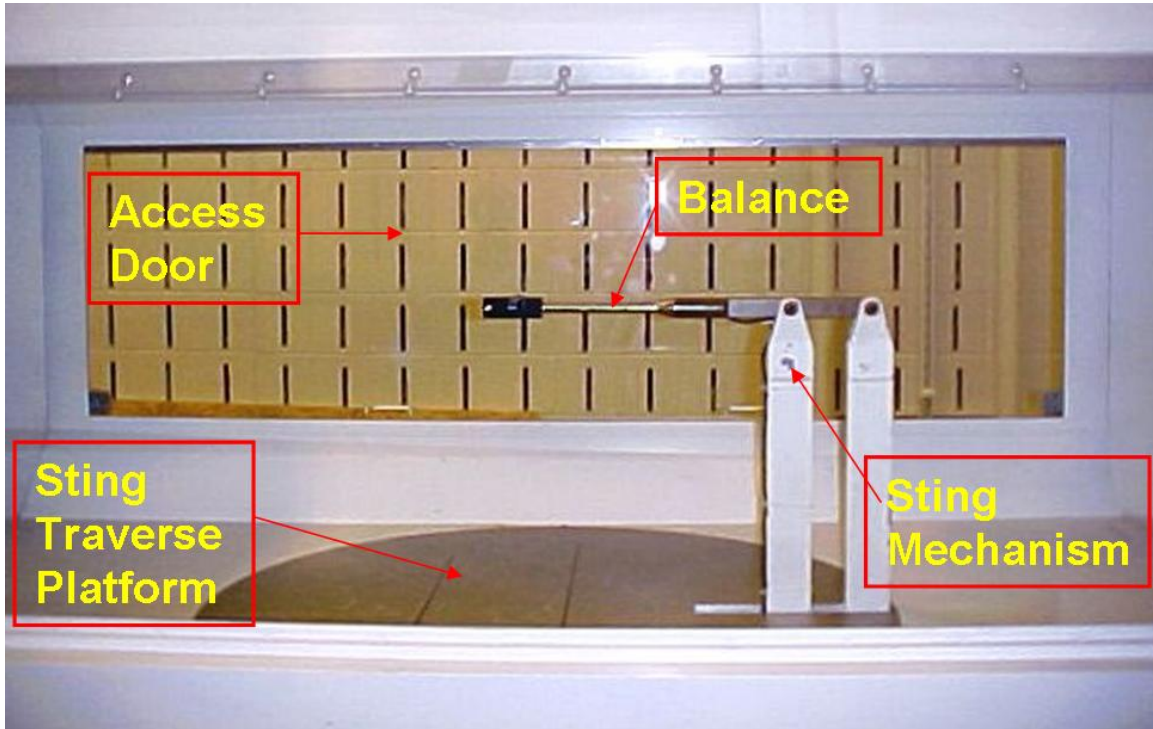
Figure 13: Wind Tunnel Test Section and Components (28)

The balance used for this test was the AFIT-1 Balance, an internal six-component balance manufactured by Modern Machine & Tool Co, Inc. See the complete capacity of strain gage rosettes listed in Table 4. Refer to reference 29 for a more thorough description of the AFIT-1 Balance.

Table 4: AFIT-1 Balance Maximum Loads

Component	Maximum Load
Normal Force (N1)	10 lbs
Pitch Moment (N2)	10 in-lbs
Side Force (S1)	5 lbs
Yaw Moment (S2)	5 in-lbs
Axial Force (A1)	5 lbs
Roll Moment (L1)	4 in-lbs

After the flow travels through the test section, it enters the 26-ft long divergent section, which includes a model catcher in case of any component failure. Once through

the divergent section, the flow goes through the fan and exits vertically up through the

exhaust pipe. See Figure 14 for complete schematic of the wind tunnel.
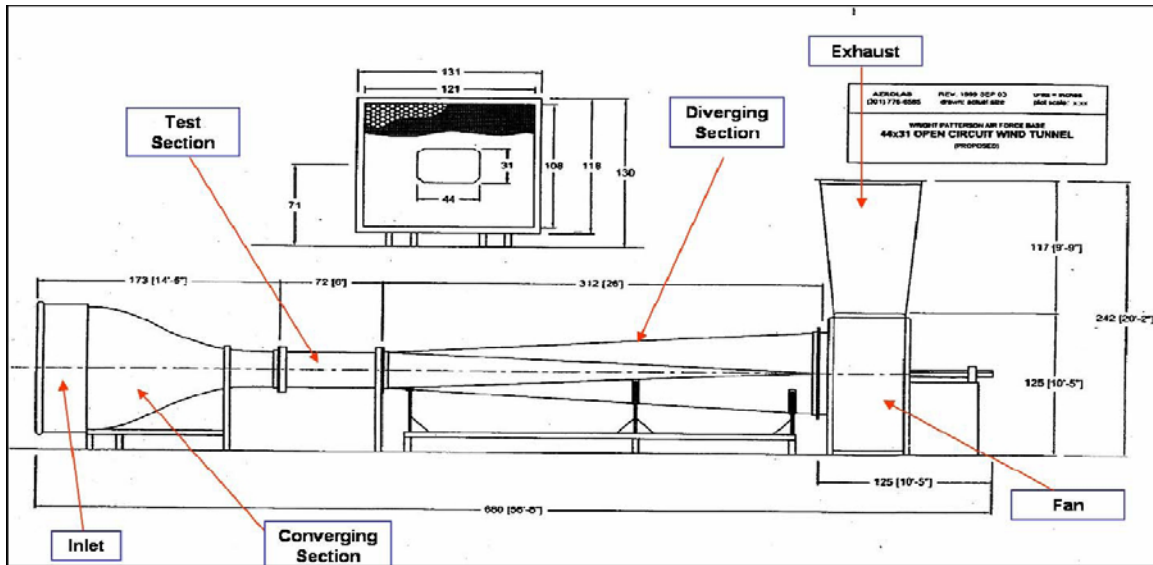
Figure 14: Wind Tunnel Schematic (28)

Section 2.2 – Procedure

A static weight calibration process was carried out first. Known weights were

attached to the balance and the calibration constants were adjusted in the data collection

software by manually matching the loads on the balance to the loads registered in the

software. Linearity was verified by ensuring that the voltages corresponded linearly to

the increases in weights attached. LabView Virtual Instrument$^{©}$ interface was used to

control all tunnel parameters including angle of attack, yaw angle, and tunnel speed.

While this interface controlled these parameters, analog backups of angle of attack and

sideslip angle were also monitored with sting mounted optical encoders. The analog

measurement for velocity was a pressure transducer and pitot-static tube and was the

main guide for tunnel velocity throughout all the test runs.

26

The measured data from the balance was stored in the form of two normal force components (N_1 & N_2), two side force components (S_1 & S_2), an axial force component (A_1), and a roll moment (ℓ_1). Voltage was continuously applied to the strain gage rosette, and resistance was measured across the wire filament. The applied load elongated the wire causing an increase in the resistance. Output voltages from the increased resistance were equated to strain and finally force through a series of calibration equations. A conventional coordinate system was used in the tunnel with +x-direction pointing towards the intake, +y-direction pointing out towards the access door, and +z-direction pointing down towards the tunnel floor. See Figure 15 for a better understanding of the coordinate system.
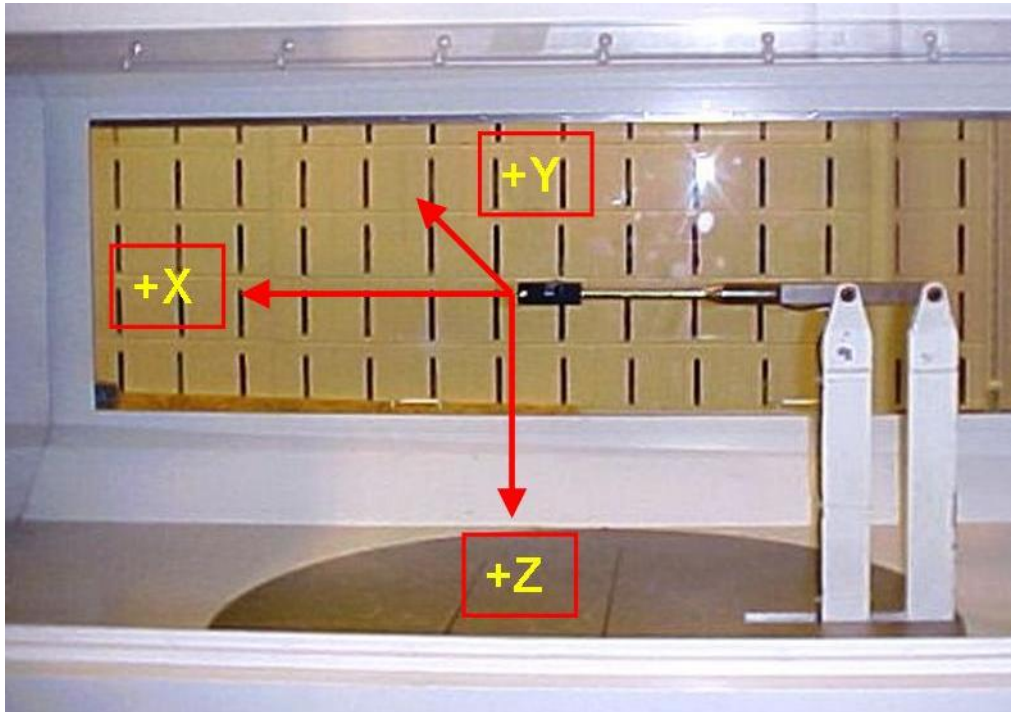
Figure 15: Test Section Coordinates (26)

After the balance was calibrated, the chevron UCAV was mounted to the balance using two 2-56 screws. Because of the symmetrical wing planform of the UCAV model,

the balance was in line with the longitudinal x-axis and at the y- and z-axis centers of gravity.

The chevron UCAV model was tested in two different flight conditions: Out-of-Ground-Effect (OGE) and In-Ground-Effect (IGE). The OGE tests examined the longitudinal forces and moments on the UCAV away from the ground, whereas the IGE tests explored the same criteria except the ground plane was placed at four different heights. The proposed test conditions called for four different wind tunnel speeds each with angle of attack sweeping from -10 deg to +20 deg. However, these conditions were not met for most of the test runs due to balance capacity limitations and potential model or sting mechanism collision with the ground plane. Table 5 shows the actual test matrix for each test run. A tare or wind-off run was completed to calculate the effect of the UCAV's static weight on the balance. This effect was necessary to remove the tare effects on the axial sensor, which affects the drag coefficient calculation.

Table 5: Experimental Test Matrix

Tunnel Speed: (mph)	UCAV only	Plane 1 h/b = 0.3	Plane 2 h/b = 0.15	Plane 3 h/b = 0.10	Plane 4 h/b = 0.05
40	$-10^o < \alpha < +20^o$	$-10^o < \alpha < +17^o$	$-10^o < \alpha < +17^o$	$-10^o < \alpha < +11^o$	$-5^o < \alpha < +6^o$
60	$-10^o < \alpha < +14^o$	$-10^o < \alpha < +14^o$	$-10^o < \alpha < +13^o$	$-8^o < \alpha < +11^o$	$-5^o < \alpha < +6^o$
80	$-8^o < \alpha < +7^o$	$-7^o < \alpha < +7^o$	$-5^o < \alpha < +6^o$	$-4^o < \alpha < +6^o$	$-3^o < \alpha < +5^o$
100	$-5^o < \alpha < +4^o$	$-4^o < \alpha < +4^o$	$-3^o < \alpha < +3^o$	$-3^o < \alpha < +3^o$	$-1^o < \alpha < +3^o$

The test matrix in Table 5 shows that as the height above ground decreased, angle of attack variation declined due to the extra forces and moments on the model as it entered into the ground effect region. To avoid damaging the balance due to these added loads, the alpha sweeps were limited.

Section 2.3 – Data Analysis

A data acquisition program was set up within the control computer to store the data in a tab delimited text file at a rate of two data points per second (2 Hz sampling rate). For the alpha sweeps, the flow velocity was slowly increased until the desired speed was reached. After ensuring that the balance was taking accurate data, the model was dropped to its least negative alpha setting and data were acquired for 30 sec. The angle of attack then increased 2 deg and held for another 30 sec. This was repeated until either the balance reached its capacity or the ground plane interfered with the sting mechanism.

A MATLAB® code, written by Capt. DeLuca (26), Lt. Gebbie (28), and altered for the AFIT-1 balance by Lt. Rivera Parga (29) was used to reduce the acquired force and moment data. The data reduction program received the tare file and one of the experimental test files simultaneously. It then combined the similar measured forces and moments and averaged them to a single test point for each angle of attack. Before this data were exported as aerodynamic coefficients, the physical testing conditions, balance interactions, and blockage correction factors were calculated. For more detail regarding the data reduction program, see references 26, 28, and 29.

After the MATLAB® program reduced the data, an EXCEL® output file was created that consisted of Mach number, Reynolds number, dynamic pressure, velocity, angle of attack, lift, drag, roll moment, pitching moment, yaw moment, and side force coefficients for every angle of attack tested. Standard aerodynamic plots were then created. See Appendix C for a sample calculation of the data reduction.

Section 3 – Ground Plane Design and Construction

In order to properly represent the model flying close to the ground, a ground plane was built and mounted in the wind tunnel. The ground plane was composed of two plates and eight cylindrical legs. The plates were hot-rolled steel and the legs were cold-rolled steel. The dimensions are shown in Table 6 and pictures of the ground plane are shown in Figure 16 andFigure 17. Refer to Appendix A for more pictures and to Appendix B for detailed drawings of the ground plane.

Figure 16: Ground Plane

Figure 17: Ground Plane and Model in Test Section

Ground Plane Dimensions	
Plate	
thickness, in	0.25
diameter/width, in	35.313
max length, in	44.313
Legs	
diameter, in	1.5
length, in	
height 1	9.77
height 2	12.17
height 3	12.97
height 4	13.77

Table 6: Ground Plane Dimensions

The circular plate is identical to the traverse circular plate on the floor of the test section, which rotates to simulate yaw angle. By mounting the circular ground plane piece on top of the circular floor plate, the model being tested with the ground plane can

also experience the same yaw deflection as a model not tested with the ground plane. The circular piece also has a cut 11-in by 1.5-in in the rear to allow the sting mechanism to rotate to alter the angle of attack of the model. Figure 18 shows the two pieces separated.

Figure 18: Top View of Ground Plane with Front and Circular Pieces Separated

The front piece of the ground plane provides a straight leading edge that is rounded and beveled cut as shown in Figure 19.

Figure 19: Leading Edge of Ground Plane

A pair of screws mounted in counter-bored holes was used to attach each cylindrical leg to the flat plate. Sixteen holes were drilled in the test section floor so that the eight legs were mounted securely. A stress analysis was completed to ensure that the maximum dynamic pressure of the wind tunnel's maximum velocity (150 mph) would not sever the screws and overturn the ground plane. Four quarter-inch screws were used to mount each leg, which resulted in a factor of safety of 18.

Section 3.1 – Predicting the Leg Heights

Not having the flexibility of altering the model height with the sting, the ground plane height was changed to vary the height above ground. Various methods were considered including using hollow cylinders with varying rows of holes held together by pins to allow for a changing ground plane height. With the uncertainty of how the

dynamic pressure would affect the ground plane, it was decided to use four different leg heights that were interchanged for each height.

The ground plane heights were selected to ensure the greatest effect from the ground on the model. Based on McCormick's ground effect prediction for induced drag along with the ground effect regions discovered in references 17, 20, and 21, the four heights were chosen and can be seen in Table 7.

Table 7: Ground Plane Heights and Corresponding h/b

GP Designator	height	h / b
Plane 1	10.02	0.3
Plane 2	12.42	0.15
Plane 3	14.22	0.1
Plane 4	14.02	0.05

Model height above ground was referenced from the root quarter-chord.

Section 4 – Boundary Layer Calculations

While time constraints did not allow for boundary layer measurements, conventional flat plate boundary layer equations were used to predict the boundary layer height and displacement thickness at the model location.

Typically, boundary layers are divided into two types: laminar and turbulent. Each type has a no slip and solid surface boundary condition, which means that the fluid particles touching the surface have zero velocity and the flow can not travel through the surface.

The laminar boundary layer calculations utilized the Falkner-Skan method (30). While this method can be used for flows around a wide range of configurations, the simplest form, flow past a flat plate, was used in this study. The laminar boundary layer

thickness was defined as the distance from the flat plate to where the velocity equaled

99% of the free-stream velocity. Assuming an inviscid, incompressible flow, the laminar

calculations used the following equation:

$$\delta_{lam} = \frac{5.0x}{\sqrt{Re_x}}$$ [4]

As the boundary layer builds up in the streamwise direction, a transition process takes

place due to disturbances in the flow. This transition segment can vary widely in length

and strength, but normally depends on pressure gradient, surface roughness,

compressibility effects, surface temperature, suction or blowing on the surface, and free-

stream turbulence (30). For this study, it will be assumed that this process occurs

instantaneously.

For incompressible flow past a flat plate, transition is function of Reynolds

number. It is customary to use a Reynolds number of 500,000 to locate the transition

point (30). For each tunnel velocity used for the experiment, a different transition point

was located. The laminar boundary layer thickness was noted at this location, and the

turbulent boundary layer was set equal to this thickness.

Exact calculations of the turbulent boundary layer normally involve differential

equations of motion for computational fluid dynamic models. For this study, time-

averaged (or mean-flow) properties were assumed and the flow velocity was represented

by the power law approximation, noted in Equation [5].

$$\frac{U}{U_\infty} = \left(\frac{y}{\delta}\right)^{1/7}$$ [5]

From this estimate, the turbulent boundary layer thickness could be derived based on Blasius' skin friction coefficient for a turbulent boundary layer on a flat plate. To see the actual derivation, see reference 31.

$$\delta_{turb} = \frac{0.3747x}{\left(\text{Re}\right)^{0.2}}$$

[6]

As mentioned before, an instantaneous transition was assumed, and so Equation [6] was set equal to Equation [4] at the transition point. Solving this equation for *x* and subtracting the result from the transition point gave the pseudo-starting point for the turbulent boundary layer build-up. Figure 20 illustrates the assumptions.
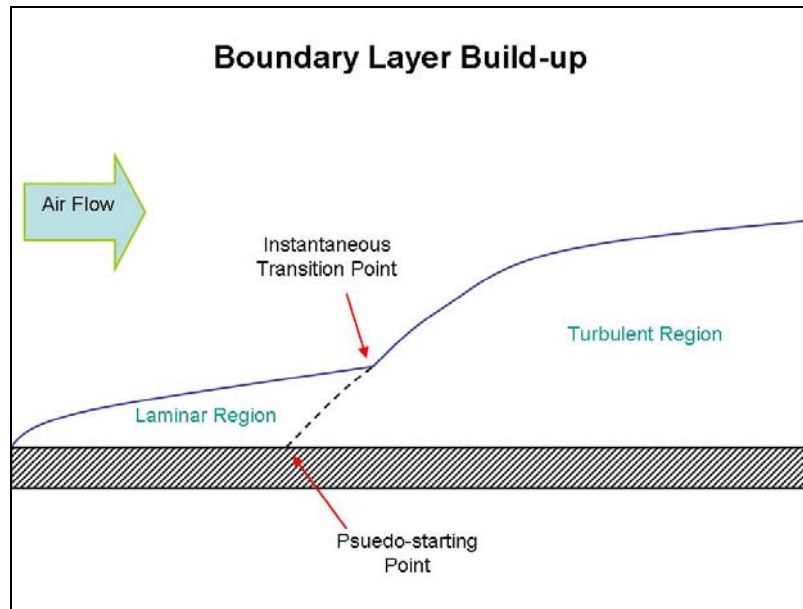
Figure 20: Schematic of Boundary Layer Build-up

The boundary layer thickness results were most relevant for the streamwise *x* locations from the nose of the model to the trailing edge. In order to determine the

distance the external streamlines were shifted due to the presence of the boundary layer, the displacement thickness was calculated using Equation [7].

$$\delta^* = \int_0^{\delta} \left(1 - \frac{U}{U_\infty}\right) dy \qquad\qquad [7]$$

The displacement thickness is largely dependent on the velocity profile. Substituting Equation [5] into Equation [7] with δ equal to the turbulent boundary layer thickness at the trailing edge of the model, the displacement thickness was estimated.

Section 5 – Hot-wire Anemometry

A hot-wire anemometry experiment was used to determine the difference between the indicated transducer velocity and the actual velocity at the model. Also, it was used to examine the blockage effects due to the ground plane. The following describes the equipment, procedure, and data analysis.

Section 5.1 – Equipment

The AFIT low-speed 3' x 3' wind tunnel is equipped with a Dantec-Dynamics Streamline 90N10 Constant Temperature Anemometer (CTA). It is fully motorized and programmable with a 3-axis traversing system. The probe type used was a single wire 55 P11 and was used with the vertical attachment. Figure 21 is a drawing of the probe with the single wire parallel to the y-axis.
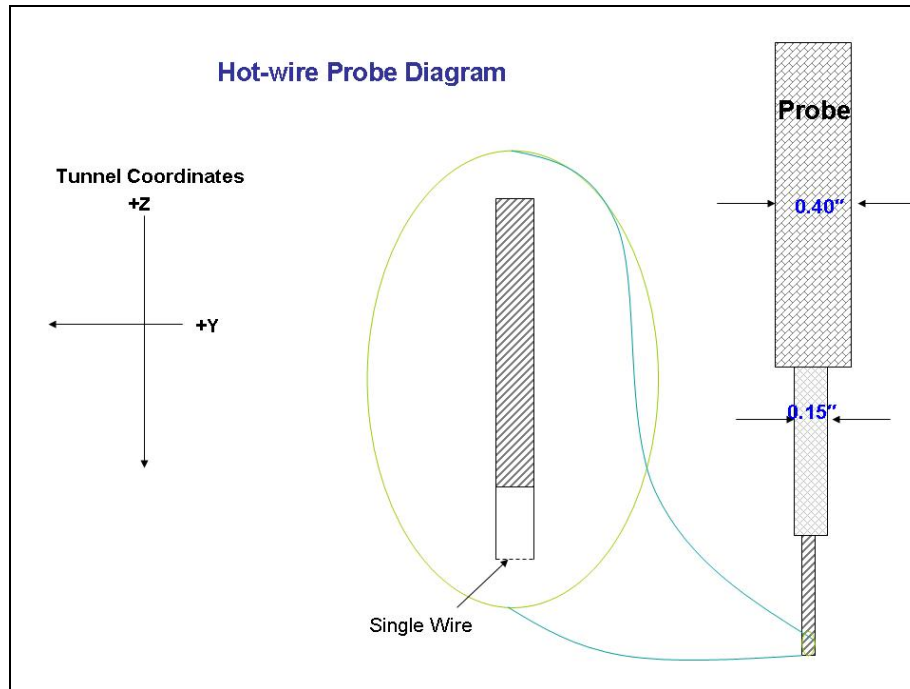
Figure 21: Schematic of Hot-wire Probe Configuration

The maximum range of the probe is 19.7 inches in the horizontal (y-direction) and vertical (z-direction) direction. It also has the capability to traverse longitudinally in the x-direction approximately 3 ft. The Dantec hot-wire anemometer came with a data acquisition program called Streamware® which was used to collect, process, and format data.

Section 5.2 – Procedure

The hot-wire anemometer was calibrated using the Dantec automatic calibrator system. While the hot-wire is outside the tunnel, the automatic calibrator with attaching nozzle blew air across the single wire probe. The velocity was controlled by the Streamware® software in the control room and was increased from 4.5 mph to 161 mph. As the known velocity increased, the anemometer measured the voltage across the single wire. The calibration program within the Streamware® software automatically created

the conversion factor between volts and metric-based velocity, which was manually converted to mph for consistency.

For the hot-wire anemometry experiment, the top Plexiglas window was removed and replaced by one with slotted groves specifically designed for the hot-wire. The slots were plugged according to the longitudinal station of interest. Figure 22 illustrates slot number 1 open for hot-wire velocity measurements.
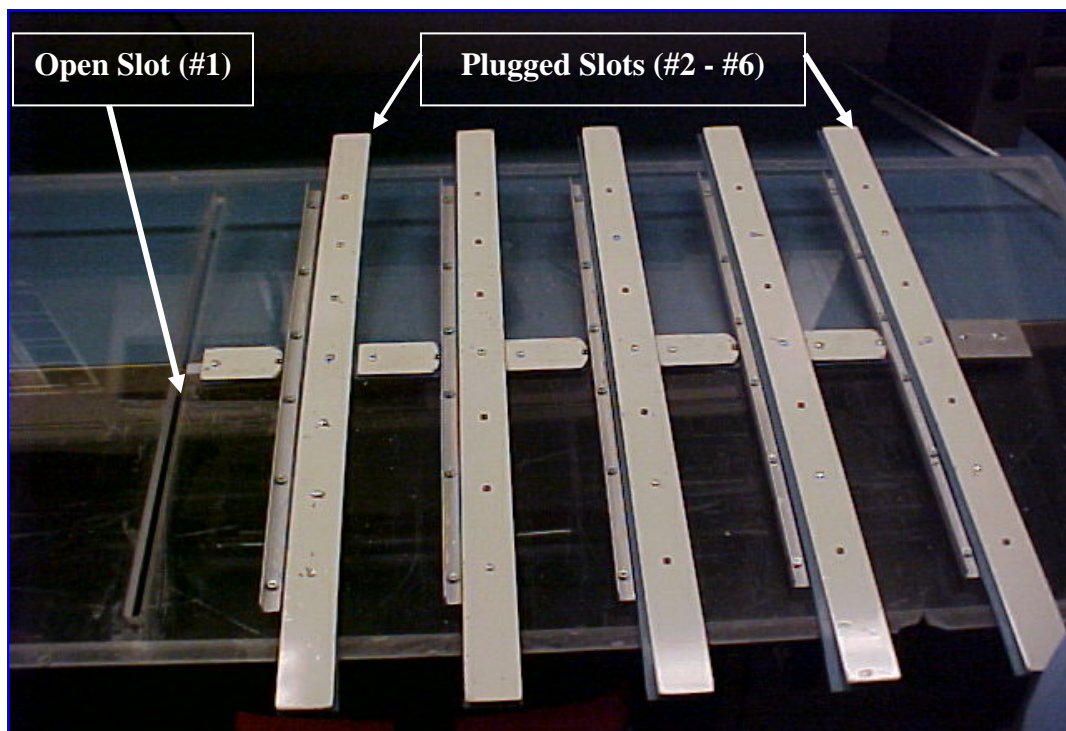
Figure 22: Removable Plexiglas Top for Hot-wire Anemometry (26)

Slot number 2 was used for this experiment because it was the closest station to the model CG. Its exact location was 2 inches in front of the model CG. Velocity was measured without the ground plane, at the lowest ground plane height, and the highest ground plane height at speeds of 40, 60, 80, and 100 mph.

The probe started at a position 1-in outside the left wing and 1-in above the top

surface. It first descended 2.36-in collecting velocity data every 0.40-in to a location

0.36-in below the bottom surface of the model. It then translated 1.89-in in the positive

y-direction, collected data, and then ascended 2.36-in again collecting data every 0.40-in.

It continued on this pattern across the entire span of the model stopping at 1-in outside

the right wingtip. See Figure 23 for the nominal probe grid test pattern.
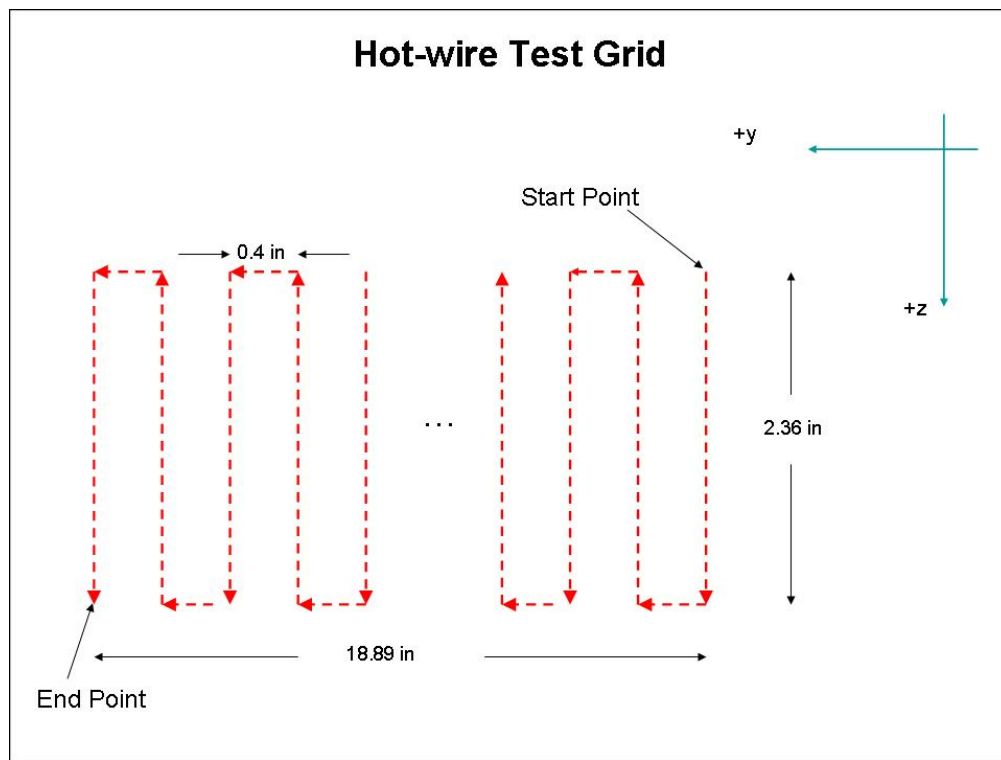
Figure 23: Hot-wire Test Grid

Section 5.3 – Data Analysis

The Dantec Streamware® software stored the data files from each test run as a

Comma Separated File (.csv). The software converted the raw test data, as voltages into

40

mean velocities at each test point. The mean velocities were compared to the transducer indicated velocities to illustrate the differences.

Section 6 – Vortex Panel Code

A theoretical 2-D vortex panel code from Kuethe, et al. (32) was used to analyze the data from the wind tunnel invesitgatoin. A vortex panel method is one in which the flow around a body is represented by replacing the surface of that body by a "source sheet" (32). The strength of each sheet or panel linearly varies over the surface so that every point on the sheet has a normal velocity equal to the normal component of the free stream velocity. For airfoils, or lifting bodies, the Kutta condition fixes the circulation strength.

Accuracy of the vortex panel method depends on how viscosity, compressibility, and high flow speeds can be incorporated into the computation. The code for this study was strictly inviscid and because of the low speeds tested, compressibility was not a factor. Additionally, the accuracy of the vortex panel method depends on the number of panels used to represent the surface. The more panels used, the more accurate the code. The location of the panel boundaries was based on a circle drawn around the airfoil intersecting through the leading and trailing edges centered at the midchord. Diameter lines were drawn through the midchord point. Another line was drawn from the intersection of the diameter lines with the circle to the airfoil inside, identifying the boundary points for each panel.

Control points were established at the center of each panel. The normal velocity at these points was set to zero to ensure the vortex panel code met the condition of the

airfoil being a streamline. Figure 24 is a picture of the method by which the panel

boundaries were determined along with the location of the control points.
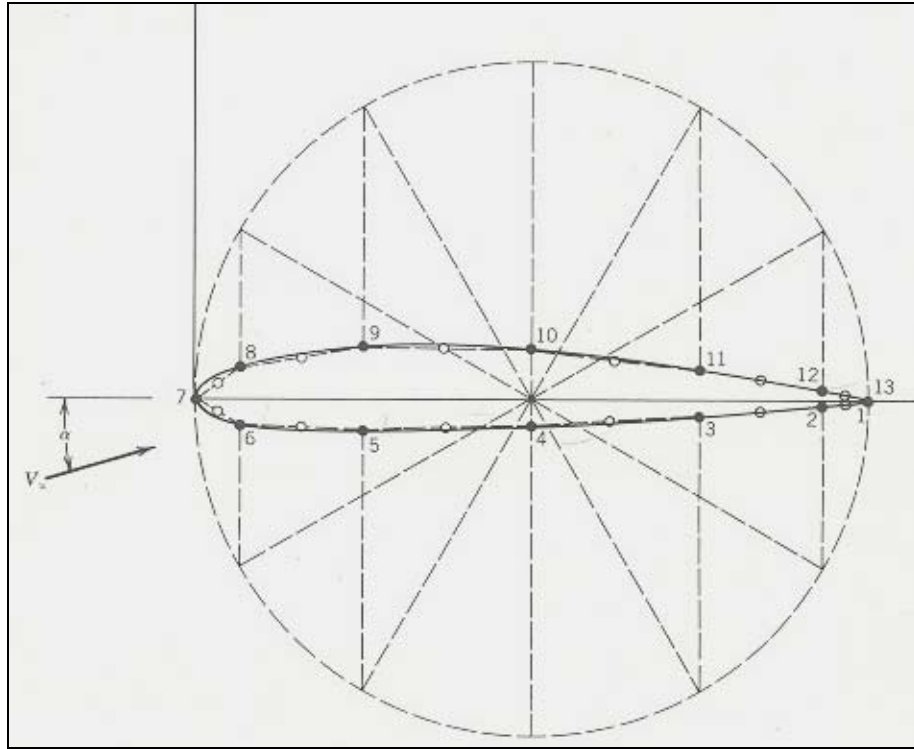
Figure 24: Method for Determining Panel Boundaries (32)

Figure 24 shows how 12 souce panels represent an airfoil. The vortex panel code used in

this experiment utilized 100 panels and control points.

The vortex panel method used reflection to analyze ground effect. Two airfoils

were placed a certain distance from each other, and a region of zero vertical velocity

forms half way between each airfoil, which simulates the ground. The code inputs airfoil

chord length, thickness, camber, max camber location, and angle of attack. Also,

airspeed, density, and distance from the ground (measured from the quarter-chord) were

inputted. The four plots outputted were surface pressure coefficient distribution, pressure

field, streamlines representing the flow field, and velocity field. Additionally, the code

calculated lift coefficient, circulation, lift force, pitching moment.

VI. Results & Analysis

This chapter presents the data gathered from the wind tunnel experiments for the chevron UCAV. The hot-wire anemometry data will be presented first followed by the flow visualization and ground effect results.

Section 1 – Hot-wire Anemometry

The results from the hot-wire anemometry experiment exposed a significant difference in the velocity measured by the pressure transducer and the hot-wire anemometer. Figure 25 shows the transducer measured velocity compared to the hot-wire measured velocity for the open tunnel or OGE test condition.
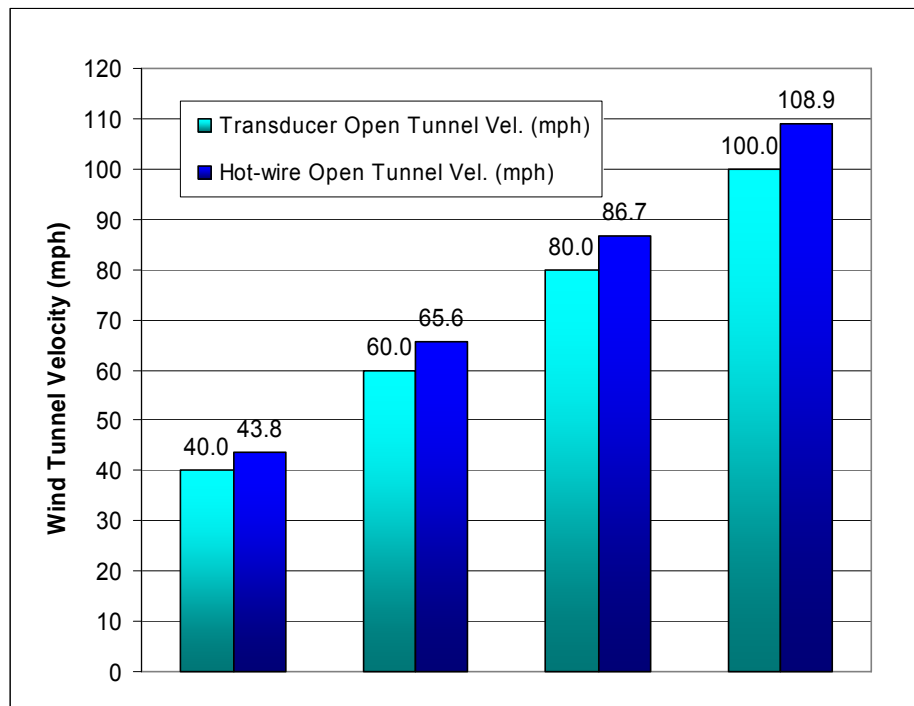
Figure 25: Open Tunnel Hot-wire and Transducer Velocity Comparison

The first observation from the data in Figure 25 is the averaged 9% difference in the open tunnel hot-wire velocities compared to the transducer velocities at each test condition. Although, there was no blockage in the test section during the open tunnel hot-wire runs, this difference was accounted for in the MATLAB$^{©}$ data reduction code in the form of a blockage correction. It was later discovered that the pressure transducer tube had a leak, which perhaps attributed to this error. The leak was patched, but due to time constraints, re-testing was not done, so the hot-wire measured velocities were considered the reference wind tunnel speeds.

To measure the blockage effect due to the ground plane, the wind tunnel velocity, as indicated by the pressure transducer, was held constant while the hot-wire measured the tunnel velocity with the ground plane in the test section. The ground plane was set at its lowest height (h/b = 0.3) and its highest height (h/b = 0.05) for the blockage measurements. Figure 26 are the results of the ground plane hot-wire measuments compared to the open tunnel hot-wire measurements.
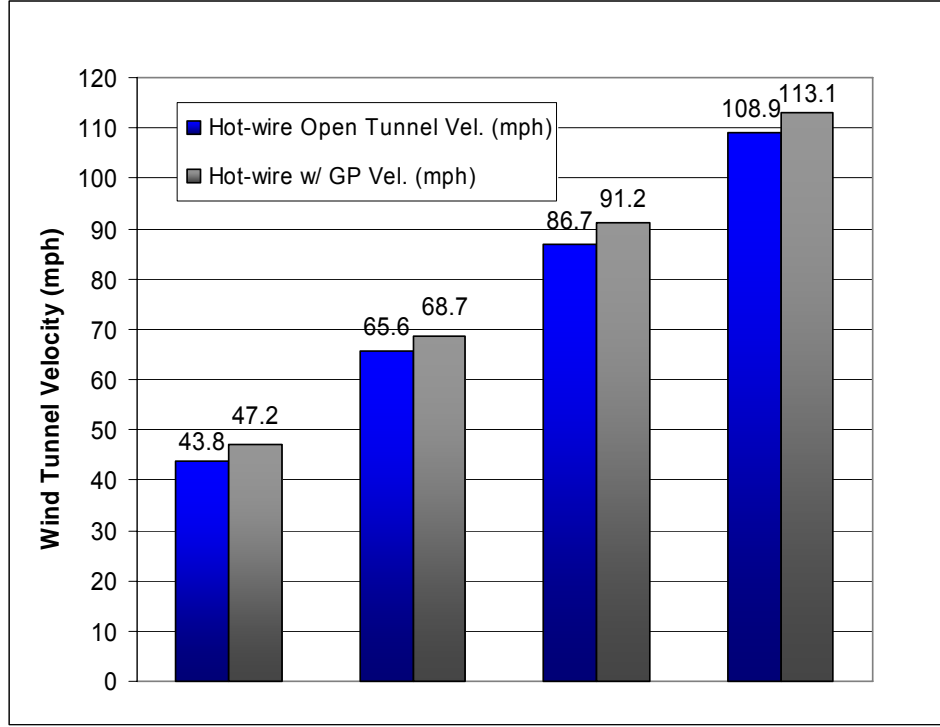
Figure 26: Hot-wire Velocity Comparison

The percent difference between the average velocities measured at the two ground plane heights was less than 1%, so the ground plane hot-wire velocities in Figure 26 were averaged.

With the ground plane in the test section, the airflow was forced to speed up to satisfy the conservation of mass. Blockage correction factors consisted of ratios between the open tunnel and ground plane velocities.

The total blockage correction facors between the tunnel velocity with the ground plane and the transducer velocity were computed as follows:

$$\frac{GP}{Tr} = \frac{OT}{Tr} * \frac{GP}{OT}$$

[8]

where

GP = hot-wire measured velocity with ground plane

Tr = pressure transducer measured velocity

OT = open tunnel hot-wire measured velocity

Table 8 summarizes the correction factors.

Table 8: Velocity Correction Factors Used for Blockage

Correction Factors	40 mph	60 mph	80 mph	100 mph
OT-to-Tr	1.094	1.093	1.084	1.089
Plane 1-to-OT	1.075	1.052	1.055	1.042
Plane 2-to-OT	1.077	1.049	1.052	1.040
Plane 3-to-OT	1.078	1.046	1.050	1.038
Plane 4-to-OT	1.080	1.043	1.047	1.036

Section 2 – Wind Tunnel Ground Effect Tests

The following is the wind tunnel data collected during this test on the chevron UCAV. The ground effect region was examined and identified from the lift and drag coefficient with respect to the longitudinal axis. Table 9 presents the flight parameters at the various test speeds. It should be noted that the wind tunnel velocities labeled on figures in this section and in the Appendix E are 40, 60, 80, and 100 mph, but the corrected velocities accounting for the blockage and measurement error are in Table 8.

Table 9: Summary of Flight Conditions

U_∞* (mph)		Mach No.		q_c (lb$_f$ / ft^2)		Re$_c$	
OGE	IGE	OGE	IGE	OGE	IGE	OGE	IGE
43.65	46.20	0.056	0.060	4.57	5.09	2.37×10^5	2.50×10^5
66.00	68.05	0.085	0.088	10.44	11.04	3.59×10^5	3.68×10^5
87.88	91.60	0.114	0.119	18.51	20.01	4.77×10^5	4.95×10^5
109.30	113.29	0.141	0.147	28.63	30.60	5.94×10^5	6.12×10^5
* = corrected velocity							

Section 2.1 – Model Only Runs

The purpose of the tunnel tests without the ground plane was to establish OGE data and also to verify the results with the longitudinal characteristics Reed (8) identified. Figure 27 shows similarities between the lift coefficients measured with the original chevron UCAV and the scaled down version.
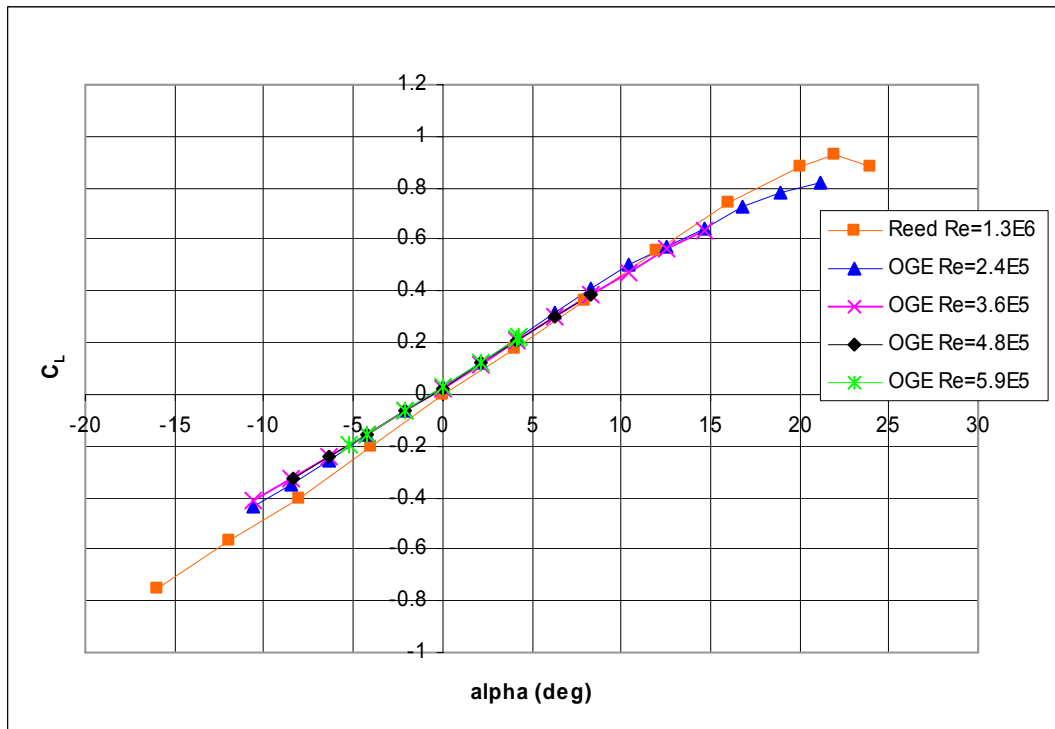
Figure 27: Aerodynamic Comparison - C_L vs. alpha

The lift curve slope, $C_{L\alpha}$, as approximated from Figure 27, is 0.044 per deg, and is relatively the same for both tests. Another comparison from Figure 27 is the lower C_L max for the scaled chevron UCAV. Reed's data indicates a C_L max of 0.917 which is 0.1 higher than the inferred C_L max of the scaled model at 40 mph (8). This difference agrees with the convention that higher Re, the higher C_L max for similar planform shapes (27). Reed conducted his experiments at a Reynolds number based on the root chord of

1.30×10^6 which makes it reasonable to suggest that the C_L max values for the chevron

UCAV of this study would be less than 0.917.

   In the same fashion, the drag coefficient of Reed's study (8) and the one measured

on the scaled UCAV differ, but again it is most likely because the models were tested at

different Reynolds numbers. Figure 28 and Figure 29 are the drag polars of the original

chevron UCAV and the scaled version at each test speed.
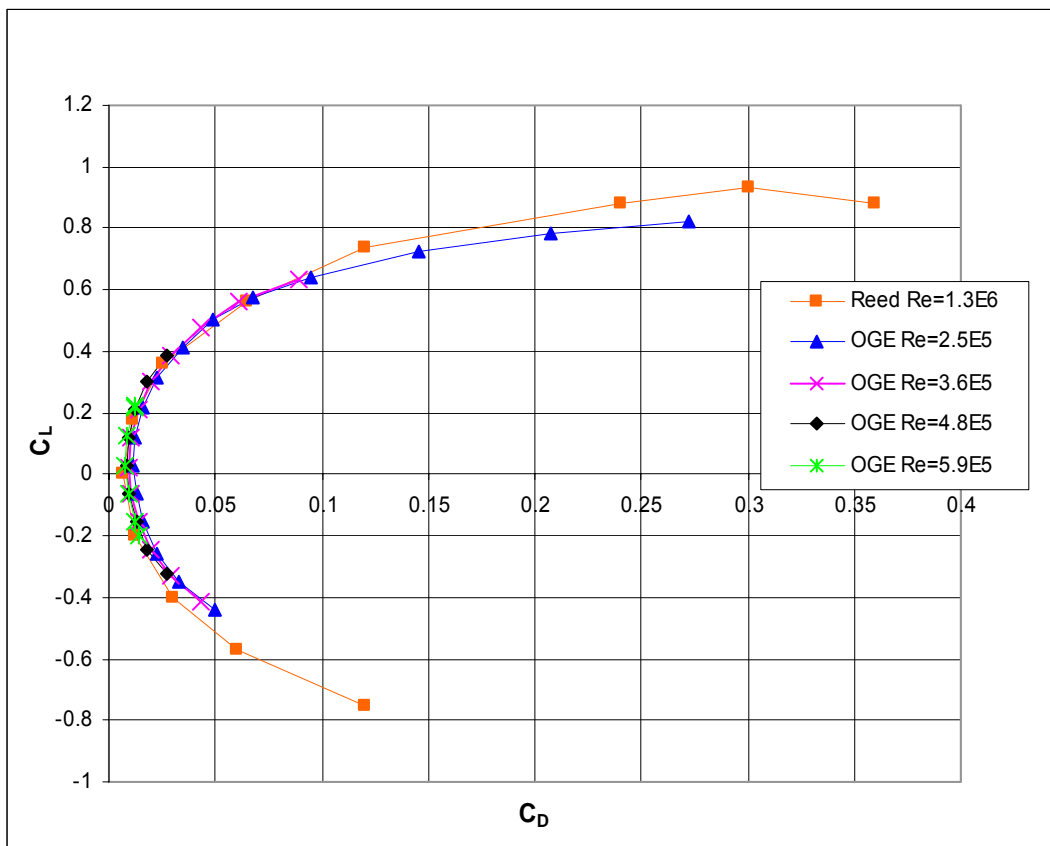
Figure 28: Aerodynamic Comparison - C_L vs. C_D
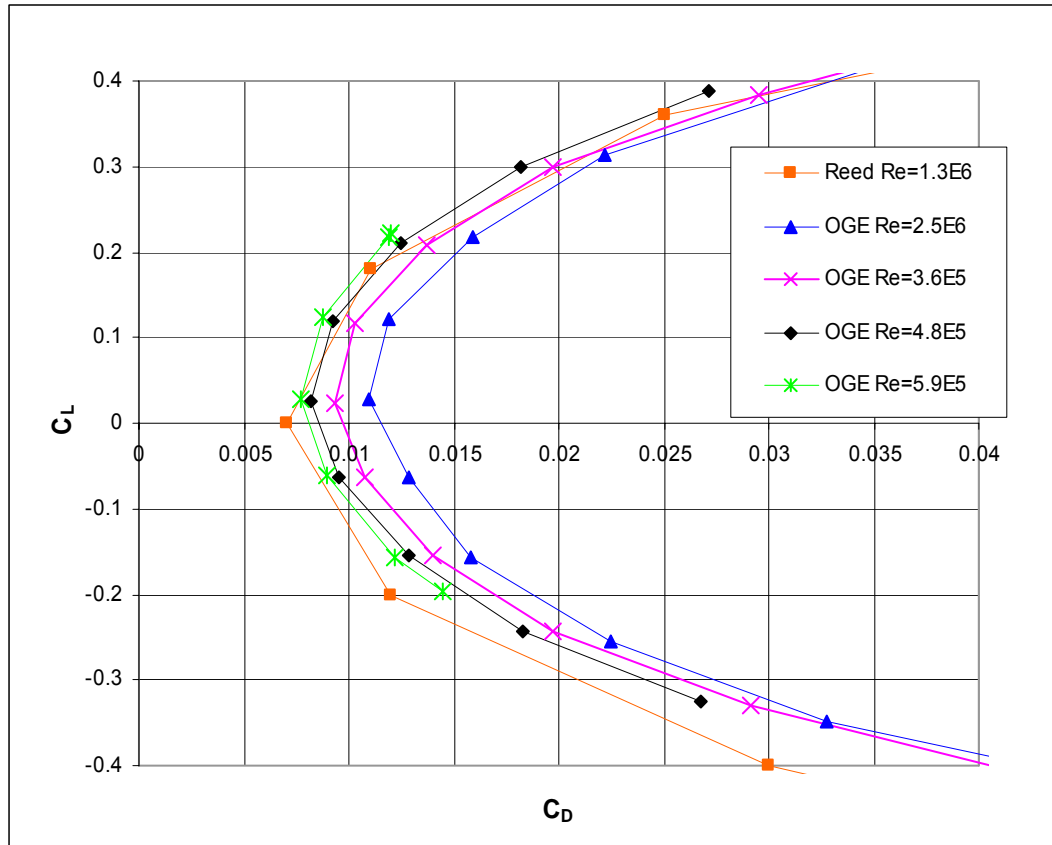
Figure 29: Aerodynamic Comparison - C_L vs. C_D Zoomed In

As can better be seen from the reduced range plot of Figure 29, as Re decreases, C_D increases. This is consistent with convention that at lower Re, more flow separation occurs causing more drag (27).

On another note, the balances used for each respective test were stressed close to their full capacity. The previous study used a 200-lb balance whereas the AFIT-1 balance had a capacity of 10-lbs, but due to the significant weight difference between the two models, each balance was stretched to its full capacity, which decreases the uncertainties of the data (8).

Section 2.2 – Varying Ground Plane Heights

The following plots illustrate the effects of the decreasing height above ground with respect to lift and drag. The height above ground was measured from the root quarter-chord. The data presented is only for the two lowest speeds, 40 and 60 mph, because the balance limitations were exceeded at the two faster speeds. Refer to Appendix E for plots of the data collected at the two faster speeds.

Section 2.2.1 – Lift Coefficient Variation

The OGE data is shown in the following plots as the far right point or the point where h/b = 0.93. Figure 30 Figure 31 show the variation in lift at four different angles of attack as a function of height above ground at 40 and 60 mph, respectfully.
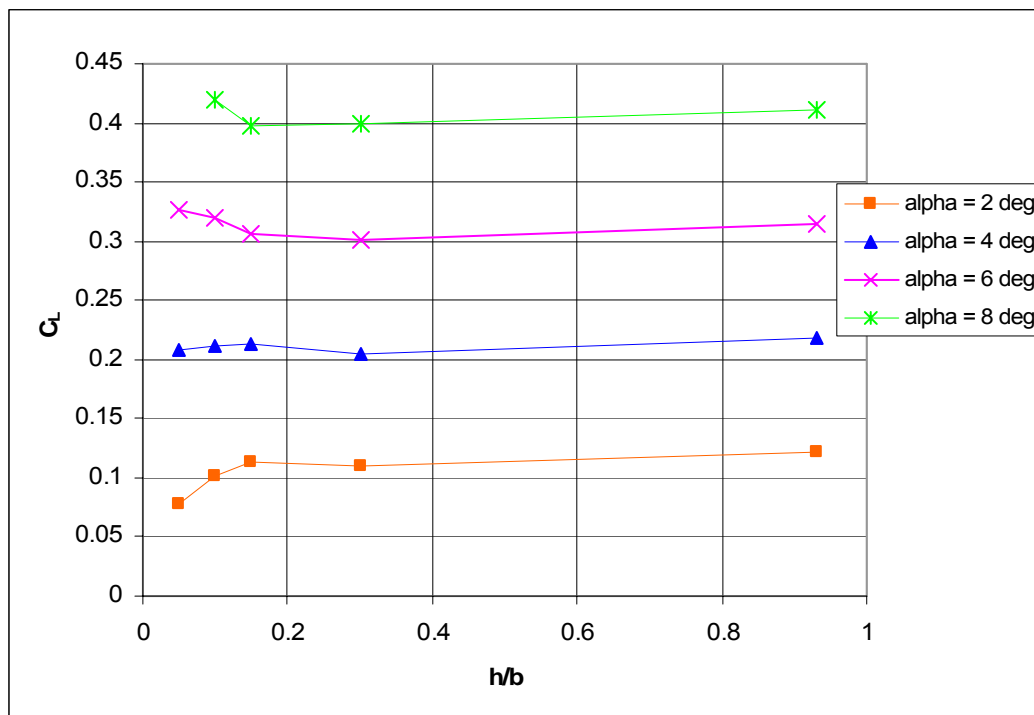
Figure 30: Ground Effect - C_L vs. (h/b) 40 mph
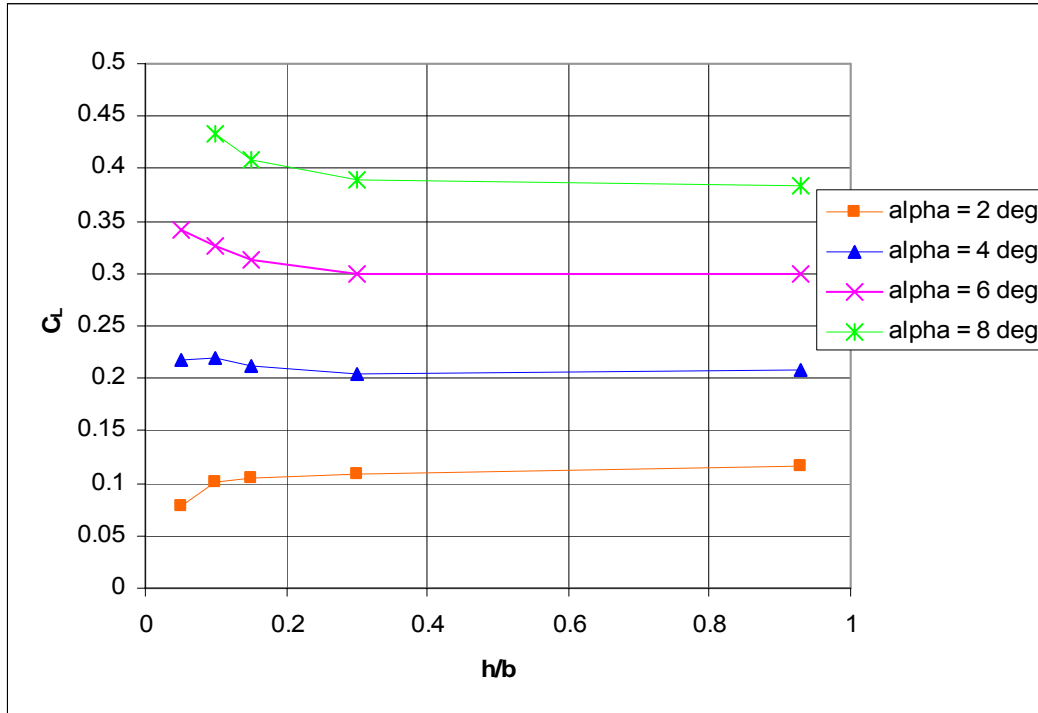
Figure 31: Ground Effect - C_L vs. (h/b) 60 mph

Since the OGE or model-only test runs were at a slightly slower velocity than the runs with the ground plane, as shown in Figure 25, the points corresponding to OGE were omitted from the analysis of the ground effect region.

The overall trend in C_L as height above ground decreases is consistent in Figure 30 and Figure 31. At 6 and 8 deg angle of attack (AOA) C_L increases steadily below h/b of 0.3. This increase is typical and expected for most aircraft flying in ground effect. Also, rate of change in C_L increases from 0.095 to 0.11 per h/b at 40 mph and from 0.13 per to 0.22 per h/b at 60 mph. At an AOA of 4 deg the lift coefficient does not change much as the height above ground is decreased, but at 2 deg AOA C_L clearly drops.

The behavior of the lift coefficient as height above ground decreases suggests that the influence of the ground on the chevron UCAV wing planform can be explained using

a 2-D theoretical prediction. The model's airfoil, the NACA 0015, was inserted into the vortex panal code described in Chapter III. Figure 32 shows the section lift coefficient as a function of height above ground for 40 mph.
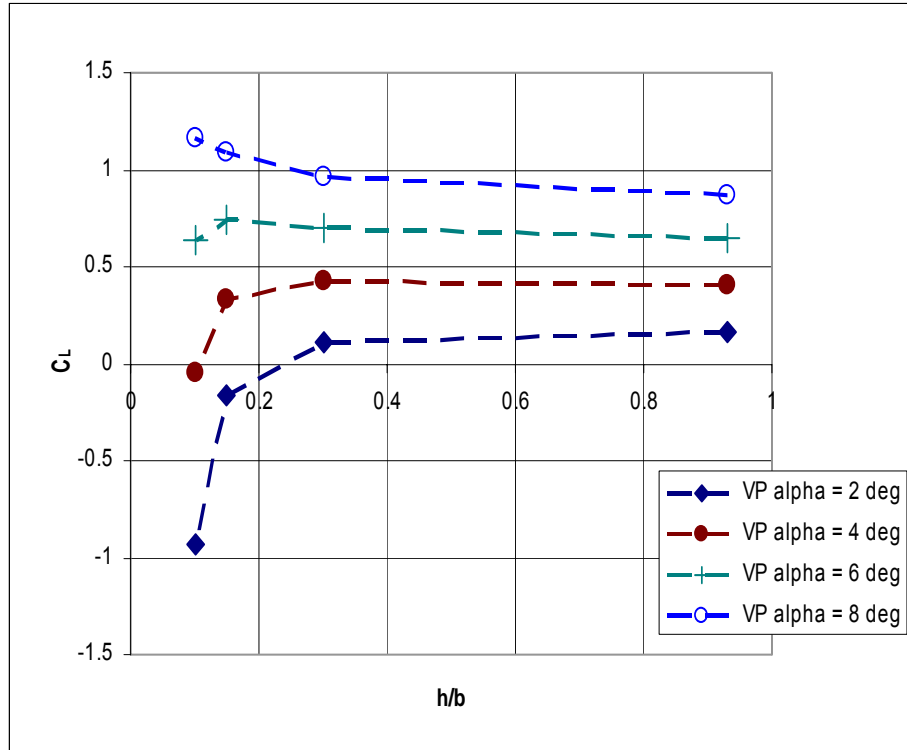
Figure 32: Ground Effect - 2-D Vortex Panel Prediction - C_L vs. (h/b) 40 mph

The values of lift coefficient in Figure 32 do not match up to those in Figure 30 and Figure 31 because section lift coefficient is generally higher compared to a wing of finite span with the same airfoil (27). Nevertheless, the trends of the curves are similar. The increase in lift at AOA of 8 deg suggests that the airfoil is behaving like a standard airfoil with flow traveling faster across the top surface compared to the lower surface producing a positive pressure differential. A pressure coefficient, C_P, contour plot is shown in Figure 33, which was calculated with the vortex panel code.
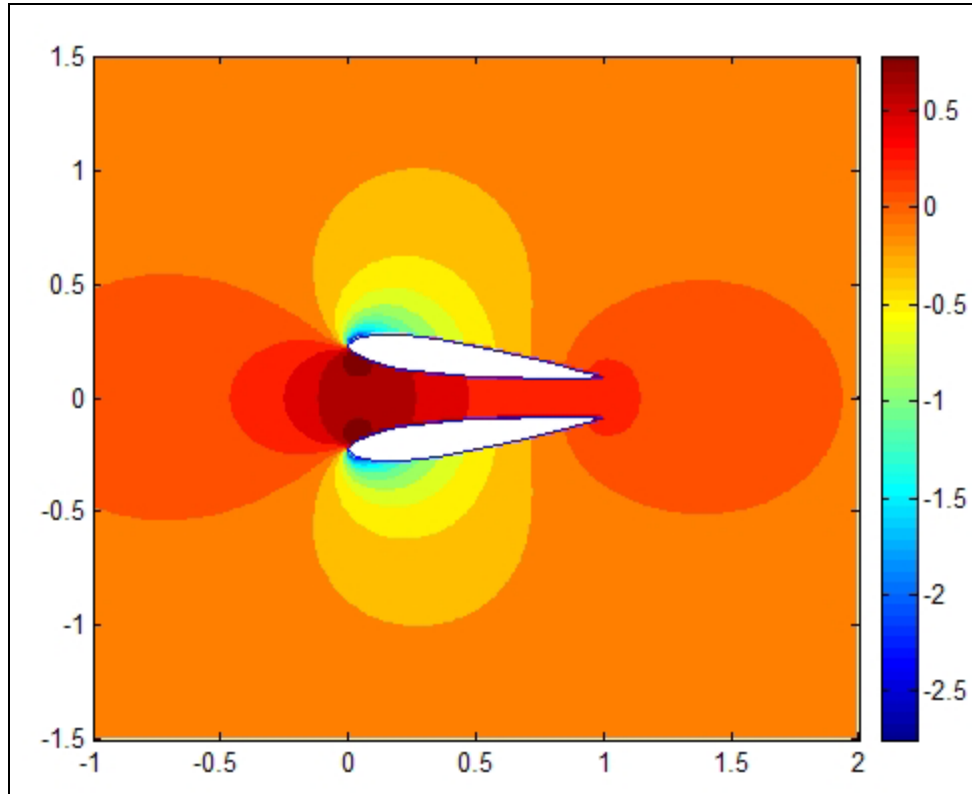
Figure 33: Contour Plot of C$_P$ Around an Airfoil in Reflection AOA=8 deg, h/b=0.15

Figure 33 shows that the 2-D vortex panel code predicts the C$_P$ distribution similar to that using thin-airfoil theory, which for a symmetric airfoil states that section lift coefficient is directly proportional to circulation and AOA. However, at lower angles of attack, the vortex panel predicted the opposite distribution as shown in Figure 34.
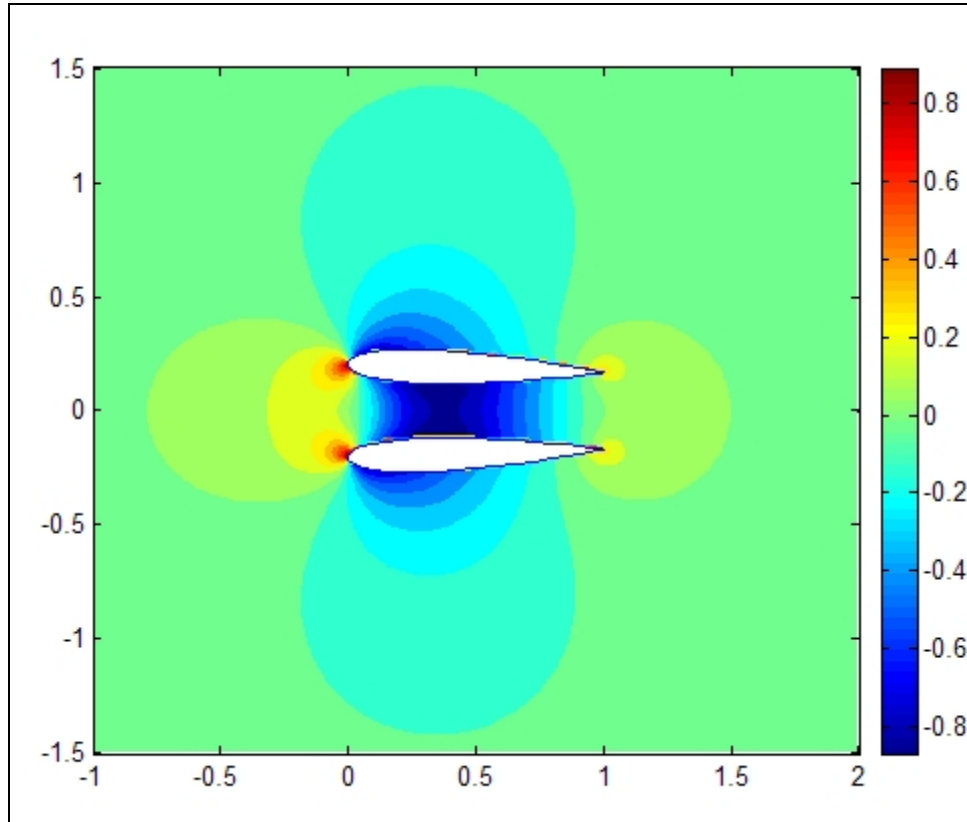
Figure 34: Contour Plot of CP Around an Airfoil in Reflection AOA=2 deg, h/b=0.15

At the same height above ground as in Figure 33, Figure 34 shows a negative pressure coefficient beneath the airfoil. This C_P distribution suggests that airflow was traveling faster across the lower surface of the airfoil compared to the upper surface, which produces negative circulation and negative lift. Whereas the 8 deg AOA C_P distribution was due to the airfoil producing lift agreeing with thin airfoil theory, the C_P distribution in Figure 31 suggests that the thickness of the airfoil was the reason for the negative lift.

As the air attempted to travel between the airfoil and the ground, or streamline of zero vertical velocity, the air speed increased. This is called the Venturi effect, which

states that as a fluid travels through a decreasing cross-sectional area, conservation of mass forces the fluid's velocity to increase for incompressible flow.

The percent increase in lift coefficient is another valuable reason for studying the ground effect. The magnitude of the increase in lift can be used to classify certain types of aircraft configurations. For example, it has been shown that the amount of ground effect experienced is a function of aspect ratio and wing sweep. Figure 4 shows that aircraft with aspect ratios near 3 can expect a change in lift coefficient around 10% when at a height above ground of $h/b = 0.3$ (18). Since the OGE data ($h/b = 0.93$) was measured at a different Re due to the velocity measurement error and ground plane blockage, the data from this study can not be compared directly to Figure 4. The only reasonable increase in lift occurred below $h/b = 0.3$. The 40 mph test runs showed an increase in lift from $h/b = 0.3$ to $h/b = 0.05$ of 8.6% while the 60 mph test runs increased 14.0% both at an AOA of 6 and 8 deg.

Section 2.2.2 – Drag Coefficient Variation

Unlike the lift coefficient, the drag coefficient generally increased for all four angles of attack measured. Figures Figure 35 and Figure 36 show the effect of the ground plane on the C_D of the chevron UCAV model.
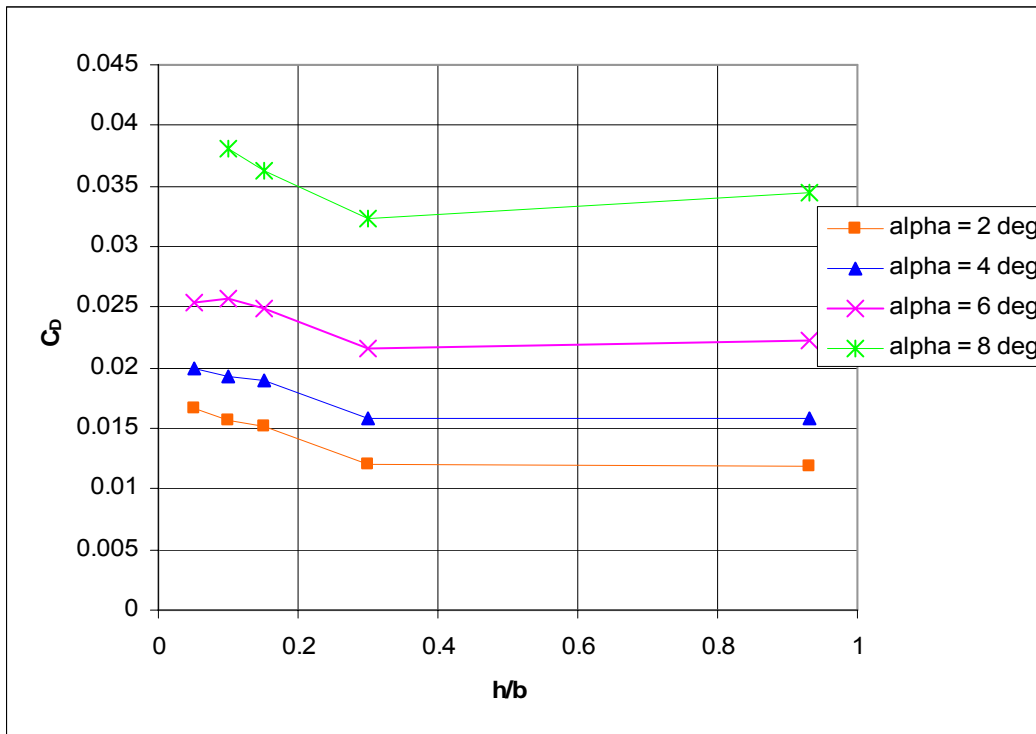
Figure 35: Ground Effect - C_D vs. (h/b) 40 mph
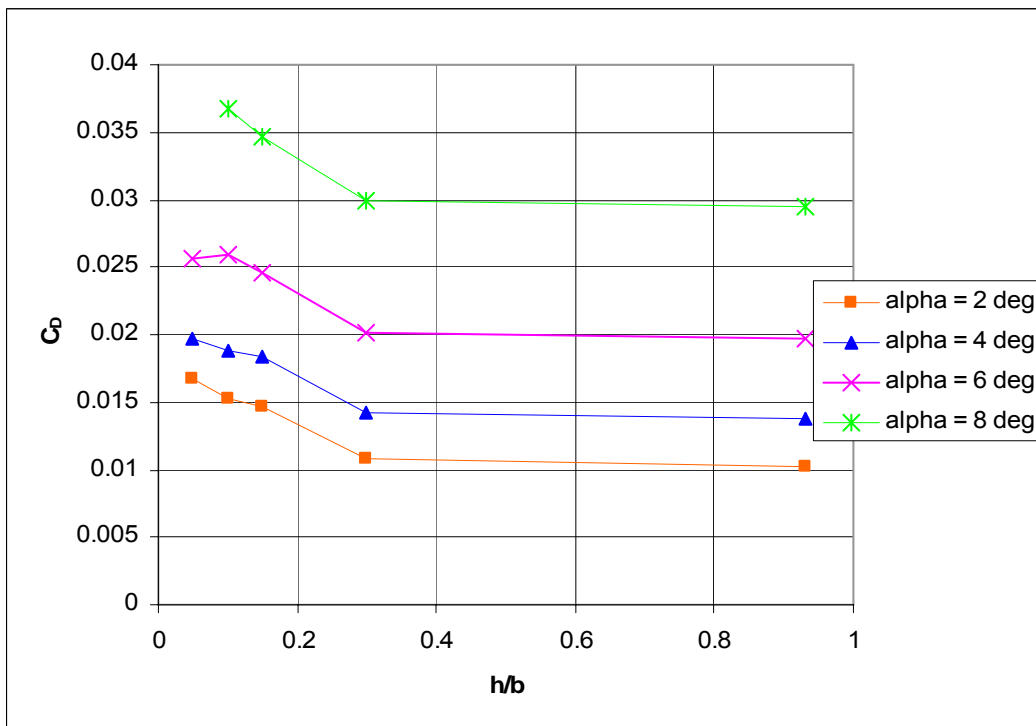
Figure 36: Ground Effect - C_D vs. (h/b) 60 mph

The C_D at all four angles of attack steadily increased roughly at the same rate as height above ground decreased. For the AOA of 6 and 8 deg, this result was expected after noticing the behavior of the lift. The induced drag component of C_D is a function of C_L^2, so when the lift increases as the UCAV enters ground effect, the drag should also increase. However, this relationship was not consistent at all heights above ground. At $h/b = 0.05$, C_D drops slightly at an AOA of 6 deg and possibly at 8 deg, balance limitations prevented the full range of testing at an AOA of 8 deg.

The C_D data shown in Figure 35, specifically for AOA of 6 deg, was applied to the following equation from Bertin (30) in order to analyze the various components of the drag.

$$C_D = C_{D0} + kC_L^2 \qquad [9]$$

Equation [9] assumes a linear relationship between C_D and C_L^2, but the experimental data revealed more of a weak quadratic relationship for all the data gathered. Figure 37 shows this non-linear relationship.
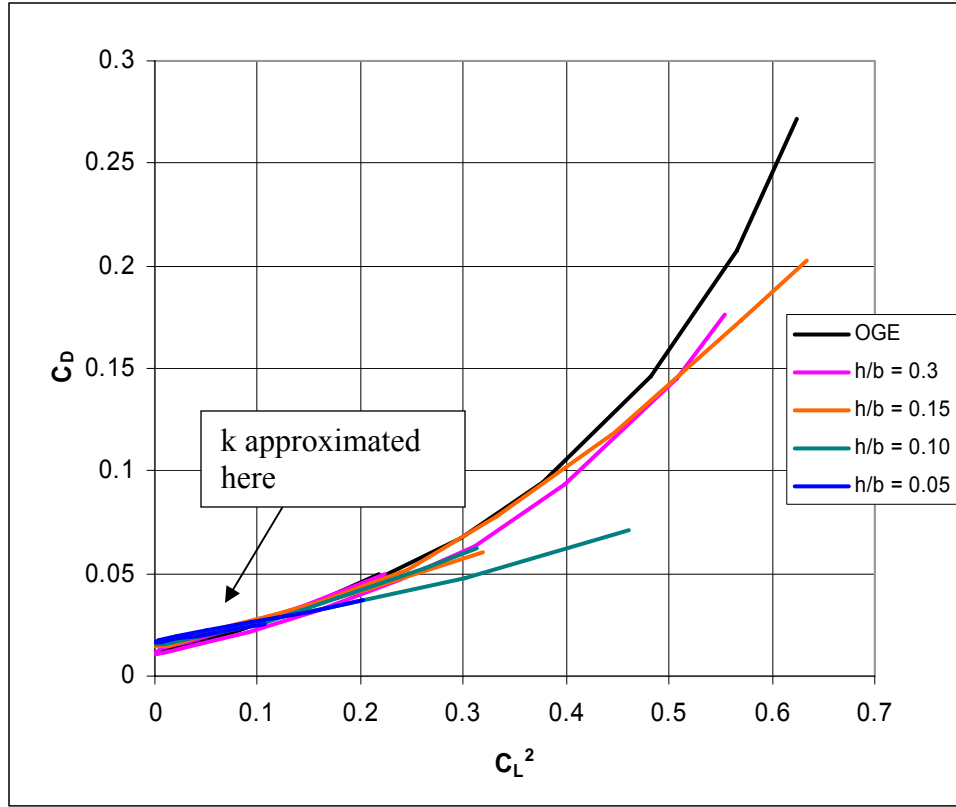
Figure 37: C_D vs. C_L^2 - 40 mph

The factor k, in Equation [9] typically equals the slope of the C_D vs. C_L^2 curve (27), but because of the non-linear relationship in Figure 37, k was approximated to be 0.115 from the nearly linear curves in the lower C_D and C_L^2 region (see arrow in Figure 37).

After k was determined, and the minimum measured C_D was inserted for C_{D0}, the total drag coefficient was calculated. Additionally, McCormick's induced drag factor, Equation [1], was multiplied by the induced drag term of Equation [9] to evaluate the accuracy of its prediction as shown in Equation [10].

$$C_D = C_{D0} + \phi k C_L^2 \qquad [10]$$

Figure 38 shows the total C_D calculated from Equations [9] and [10] plotted adjacent to the C_D measured at an AOA of 6 deg.
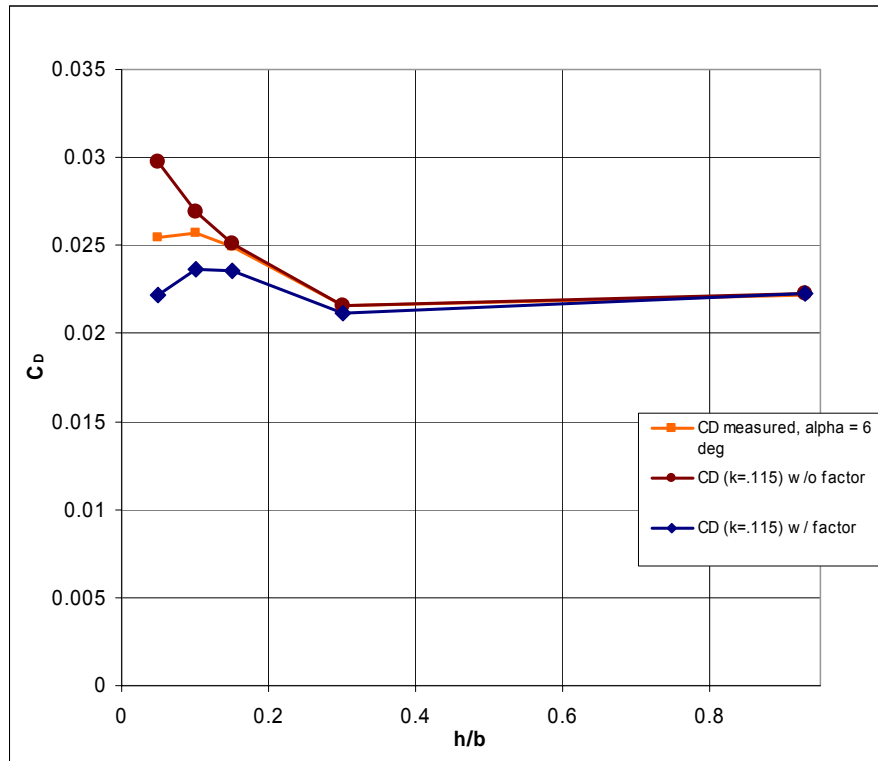
Figure 38: Ground Effect - Induced Drag Factor Comparison, 40 mph

The curves in Figure 38 suggested that McCormick's induced drag factor over predicted the reduction in total drag for the chevron UCAV at 6 deg AOA. This overprediction was because McCormick developed his factor assuming a rectangular wing and inviscid flow conditions.

Without analyzing the viscous forces on the model to quantify the friction drag, it is reasonable to suggest that further investigation be conducted on the wing tip vortices induced by the chevron UCAV. This would provide a better explanation for C_D behavior in the ground effect region.

The percent increase in C_D of the chevron UCAV was on the order of 30% which is comparable to the F-106 model tested by Lee, et al. (20). Curry (6), Curry and Owens (21) found that the Tu-144 and F-16 XL aircraft experienced an increase in drag on the order of 5-15%. This is mentioned to illustrate that other aircraft of similar aspect ratio and wing sweep can experience an increase in C_D while in the ground effect region.

Section 2.2.3 – Lift-to-Drag Ratio Variation

In an effort to draw some conclusions to the above analysis and further understand the complexities of the ground effect region for the chevron UCAV, lift-to-drag ratios (L/D) were calculated. Typically, L/D is directly correlated to aircraft efficiency, and is normally analyzed in ground effect studies to illustrate the improved, or in this case, unimproved efficiency of the ground effect region. Figure 39 and Figure 40 illustrate the negative trend of L/D for the chevron UCAV while in the ground effect region.
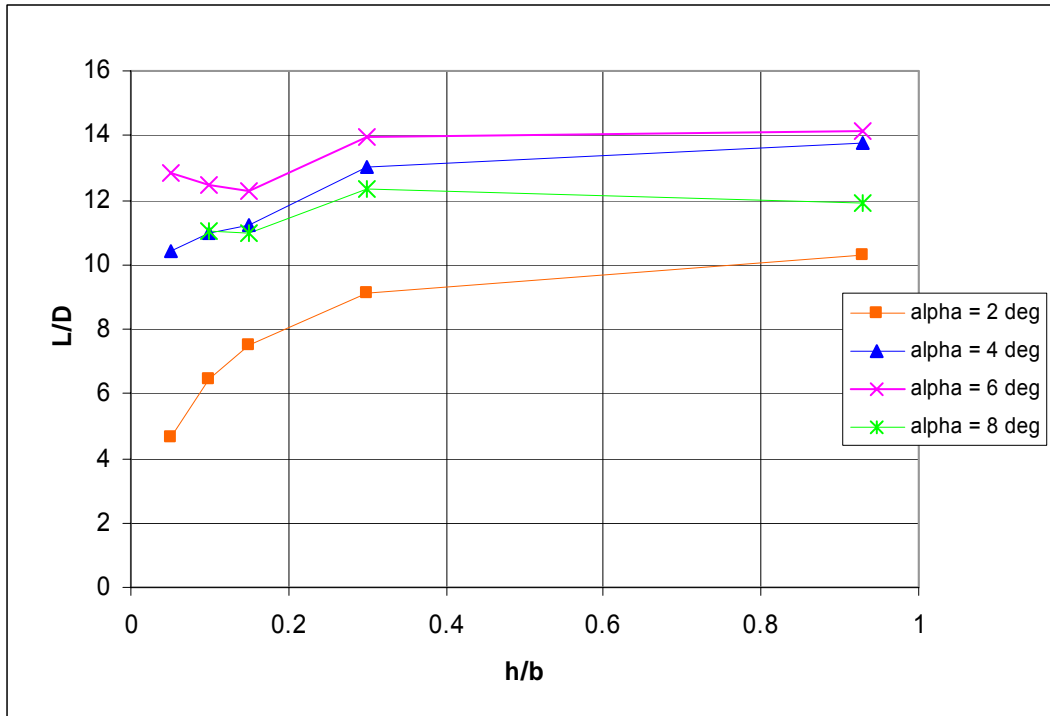
Figure 39: L/D vs. (h/b) 40 mph
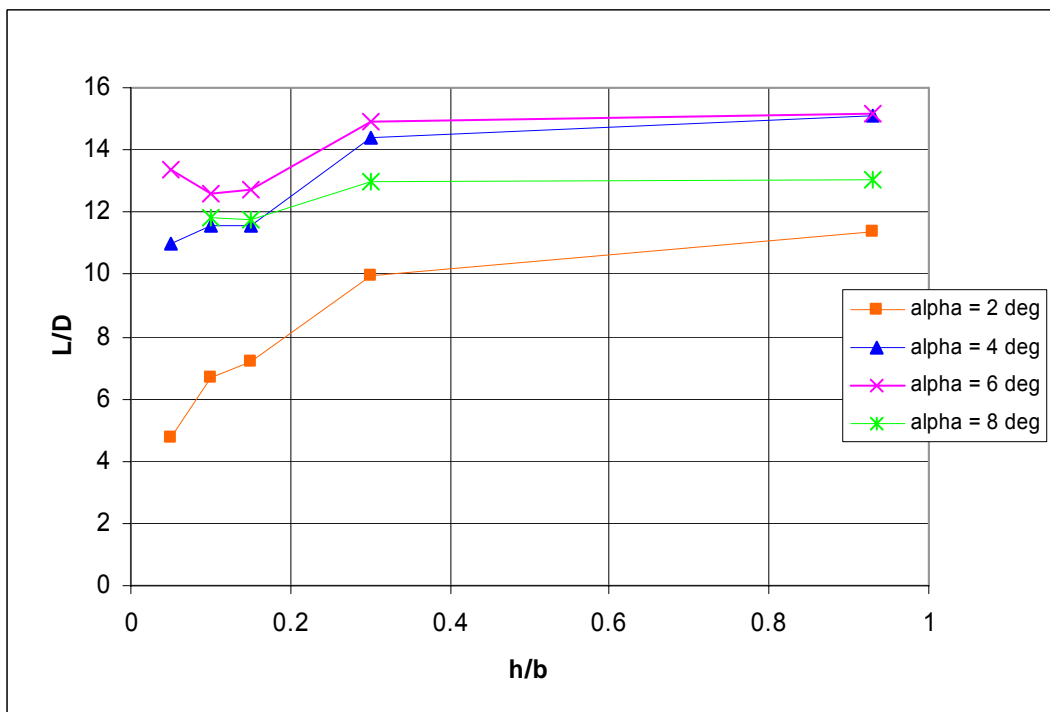
Figure 40: L/D vs. (h/b) 60 mph

62

The only positive slope was at an AOA of 6 deg while at the lowest height above ground. Not only did the AOA of 6 deg have the maximum value for L/D, as seen in Figure 41, it also was the only AOA that experienced a reduction in drag while in close proximity to the ground.
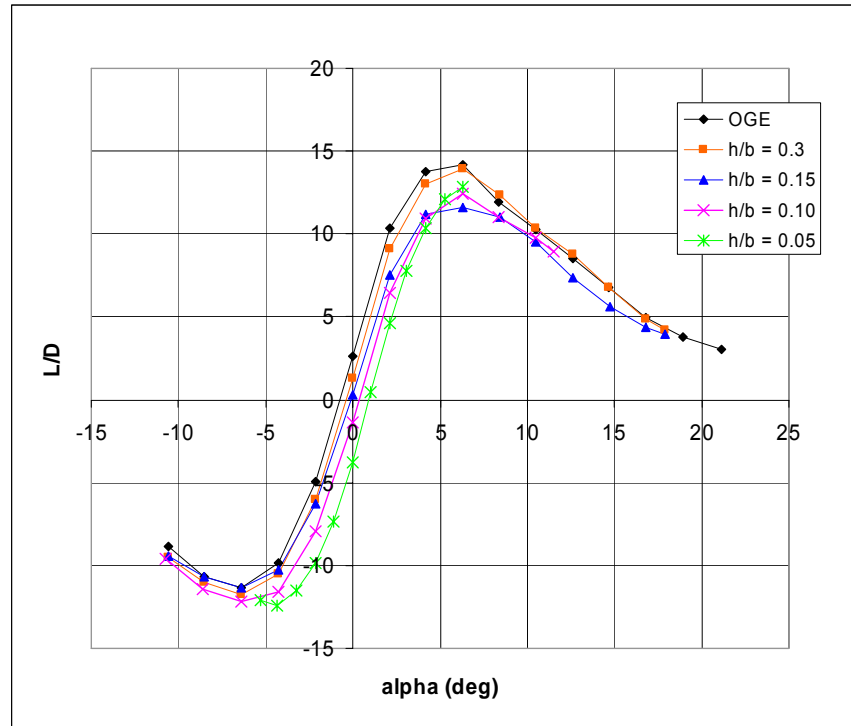
Figure 41: Ground Effect - L/D vs. alpha, 40 mph

Refering to Figures Figure 39 and Figure 40 L/D increased 3.3% at 40 mph and 5.9% at 60 mph at h/b = 0.05. This increase is consistent with the slight decrease in C_D at the same height.

The L/D variation for the chevron UCAV illustrated that the increase in lift at AOA of 6 and 8 deg was not enough to overcome the increase in drag. However, the slight L/D increase at AOA of 6 deg at h/b = 0.05 suggests that possible reduction in

induced drag caused an increased L/D. At AOA of 2 and 4 deg, the decreasing L/D

suggests that the significant loss of lift from the Venturi effect as shown in Figure 30 and

Figure 31 played a role in the L/D variation of the UCAV while in the ground effect

region.

In addition, the increase in C_D played a significant role in the behavior of the L/D

variation for the chevron UCAV and comparisons were drawn from previous studies.

The resulting L/D for the F-106 model decreased (20), and the L/D for the Tu-144 (21)

and F-16 XL (6) increased which can be attributed to differences in percent increase of

C_D as mentioned before.

Section 3 – Test Section Flow Analysis

Section 3.1 – Flow Visualization

To ensure the air flow over the ground plane was uniform, a flow visualization

experiment was conducted. Small tufts were attached on the top surface of the ground

plane covering the leading edge, side edges, across the circular gap, and uniformly across

the remainder of the surface. To see how the tufts were placed on the ground plane refer

to Figure 42 - Figure 44.
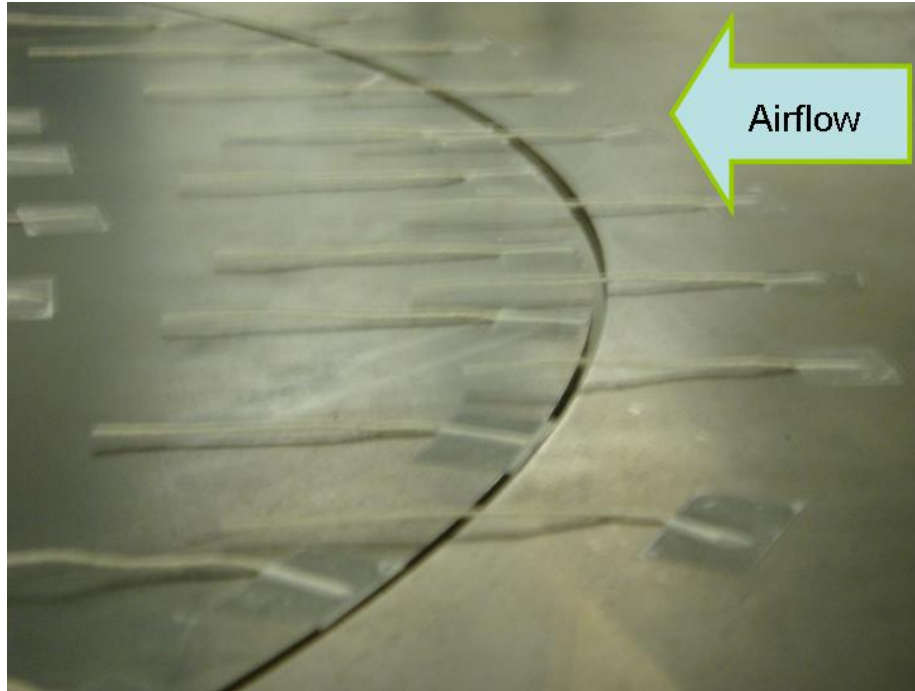
Figure 42: Tufts Across Circular Gap

When the ground plane was mounted in the tunnel test section, the circular piece and the front piece did not exactly fit perfectly together. This imperfection needed to be analyzed, so tufts were placed just before and over the small gap as shown in Figure 42. Since the circular piece was slightly lower than the front piece, the flow beneath the ground plane contacted the front edge and traveled up through the gap. The tufts across the gap illustrated this effect and the tufts downstream of the gap showed that the flow remained uniform not having any apparent effect on the balace data.

Figure 43 is a top view of the model and ground plane during testing.
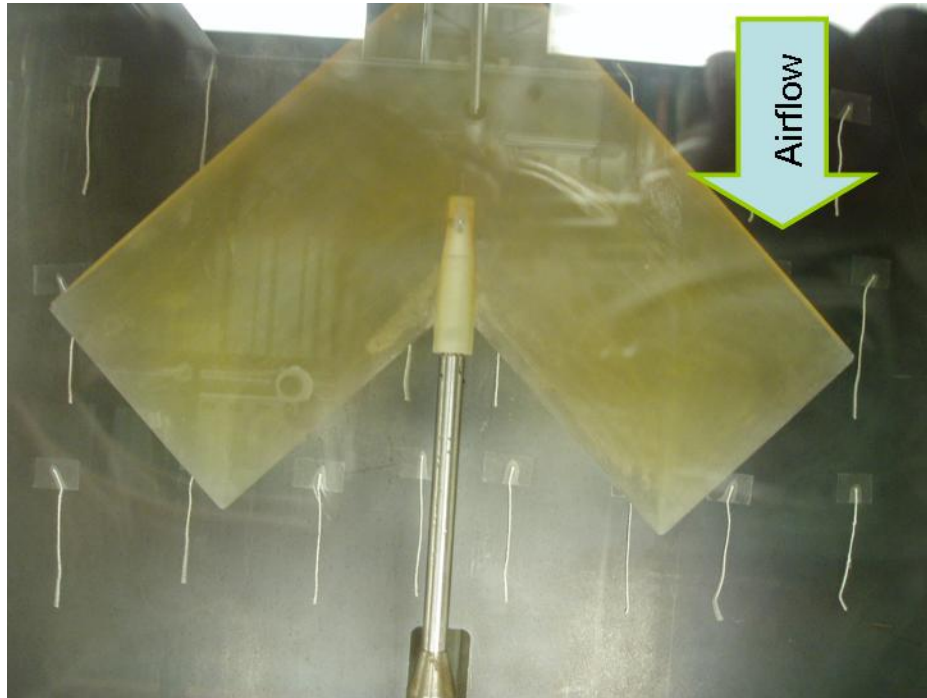
Figure 43: Tufts Beneath the Model

As one can see, the flow was straight and uniform beneath the model which confirmed that no obvious irregularities existed where the balance gathered data.

Another important aspect to analyze was the effect of the cylindrical mounting legs on the flow across the ground plane. Figure 44 illustrates how the flow traveled along the side edges and at the leading edge.
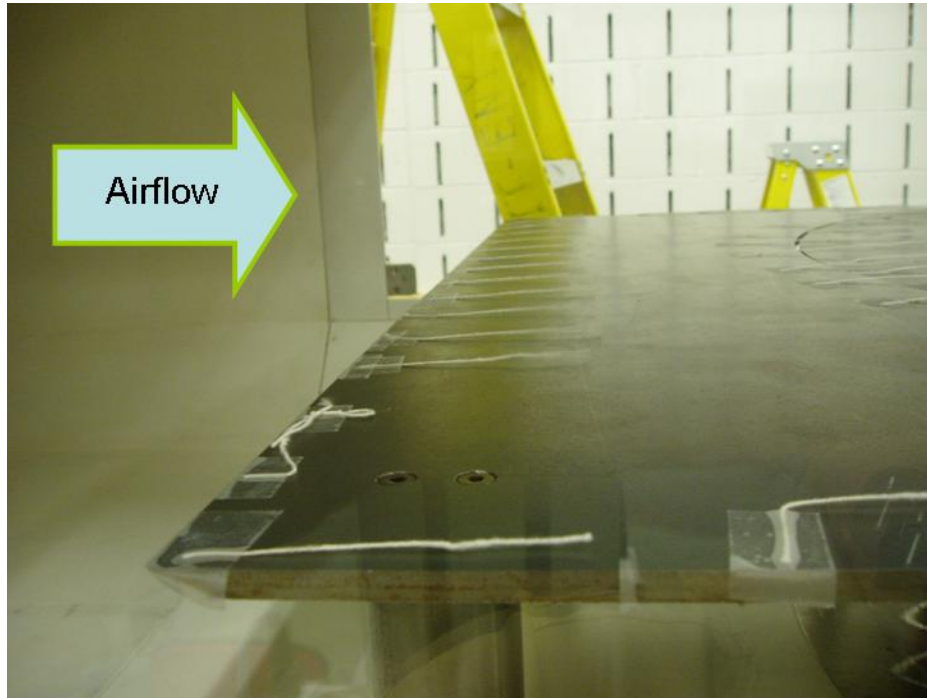
Figure 44: Tufts Attached to Leading and Side Edges

Tufts were placed along each side in order to determine if the flow beneath the ground plane rolled around the side edges. The near tufts in Figure 44 are a good representation of the uniform flow that resulted along the edges of the ground plane, which suggests that the flow beneath the ground plane did not roll over the side edges.

Also shown in Figure 44 is the only unusual outcome from the flow visualization. The second tuft from the side at the leading edge was 90 deg inward and the third tuft from the side edge was 90 deg outward compared to the remainder of the tufts. Although not shown in Figure 44, the tufts above the opposite front leg acted identical to the ones shown. This can best be explained by discussing the horseshoe vortex system that results from the boundary layer on the underside of the flat plate interacting with a circular cylinder (33). In subsonic flow, any disturbance downstream is experienced to some degree upstream as well, which strongly suggests that the effects of the counter-rotating

horseshoe vortices caused the two tufts in Figure 44 to turn towards each other. Although

not shown in Figure 44, the tufts further downstream indicate that the horseshoe vortices

diminished or dampened out prior to the model location, which reduced the likelihood of

this phenomenon affecting the balance data.

Section 3.2 – Boundary Layer Thickness

In order to qualify the data gathered at the low heights above ground, the

boundary layer growth on the ground plane was estimated. Using the incompressible

laminar and turbulent boundary layer equations for a flat plate outlined in Chapter III, the

following results were obtained:

Table 10: Boundary Layer Growth on the Ground Plane

U_∞ (mph)	x_{tr} (ft)	$d_{l.e.}$ (in)	$d_{t.e.}$ (in)	d^* (in)	% disp.
47.2	1.1366	0.2148	0.4809	0.0601	12.4974
68.7	0.7806	0.2760	0.5105	0.0638	12.4976
91.2	0.5880	0.2980	0.5146	0.0643	12.4951
113.1	0.4739	0.3061	0.5109	0.0639	12.5073

Table 10 indicates a relatively consistent turbulent boundary layer and displacement

thickness for the various test speeds. This consistency is attributable to the transition

location moving closer to the leading edge of the ground plane as the velocity increased.

The far right column is the percent of $\delta_{t.e.}$ that δ^* displaces. Since the boundary layer was

not measured, the estimated thicknesses in Table 10 were not validated, but the hot-wire

results suggested a thicker boundary layer than estimated.

While the hot-wire anemometry experiment was not intended to identify the

boundary layer on the ground plane, the results clearly offer a boundary layer thickness

result. During the hot-wire runs with tallest ground plane (h/b = 0.05), there was an

averaged 7% difference in measurements when the probe was at its lowest position

$(z = 2.36 - \text{in})$ compared to the higher readings $(0 \le z \le 1.97 - \text{in})$. Figure 45 illustrates

the probe location relative to the model and the highest ground plane setting.
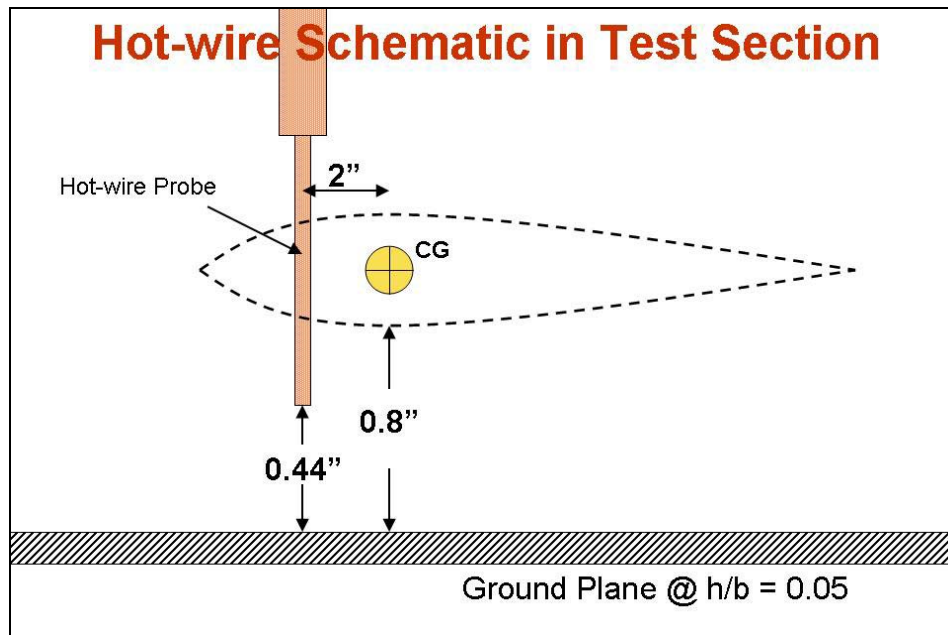
Figure 45: Hot-wire Location in Test Section Relative to Model

As stated in Chapter III, the 2.36-in location of the probe corresponded to a

distance below the model CG of 0.36-in, which means that if the 7% difference is due to

the boundary layer, then the boundary layer thickness could be larger than 0.44-in at the

model CG. Comparing this to the calculated values in Table 10, one can clearly see that

the calculated thicknesses are slightly lower than the hot-wire results which may indicate

that further investigation is necessary in order to accurately identify the boundary layer

build up on the ground plane.

V. Conclusions & Recommendations

Section 1 – Conclusions

Investigating the ground effect region for the chevron UCAV took a lot of coordination, but in the end, all the established goals were achieved. The goals, as explained in Chapter I, will be re-iterated below followed by a discussion of how each goal was met.

The first goal was to expand the test capabilities of the AFIT 3' x 3' wind tunnel by analyzing the flow characteristics through the test section with the ground plane. This was accomplished primarily by three different methods, hot-wire measurements, flow visualization, and boundary layer calculations. The hot-wire results indicated a significant disparity between the indicated transducer speed and the hot-wire measured speed. An average correction factor of 9% was applied to the data reduction program for the test runs without the ground plane. Adding the ground plane revealed more of a difference between indicated transducer speed and the actual speed at the model location in the wind tunnel. Additional correction factors ranging from 3.5 to 7.9% were multiplied by the 9% correction factor to form the complete blockage correction.

The flow visualization results revealed a uniform flow over the top of the ground plane, especially beneath the model. The circular gap where the two pieces of the ground plane came together caused a small updraft of air, but the effect seemed negligible. The only unusual occurrence was at the leading edge directly above the front two cylindrical

legs, which was believed to be the result of the horseshoe vortices that developed at the junction of a cylinder and a flat plate.

The boundary layer build-up across the ground plane was modeled using conventional flat-plate laminar and turbulent boundary layer equations. Beneath the model, which was the area of most concern, the boundary layer was turbulent with an instantaneous transition point well in front of the model. The boundary layer thickness was on the order of 0.5-in, which corresponded to a displacement thickness on the order of 0.06-in. An interesting result from the hot-wire experiments indicated that the boundary layer at the model CG was approximately 0.44-in thick based on an obvious drop in mean velocity.

Since the idea for this project originated with Reed's thesis (8), another goal was to compare his data with the OGE data collected in this study. Although, not all test conditions could be matched due to the constraints of the balance limitations, the data still compared to a reasonable degree of accuracy. Reynolds number differences were the likely reason for the slight variations.

During the experiment, the ground plane had no major installation or testing issues. The airflow traveled across the ground plane with uniform flow, but blockage corrections for wind tunnel speed were necessary. Boundary layer build-up on the ground plane was a concern, but it appeared as though it did not affect the aerodynamic test results.

Identifying the ground effect region for the chevron UCAV planform with respect to height above ground will be the next goal discussed. Force and moment data was collected and reduced to calculate the aerodynamic coefficients while the UCAV was in

71

close proximity to the ground plane. The data was presented by analyzing the change in C_L and C_D near the ground.

The C_L variation with height above ground for AOA of 6 and 8 deg suggested that the chevron UCAV performed as a typical aircraft would according to standard convention. At lower AOA of 2 and 4 deg, the lift responded in the opposite fashion and decreased with the 2 deg case decreasing at a greater rate. This behavior was explained by analyzing the C_P contour plot of the 2-D airfoils in reflection. The negative C_P beneath airfoil suggested that the flow was traveling faster due to the Ventri effect. This higher velocity caused lift to decrease. The trends from a 2-D vortex panel program agreed with the experimental results.

C_D variation with height above ground for AOA equal to 6 deg showed that the drag increased and then decreased as the UCAV got closer to the ground plane. The increase in C_D most likely came from the increase in C_L and the slight decrease at $h/b = 0.05$ was probably because of the flattening out of the wingtip vortices. At lower AOA, C_D increased as height above ground decreased, which was not the expected result since the lift decreased.

Another goal was to verify McCormick's induced drag factor with the experimental results. It was concluded after analyzing the variation in C_D with height above ground that at AOA equal to 6 deg that McCormick's induced drag factor over predicted the decrease in induced drag for the chevron UCAV.

Finally, the last goal of this experiment was to expand the existing aerodynamic database for moderately swept, low aspect ratio, tailless, blended wing body UAVs. This

was accomplished for small angles of attack and low speeds. Further analysis is required to complete the ground effect data for higher angles of attack.

Section 2 - Recommendations

While this thesis only provided a first-cut analysis in many of the aspects studied, it should lay the foundation for further experiments with the chevron UCAV and the ground plane in the AFIT 3' x 3' wind tunnel. Based on the findings of this study, the following are recommendations for further experiments and analysis:

- use a 100-lb balance to expand the test results. Higher angles of attack could be analyzed which would allow for more of a comparison to previous studies;

- take measurements of the boundary layer on the ground plane to better analyze possible effects. Also, measurements or better predictions of the boundary layer transition will further the analysis significantly;

- ensure that the test speed is adjusted properly when testing in the OGE region. The tunnel should be sped up according to the factors calculated in Table 8 for each ground plane height;

- measure the wake and/or vortices shed by the UCAV at all ground plane heights in order to better analyze the reduction in induced drag;

- use another flow visualization technique to verify the findings found in this study;

- set up a boundary layer removal system, such as blowing or sucking air along the top surface of the ground plane, to better simulate an actual aircraft flying over the ground;

- analyze the effects of sideslip and lateral stability of the chevron UCAV in ground effect;

- compare the results found in this study with a dynamic ground effect experiment.

Figure 46: Model & Ground Plane at h/b = 0.3

Figure 47: Ground Plane - Top View & Separated View

Figure 48: Original Chevron UCAV - Top View
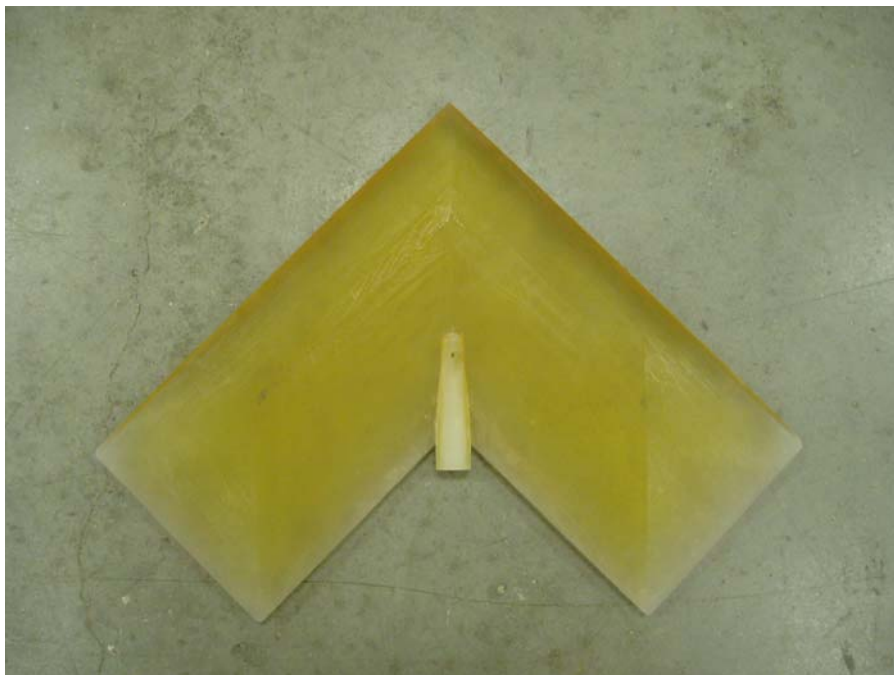
Figure 49: 1/2 Scaled Chevron UCAV

Appendix B: Ground Plane Drawings

Below are the drawings with dimensions of the circular plate, front plate, and the mounting legs for the ground plane.

.020

(30.00°)

DETAIL B
SCALE 1 : 1

B

.250

8X ⌀ .281 THRU ALL
⊔ ⌀ .438 ▼ .127

26.656

⌀35.313

35.313

31.313

2.000

.750
(4X)

1.625

DETAIL A
SCALE 1 : 4
(4X)

A

12.000

B   front gp

SHEET 1 OF 1

8 Pieces of each
DIM 'A' to be: 9.77
12.17
12.97
13.77

4X 1/4-20 ⍏ 1.500

.750

DIM 'A' (inches)

Ø1.500

DETAIL A
SCALE 1 : 1
(2X)

A

		DRAWN		TITLE:
		CHECK'D		
		MFG APPR.		
		ENG APPR.		
		Q.A.		
		COMMENTS:		

SIZE | DWG. NO. | REV
B | shaft |
SCALE: 1:2 | WEIGHT: | SHEET 1 OF 1
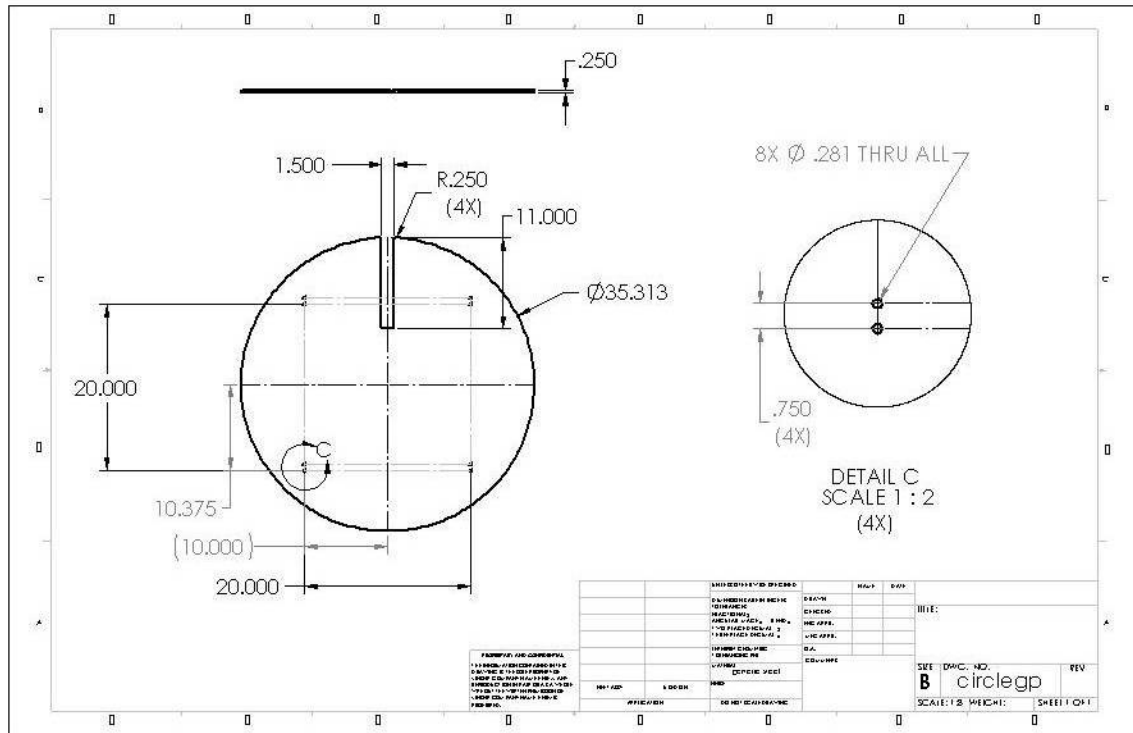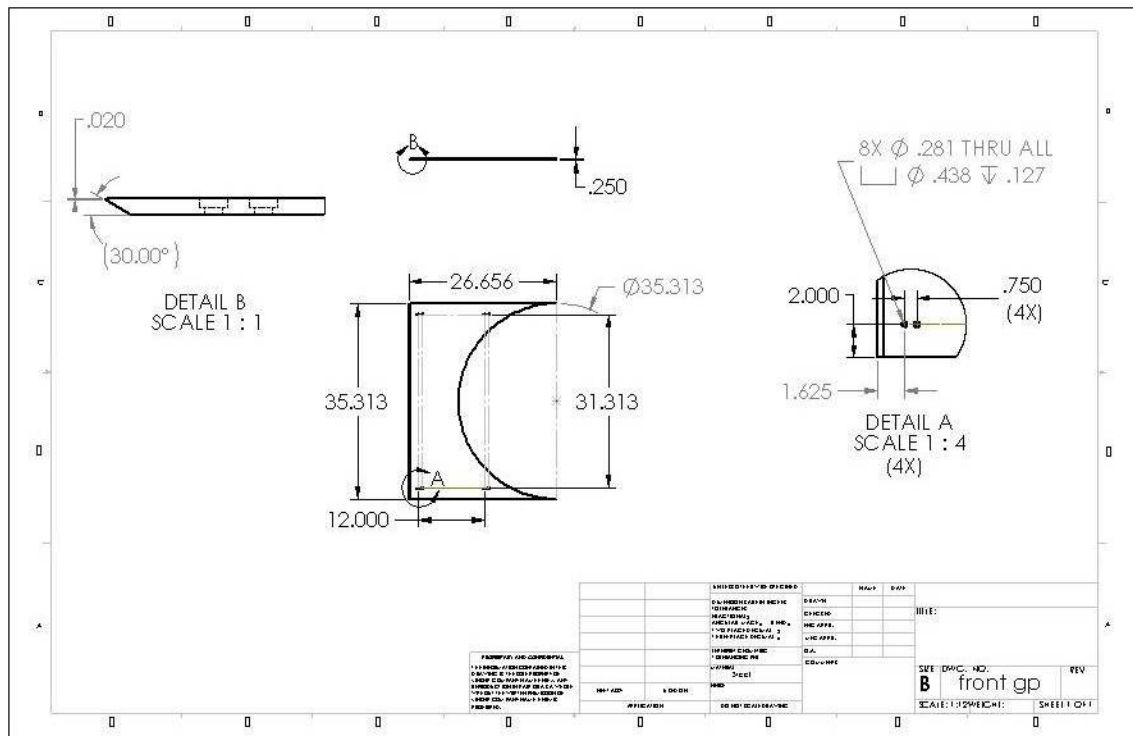
Appendix C: Data Reduction Sample Calculation

The following is a sample calculation for the MATLAB$^{©}$ data reduction program

used for this experiment for the following test condition:

$$U_\infty = 40 \text{ mph}$$
$$h\!\!\!/_b = 0.15$$
$$\alpha = 6 \text{ deg}$$

Test room conditions and model specifics:

$$T = 533.7 \ ^\circ\text{R}$$
$$P = 14.066 \text{ psia}$$
$$R = 1716 \ \tfrac{\text{ft-lb}_f}{\text{slug-R}}$$
$$\mu = 0.372\text{x}10^{-6} \ \tfrac{\text{slug}}{\text{ft-sec}}$$
$$c_r = 0.6183 \text{ ft}$$
$$S = 0.607 \text{ ft}^2$$
$$b = 1.333 \text{ ft}$$
$$AR = \frac{b^2}{S} = 2.93$$
$$\gamma = 1.4$$
$$\rho = \frac{P}{R*T} = 0.0022 \, \tfrac{\text{slugs}}{\text{ft}^3}$$
$$q_\infty = \frac{1}{2}*\rho*U_\infty^2 = 3.633 \ \tfrac{\text{lb}_f}{\text{ft}^2}$$
$$a = \sqrt{\gamma*R*T} = 1132.3 \ \tfrac{\text{ft}}{\text{sec}}$$

Blockage / Velocity Corrections:

$$\varepsilon = \text{blockage correction term}$$
$$sb = \text{solid blockage}$$
$$gp = \text{ground plane}$$
$$tc = \text{transducer correction}$$
$$K_1 = \text{body shape factor} = 1.04$$
$$\tau_1 = f(\text{test section shape} \ \& \ \frac{2b}{B}) = 0.86$$
$$Wing \ volume = Body \ volume = 0.03668 \ \text{ft}^3$$
$$C = \text{tunnel cross section area} = 9.4722 \ \text{ft}^2$$
$$\varepsilon_{sb,wing} = \frac{K_1 * \tau_1 * Wing \ volume}{C^{3/2}} = 0.001125$$
$$\varepsilon_{gp} = 1.077 \ (\text{calculated from hot-wire results})$$
$$\varepsilon_{tc} = 1.090 \ (\text{calculated from hot-wire results})$$
$$\varepsilon_{Total} = \varepsilon_{sb} + \left(\varepsilon_{gp} * \varepsilon_{tc} - 1 \right) = 0.17476$$

Note: solid blockage correction equations taken from Barlow, et al. (27)

Calculating the flight parameters with corrections applied:

$$U_{\infty,corr} = U_{\infty} * (1 + \varepsilon_{Total}) = 67.4286 \tfrac{\text{ft}}{\text{sec}} = 45.9740 \ \text{mph}$$
$$q_{\infty,corr} = q_{\infty} * (1 + \varepsilon_{Total})^2 = 5.0279 \ \tfrac{\text{lb}_f}{\text{ft}^2}$$
$$M = \frac{U_{\infty,corr}}{a} = 0.0593$$
$$\text{Re} = \frac{\rho * U_{\infty,corr} * c_r}{\mu} = 2.468 \text{x} 10^5$$

The raw data from the control computer contained the following measurements:

[N_1, N_2, S_1, S_2, A_1, ℓ]. These force and moment measurements were subtracted from the

tare effects and corrected for the balance interactions. Refer to DeLuca (26) or Rivera

(29) see a complete procedure of data reduction program. The remainder of the sample

calculation will carry on after the balance and tare effects were removed from the inputted data.

The corrected data was originally in the UCAV's body axis frame. The following equations converted the drag, side, and lift forces $\begin{bmatrix} D & S^* & L \end{bmatrix}$; and roll, pitch, and yaw moments $\begin{bmatrix} \ell & m & n \end{bmatrix}$ into the wind axis frame:

$$\begin{bmatrix} D \\ S^* \\ L \end{bmatrix}_{wind} = \begin{bmatrix} A*\cos\theta*\cos\psi + Y*\sin\psi + N*\sin\theta*\cos\psi \\ -A*\sin\psi*\cos\theta + Y*\cos\psi - N*\sin\theta*\sin\psi \\ -A*\sin\theta + N*\cos\theta \end{bmatrix}$$

$$\begin{bmatrix} \ell \\ m \\ n \end{bmatrix}_{wind,bc} = \begin{bmatrix} \ell*\cos\theta*\cos\psi - m*\sin\psi + n*\sin\theta*\cos\psi \\ \ell*\sin\psi*\cos\theta + m*\cos\psi + n*\sin\theta*\sin\psi \\ -\ell*\sin\theta + n*\cos\theta \end{bmatrix}_{body,bc}$$

where:

$A = A_1$ corrected $= -0.02698$ lb$_f$

$Y = S_1$ corrected $= 0.00122$ lb$_f$

$N = N_1$ corrected $= 0.93839$ lb$_f$

$\ell = \ell$ corrected $= 0.02889$ lb$_f$-in

$m = N_2$ corrected $= 2.28160$ lb$_f$-in

$n = S_2$ corrected $= 0.03048$ lb$_f$-in

θ= pitch angle (AOA) $= 0.1078$ rads $= 6.17$ deg

ψ= yaw angle $= -0.7330 \times 10^{-3}$ rads $= -0.042$ deg (negligible)

Carrying out the above force equations for drag and lift: (side force was treated as negligible and not used in the analysis)

$$D = 0.07409 \text{ lb}_f$$
$$L = 0.93585 \text{ lb}_f$$

Before the moments were calculated, the reference point was adjusted from the balance CG to the model CG. The chevron UCAV's CG was found in the Solid Works$^{©}$ program and verified by hanging it with a small string through the drilled balance holes.

Since the model CG was located along the x-axis, the $\bar{y}$ and $\bar{z}$ locations were zero. The following were the equations used to correct the pitching moment: (roll and yaw moment were negligible and not used in the analysis).

$$m_{wind,bc} = 2.28156 \text{ lb}_f - \text{in}$$

$$X_{cg,dist} = \text{dist. between model CG and balance CG} = 1.3725 \text{ in}$$

$$X_{cm} = X_{cg,dist} * \left[\cos(\theta + \not{w}^0) + \tan \psi \right] = 1.3645 \text{ in}$$

where:

w = angle between X_{cg} and x-axis at $\alpha = 0$

$$m_{cg} = m_{wind,bc} - L * X_{cm} + D * \not{Z}^0_{cm} = 1.02632 \text{ lb}_f - \text{in}$$

Non-dimensionalizing the lift and pitching moment yields:

$$\boxed{\begin{array}{l} C_{L_w} = \dfrac{L}{q_{\infty,corr} * S} = 0.3067 \\[3mm] C_{m_{cg}} = \dfrac{m_{cg}}{q_{\infty,corr} * S * c} = 0.06467 \end{array}}$$

These values for lift and moment coefficient agree to those in Table 13 to 0.02%.

The drag coefficient was corrected for test section geometry and flow field interference as such:

$$\delta = \frac{b}{\text{Tunnel span } (B)} = 0.3636$$

$$\Delta C_{D_w} = \frac{\delta * S}{C} (C_{L_w})^2 = 0.00219$$

The final drag coefficient is as follows:

$$C_{D_u} = \frac{D}{q_{\infty,corr} * S}$$

$$\boxed{C_{D,corr} = C_{D_u} + \Delta C_{D_w} = 0.02647}$$

The corrected drag coefficient disagrees with the value in Table 13 by 6.07%. This was due to an incorrect model span-to-test section width ratio, δ. The δ used for the C_D in Table 13 was 0.1125, which was from a previous experiment.

Appendix D: Additional Ground Effect Plots
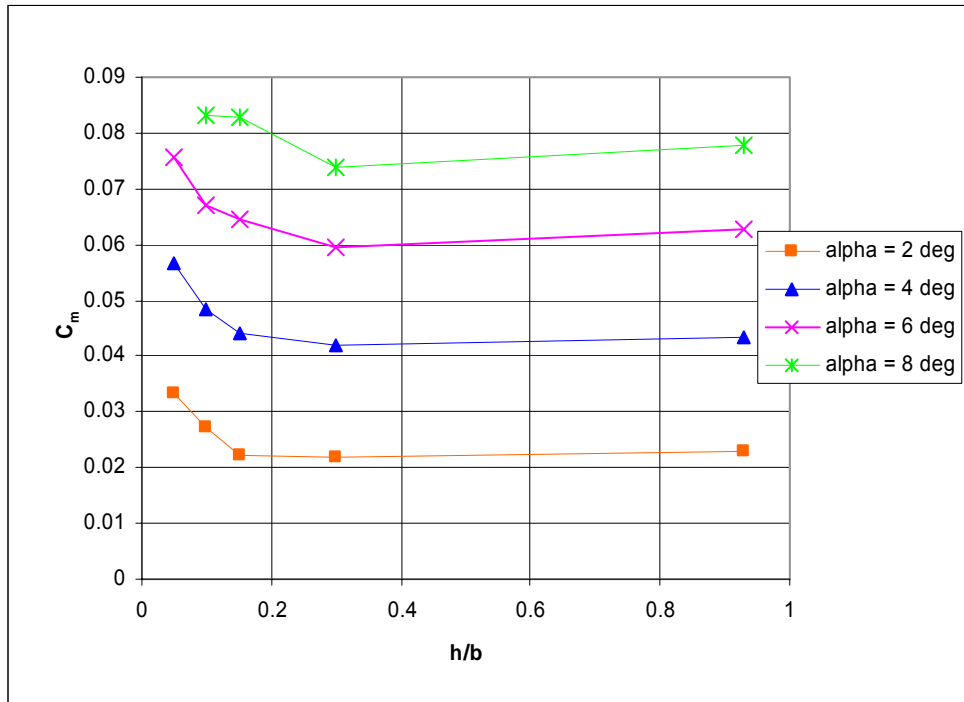
Figure 50: C_m vs. (h/b) 40 mph
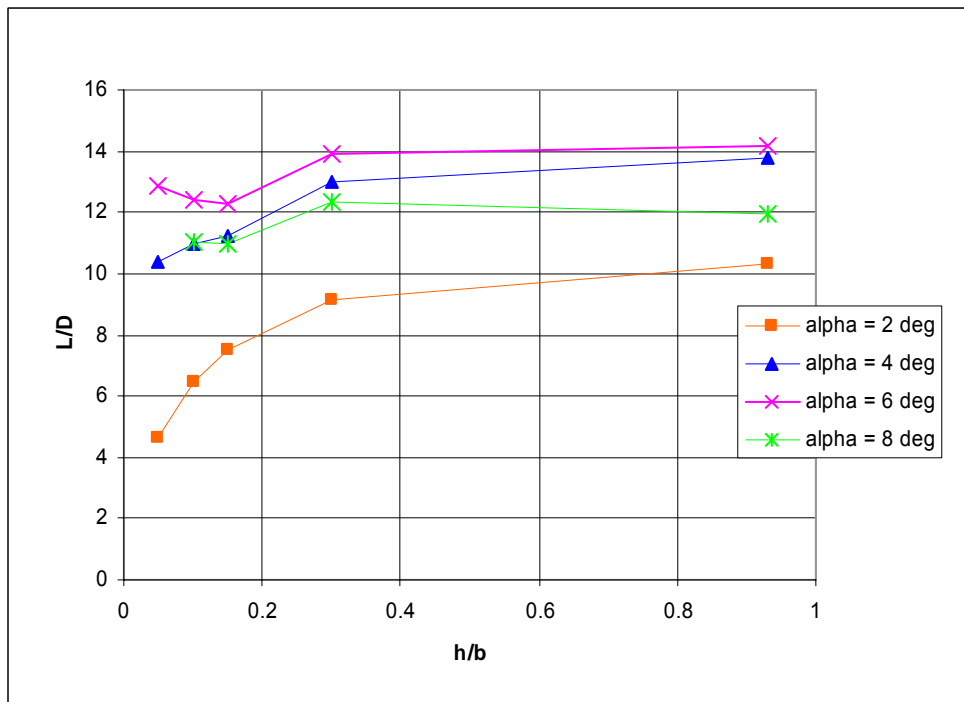
Figure 51: L/D vs. (h/b) 40 mph
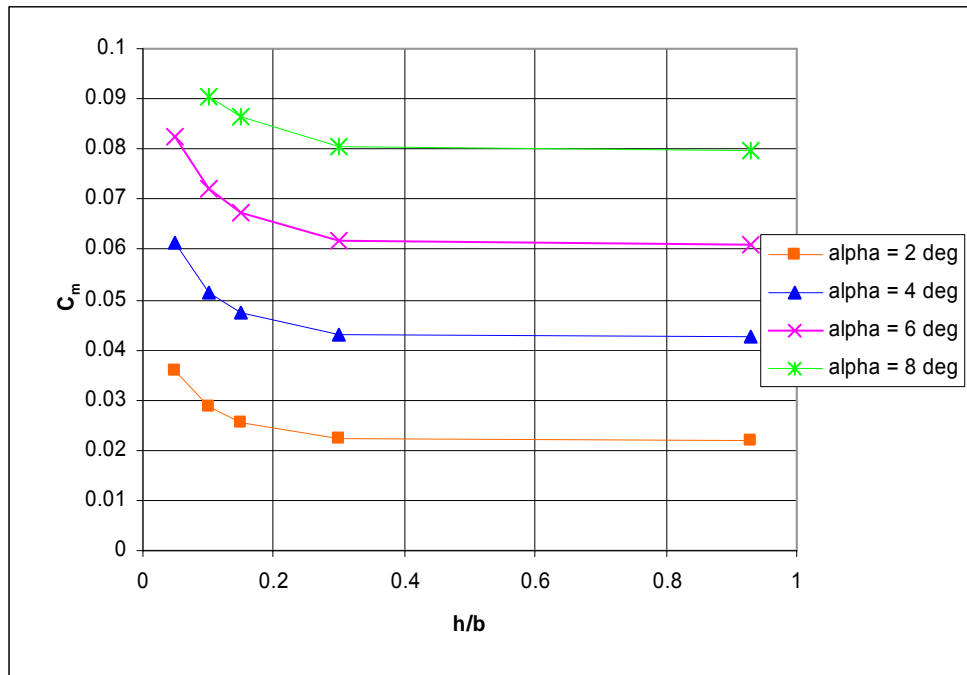
Figure 52: C_m vs. (h/b) 60 mph
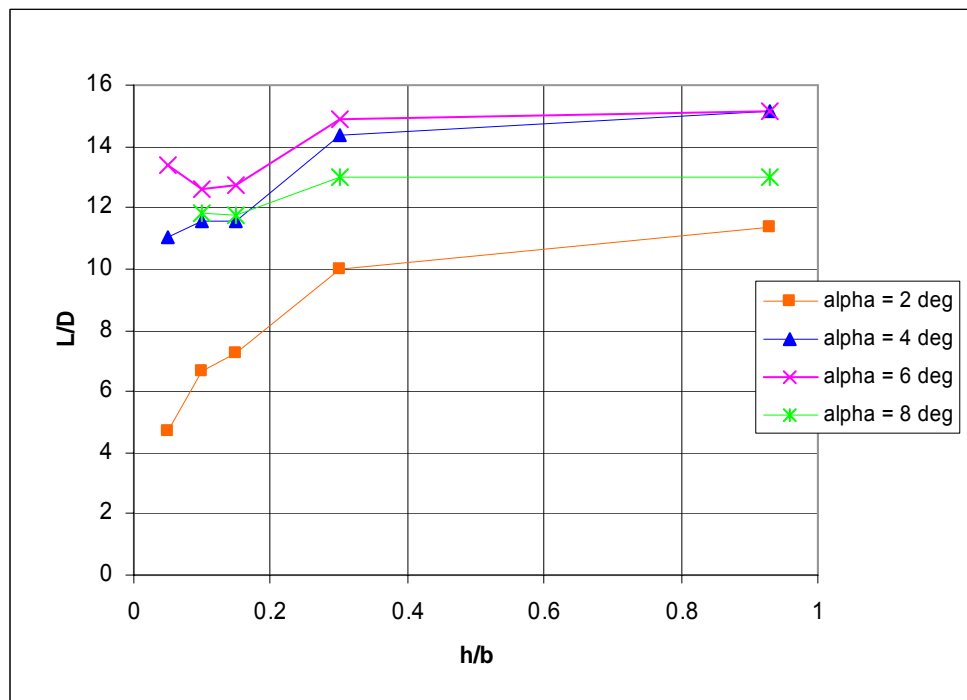
Figure 53: L/D vs. (h/b) 60 mph
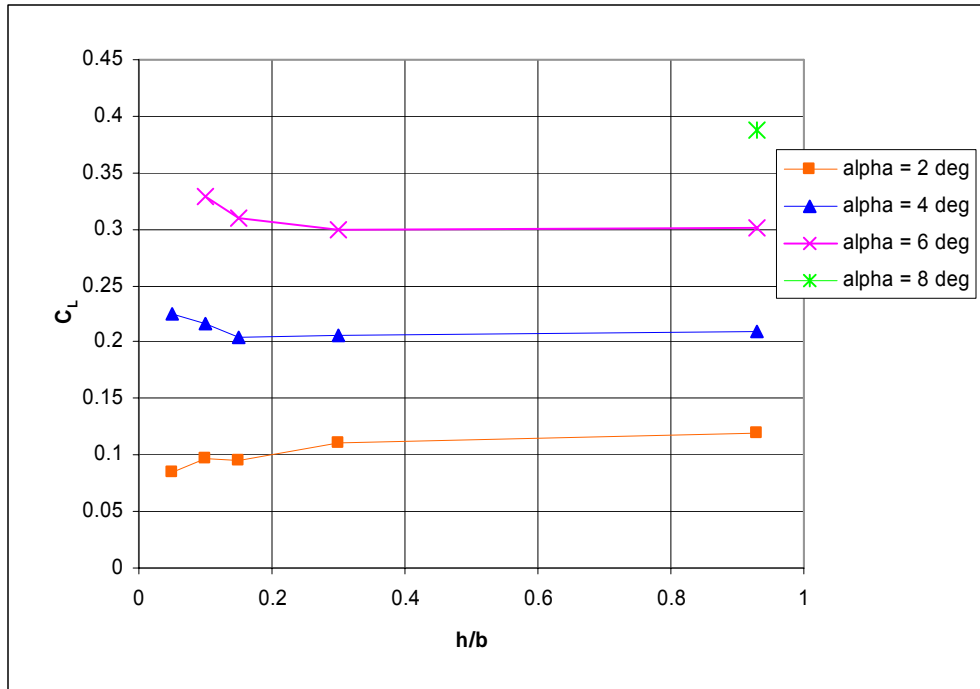
Figure 54: C_L vs. (h/b) 80 mph
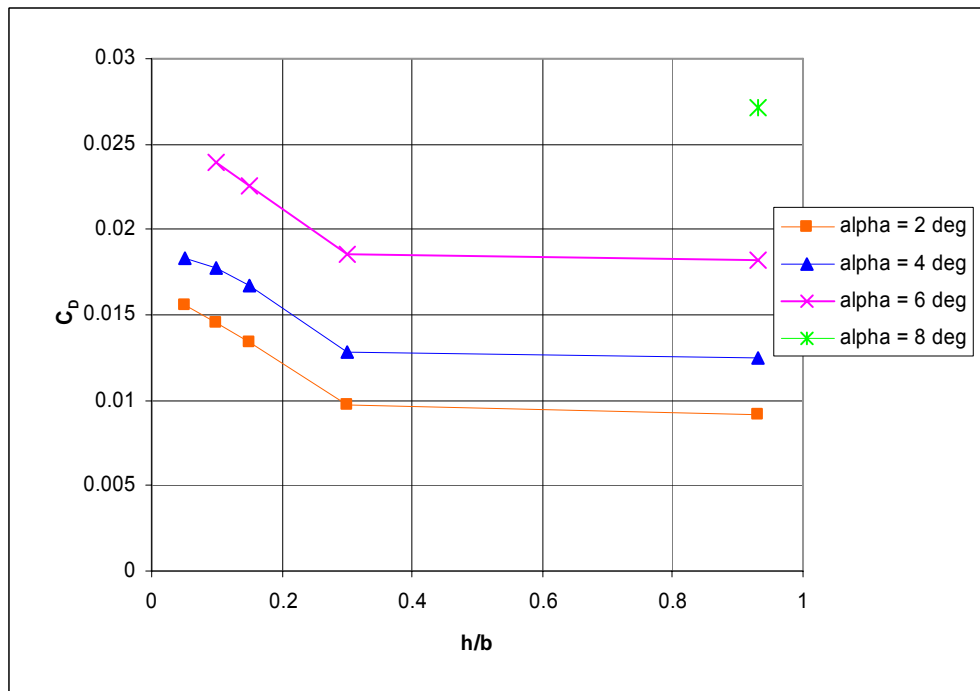
Figure 55: C_D vs. (h/b) 80 mph

86
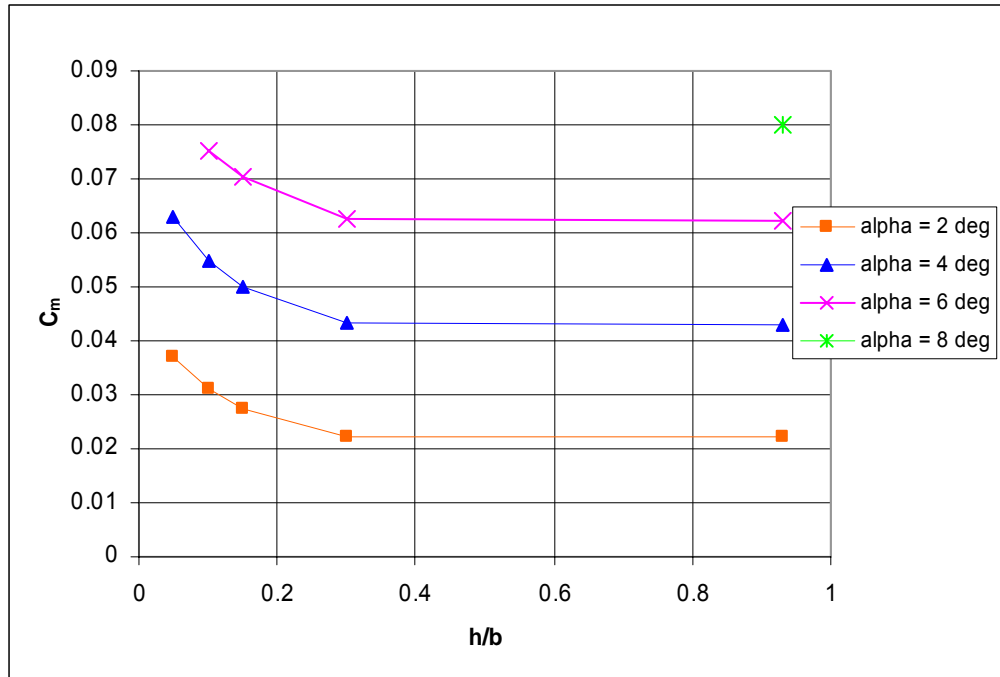
Figure 56: C_m vs. (h/b) 80 mph
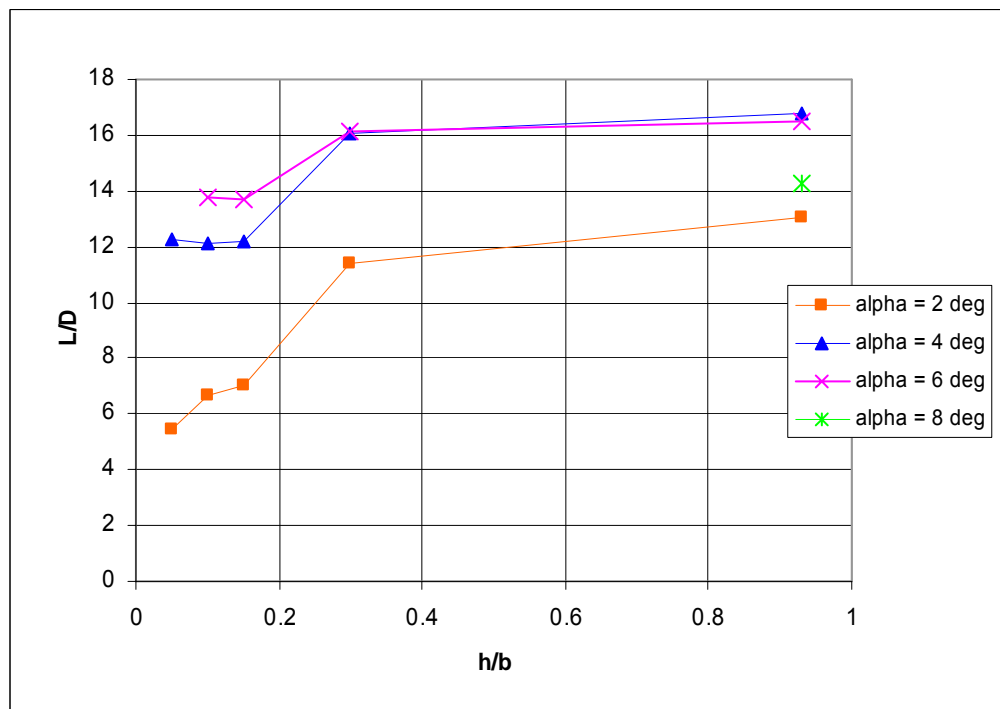
Figure 57: L/D vs. (h/b) 80 mph

87
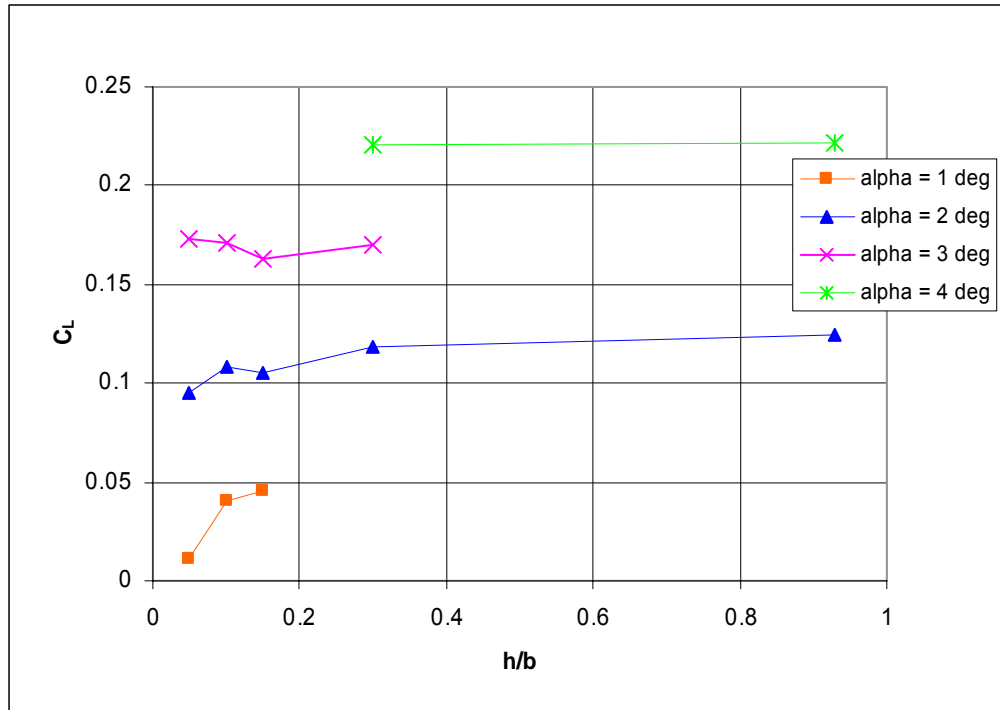
Figure 58: C_L vs. (h/b) 100 mph
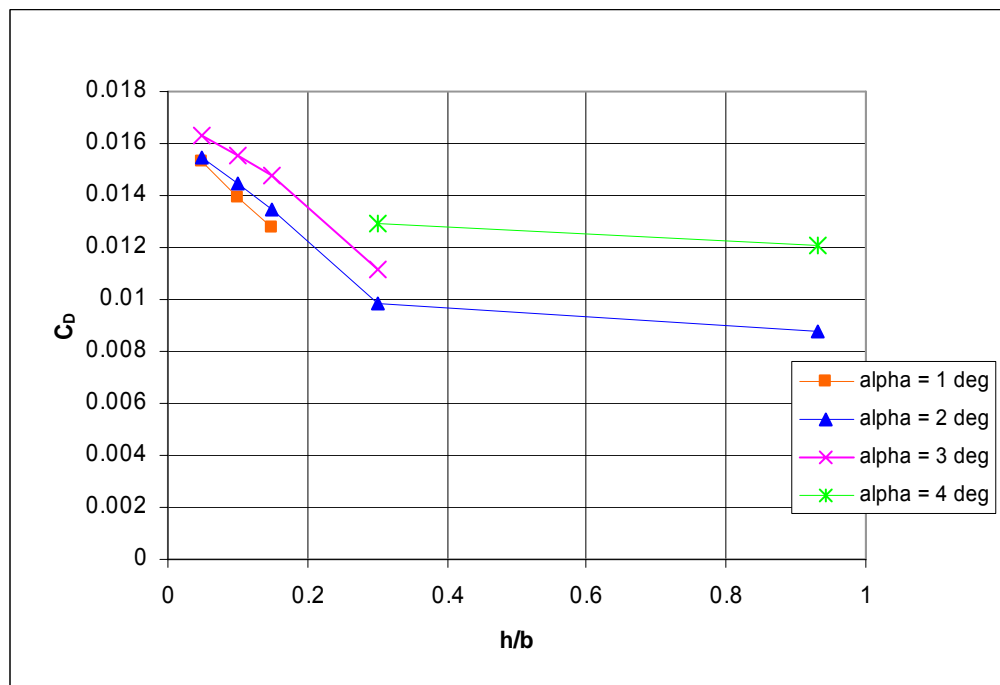
Figure 59: C_D vs. (h/b) 100 mph
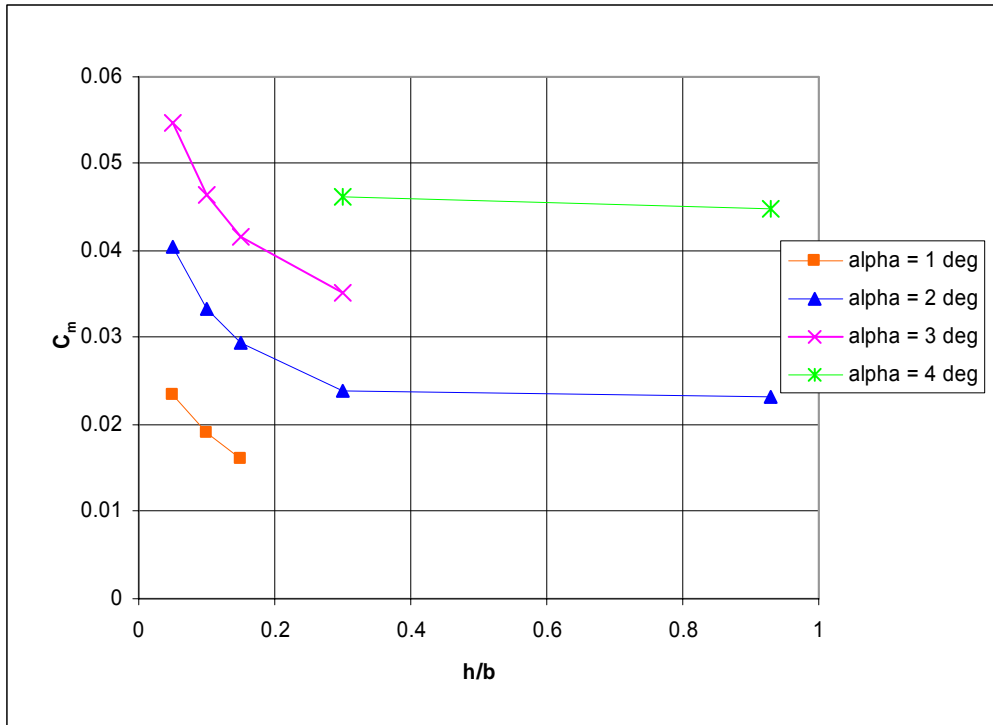
Figure 60: C_m vs. (h/b) 100 mph
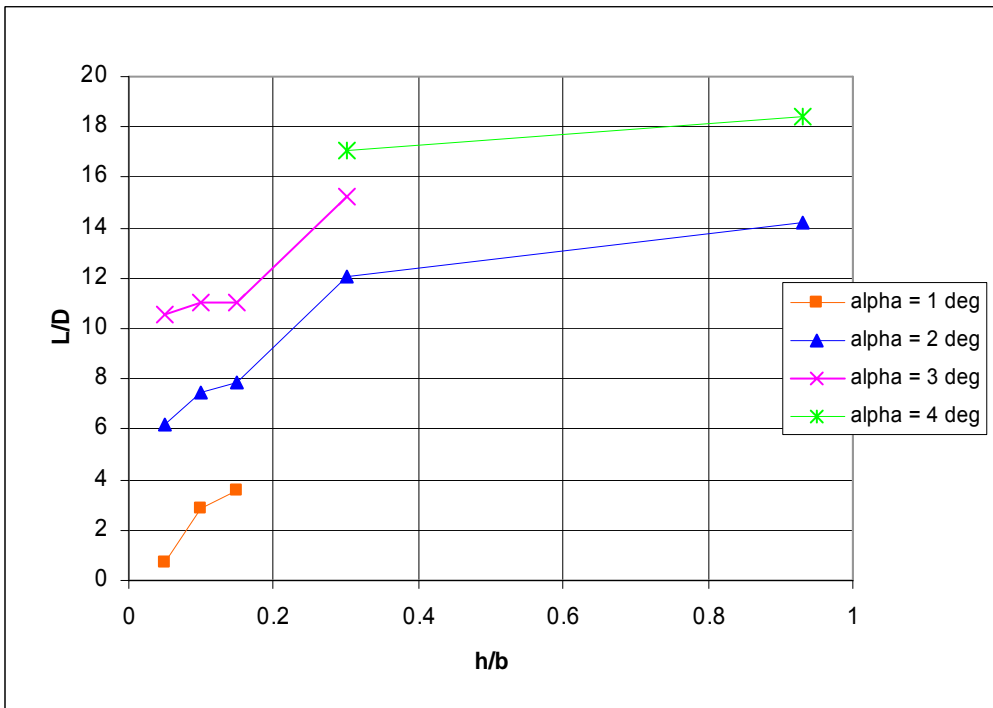
Figure 61: L/D vs. (h/b) 100 mph

89

Appendix E: Data Tables

The following tables were outputted from the data reduction program and used in the various plots.

Table 11: U=40mph, h/b=0.93 (OGE)

Mach No.	Re No.	q_c	Uoo	alpha_c	C_L	C_D_c	Cm_cg_c_w
0.0563493	236768.77	4.552549	43.582136	-10.615979	-0.4381711	0.0497466	-0.1019676
0.0563106	236605.89	4.5462878	43.552156	-8.4921887	-0.3490984	0.032759	-0.0854758
0.0563351	236709.03	4.5502521	43.571141	-6.3663688	-0.2551106	0.022517	-0.0657581
0.0562854	236500.04	4.542221	43.532672	-4.2383831	-0.1558793	0.0158532	-0.0459407
0.0562991	236557.63	4.5444333	43.543272	-2.1134549	-0.0640505	0.0128971	-0.0223047
0.0562916	236526.15	4.543224	43.537479	0.0119977	0.0290479	0.0109529	0.0001788
0.0563967	236967.54	4.5601963	43.618725	2.1376353	0.1225942	0.011881	0.0230624
0.0564334	237121.94	4.5661406	43.647145	4.1772696	0.2185537	0.0158927	0.0434659
0.0565494	237609.19	4.5849255	43.736834	6.3038083	0.3142817	0.0221855	0.0626314
0.056618	237897.44	4.5960565	43.789893	8.3438496	0.4112267	0.0344661	0.0777312
0.0566265	237933.42	4.5974467	43.796515	10.46777	0.5006149	0.0488721	0.0921763
0.0565943	237798.03	4.592216	43.771593	12.585331	0.5746081	0.0673504	0.1074878
0.0565639	237670.13	4.5872777	43.748051	14.700686	0.6432585	0.0948725	0.1192471
0.056497	237389.19	4.5764391	43.696338	16.820896	0.7236637	0.1457652	0.1154166
0.056456	237217	4.5698023	43.664642	18.931549	0.7809298	0.2073778	0.1105949
0.0563436	236744.6	4.5516198	43.577688	21.121387	0.819275	0.272025	0.1052759

Table 12: U=40mph, h/b=0.3

Mach No.	Re No.	q_c	Uoo	alpha_c	C_L	C_D_c	Cm_cg_c_w
0.0595242	250108.68	5.0799957	46.037621	-10.543224	-0.4726612	0.0496823	-0.1038341
0.0595414	250181.08	5.0829372	46.050947	-8.5043255	-0.3784832	0.034387	-0.0866243
0.0595492	250213.96	5.0842734	46.057	-6.3763665	-0.2793164	0.0237172	-0.0668002
0.0596104	250471.16	5.0947311	46.104342	-4.2464026	-0.1752955	0.0167032	-0.0466206
0.0596077	250459.62	5.0942618	46.102219	-2.1198819	-0.0796111	0.0133039	-0.0229263
0.0596595	250677.38	5.1031237	46.142301	0.006069	0.0146938	0.0111745	-0.000552
0.0597716	251148.4	5.1223195	46.229003	2.1323407	0.1097754	0.0120349	0.0217864
0.0597909	251229.48	5.125627	46.243926	4.1717388	0.205163	0.0157753	0.0420166
0.0597393	251012.81	5.11679	46.204045	6.2983392	0.3010403	0.0216025	0.0596263
0.0596864	250790.58	5.1077338	46.163139	8.4258721	0.3991755	0.0322993	0.0739897
0.0595626	250270.08	5.086554	46.067329	10.461831	0.4862361	0.047098	0.0873635
0.0594261	249696.56	5.0632682	45.961761	12.578724	0.5586114	0.0637984	0.1032196
0.0593604	249420.6	5.0520827	45.910965	14.69606	0.6320582	0.0930992	0.1120012
0.059236	248897.84	5.0309276	45.814741	16.816369	0.7127031	0.1454652	0.1058869
0.0592598	248997.84	5.0349711	45.833148	17.87255	0.7446167	0.1760877	0.1027293

Table 13: U=40 mph, h/b=0.15

Mach No.	Re No.	q_c	Uoo	alpha_c	C_L	C_D_c	Cm_cg_c_w
0.0592916	246886.83	4.9860239	45.775671	-10.58134	-0.5649449	0.0600204	-0.130368
0.0593069	246950.36	4.9885901	45.787449	-8.5347541	-0.4521546	0.0422714	-0.1052752
0.0593351	247067.61	4.9933283	45.809189	-6.3980328	-0.3317732	0.0293093	-0.0782914
0.0593534	247144.16	4.9964232	45.823383	-4.2642517	-0.2185103	0.02125	-0.051346
0.0594209	247425.05	5.0077866	45.875462	-2.1307351	-0.1058881	0.0167997	-0.0251015
0.0594615	247594	5.014628	45.906787	0.0018163	0.0043975	0.0143157	-0.000707
0.0595227	247849.12	5.0249675	45.95409	2.13378	0.1132601	0.0150956	0.0223403
0.0595636	248019.19	5.0318661	45.985623	4.17506	0.2132041	0.0190337	0.0440588
0.0595458	247945.24	5.0288658	45.971912	6.3006456	0.3066244	0.0249541	0.0646564
0.0594446	247523.83	5.011786	45.893777	8.4254263	0.3980962	0.0362443	0.0829548
0.0593805	247256.62	5.0009713	45.844234	10.465052	0.4940338	0.0520775	0.0965756
0.0592909	246883.87	4.9859044	45.775122	12.585908	0.5760055	0.0778245	0.1095503
0.0591293	246210.89	4.9587589	45.650342	14.711443	0.6693032	0.118345	0.1146984
0.059026	245780.79	4.9414497	45.570598	16.83377	0.754832	0.1730153	0.1154539
0.0589733	245561.13	4.9326208	45.52987	17.893599	0.795579	0.2027972	0.1147111

Table 14: U=40 mph, h/b=0.10

Mach No.	Re No.	q_c	Uoo	alpha_c	C_L	C_D_c	Cm_cg_c_w
0.0593961	247339.46	5.0033435	45.850618	-10.715638	-0.6794595	0.0708169	-0.1606285
0.0594063	247381.67	5.0050512	45.858442	-8.5747996	-0.5491094	0.0481446	-0.1227567
0.0594745	247665.64	5.0165482	45.911082	-6.4297099	-0.4084673	0.0334862	-0.0862726
0.0594555	247586.66	5.0133494	45.896442	-4.2883376	-0.2768253	0.023895	-0.0527131
0.059513	247826.23	5.0230562	45.940853	-2.1468838	-0.144986	0.0182399	-0.0235115
0.0595456	247961.8	5.028553	45.965983	-0.0084812	-0.0205341	0.0151624	0.0027939
0.0595826	248115.92	5.0348061	45.994554	2.1285901	0.1006946	0.0156193	0.0272515
0.0595768	248091.62	5.03382	45.99005	4.174591	0.2120685	0.0193513	0.0485315
0.0595688	248058.58	5.0324791	45.983924	6.3062164	0.320112	0.0257437	0.0671437
0.0595578	248012.57	5.0306124	45.975394	8.3475319	0.4201418	0.0381225	0.0833122
0.0594876	247720.28	5.0187619	45.921211	10.472638	0.5124024	0.0525048	0.0987192
0.0594555	247586.53	5.0133441	45.896418	11.534999	0.5592771	0.062699	0.1050568

Table 15: U=40 mph, h/b=0.05

Mach No.	Re No.	q_c	Uoo	alpha_c	C_L	C_D_c	Cm_cg_c_w
0.0609787	253929.79	5.2735224	47.072301	-5.3153772	-0.4488207	0.0369975	-0.0915299
0.0609763	253919.5	5.2730951	47.070394	-4.3341646	-0.3877781	0.0312391	-0.0705396
0.0609691	253889.49	5.2718486	47.064831	-3.2561235	-0.3053603	0.0265582	-0.0480898
0.0610154	254082.28	5.2798579	47.100569	-2.1791458	-0.2230961	0.0226368	-0.0279568
0.061025	254122.53	5.2815309	47.108031	-1.1021426	-0.1431914	0.0195427	-0.01068
0.0610619	254276.14	5.2879179	47.136506	-0.0272113	-0.0658818	0.0174281	0.0048505
0.0611316	254566.21	5.2999894	47.190278	1.0458775	0.0069669	0.016479	0.020009
0.0610926	254403.95	5.2932353	47.1602	2.1190142	0.0775104	0.0166352	0.0335249
0.0610806	254353.95	5.2911548	47.150931	3.1029269	0.1450903	0.018572	0.0453944
0.0610962	254419.02	5.2938623	47.162993	4.1727272	0.207556	0.0199655	0.0567333
0.0610837	254366.66	5.2916837	47.153287	5.240402	0.2672967	0.0220701	0.0669891
0.061113	254489.04	5.2967765	47.175972	6.3090425	0.3269543	0.0254208	0.0757002

Table 16: U=60 mph, h/b=0.93 (OGE)

Mach No.	Re No.	q_c	Uoo	alpha_c	C_L	C_D_c	Cm_cg_c_w
0.0852575	358235.04	10.421781	65.940489	-10.605667	-0.4132066	0.0428261	-0.0996435
0.085202	358001.77	10.408212	65.897551	-8.4841958	-0.3297467	0.0291728	-0.0828046
0.0851239	357673.58	10.389139	65.837142	-6.3616074	-0.2435828	0.0197456	-0.0633541
0.0851384	357734.72	10.392691	65.848396	-4.2379765	-0.1548948	0.0140115	-0.0424504
0.0851458	357765.65	10.394488	65.854088	-2.1130218	-0.0630019	0.0107352	-0.0211163
0.0851896	357949.73	10.405187	65.887973	0.0097684	0.0236504	0.0093042	0.0010019
0.085258	358237.39	10.421917	65.940921	2.1353034	0.1169484	0.010267	0.0220962
0.0853344	358558.31	10.440598	65.999993	4.1728534	0.2078615	0.0137409	0.0425923
0.0854645	359104.85	10.472452	66.100597	6.2976885	0.2994649	0.0197258	0.0609456
0.0855913	359637.47	10.50354	66.198635	8.3326231	0.384046	0.029481	0.0796603
0.0856216	359764.91	10.510985	66.222094	10.457118	0.4748258	0.0433697	0.0928019
0.0855669	359535.25	10.49757	66.179821	12.579934	0.5615398	0.0606825	0.104743
0.0855108	359299.22	10.483791	66.136374	14.697441	0.6354007	0.0889606	0.1131428

Table 17: U=60 mph, h/b=0.3

Mach No.	Re No.	q_c	Uoo	alpha_c	C_L	C_D_c	Cm_cg_c_w
0.0877577	368740.58	11.041998	67.874248	-10.54211	-0.4699647	0.0455794	-0.1071098
0.0876874	368445.04	11.024306	67.81985	-8.5028346	-0.3748735	0.0320429	-0.089926
0.087732	368632.61	11.035533	67.854375	-6.3780928	-0.2834958	0.0217329	-0.0678065
0.0877696	368790.23	11.044972	67.883388	-4.250271	-0.1846615	0.0153378	-0.0460377
0.0878039	368934.67	11.053625	67.909975	-2.1226488	-0.0863102	0.011746	-0.023086
0.0879446	369525.87	11.08908	68.018797	0.0038964	0.0094336	0.0099757	-0.0002204
0.0880399	369926.15	11.113117	68.092478	2.1315888	0.1079548	0.0108077	0.022326
0.0880007	369761.35	11.103218	68.062144	4.171416	0.2043815	0.0142071	0.0431751
0.0879413	369512.07	11.088251	68.016257	6.2978955	0.2999662	0.0201081	0.0616848
0.0877263	368608.57	11.034093	67.849949	8.4217	0.3890743	0.0299893	0.0803926
0.0875711	367956.23	10.995074	67.729874	10.46097	0.4841518	0.0440119	0.0931453
0.0874467	367433.64	10.963864	67.63368	12.583216	0.569486	0.0613121	0.1058006
0.0873421	366994.07	10.937647	67.552768	14.703368	0.6497508	0.0931221	0.1098324

Table 18: U=60 mph, h/b=0.15

Mach No.	Re No.	q_c	Uoo	alpha_c	C_L	C_D_c	Cm_cg_c_w
0.0884906	368469.49	11.106099	68.3185	-10.59127	-0.5889857	0.0570349	-0.1330465
0.0885338	368649.34	11.116944	68.351846	-8.5412159	-0.4677991	0.04022	-0.1080589
0.0885051	368529.94	11.109744	68.329708	-6.4070563	-0.3536202	0.028053	-0.0787916
0.0885015	368514.96	11.108841	68.32693	-4.2695105	-0.2312426	0.0201703	-0.0524321
0.0887352	369488.01	11.167583	68.507346	-2.1342276	-0.1143438	0.0158199	-0.0255409
0.08878	369674.65	11.178868	68.541951	-0.0015901	-0.0038498	0.013712	1.519E-05
0.0887	369341.63	11.158737	68.480205	2.1307355	0.1058891	0.0146504	0.0253483
0.0886763	369242.56	11.152751	68.461836	4.1743592	0.2115074	0.0183268	0.0473767
0.0886706	369218.91	11.151322	68.457451	6.3029526	0.3122099	0.0245395	0.0673765
0.088546	368700.07	11.120004	68.361252	8.4300233	0.409226	0.0347371	0.086292
0.088357	367913.24	11.072593	68.215365	10.472274	0.5115203	0.0501214	0.0995191
0.0883198	367758.21	11.063263	68.186621	12.59777	0.6047244	0.0708698	0.1128033
0.0882361	367409.75	11.042308	68.122012	13.658478	0.6475977	0.0876257	0.1159125

Table 19: U=60 mph, h/b=0.10

Mach No.	Re No.	q_c	Uoo	alpha_c	C_L	C_D_c	Cm_cg_c_w
0.088175	367181.57	11.026438	68.06638	-8.4981639	-0.5742028	0.047081	-0.1298002
0.088277	367606.07	11.051948	68.145071	-6.4407374	-0.4351662	0.0323526	-0.0929479
0.0882169	367355.87	11.036909	68.098691	-4.2934036	-0.2890906	0.022883	-0.0586268
0.0883197	367783.88	11.062642	68.178032	-2.1491421	-0.1504536	0.0174654	-0.0268722
0.088267	367564.4	11.049442	68.137346	-0.0093201	-0.0225651	0.0146522	0.0014927
0.0883325	367837.28	11.065855	68.187932	2.1289868	0.1016553	0.0152535	0.0287894
0.0883072	367731.78	11.059508	68.168375	4.1772545	0.2185173	0.0188592	0.0515737
0.0883282	367819.16	11.064765	68.184574	6.3089999	0.3268511	0.0259452	0.0721357
0.088305	367722.74	11.058964	68.166699	8.3530843	0.4335848	0.0367201	0.0904372
0.0881413	367041.15	11.018006	68.040349	10.483415	0.5384949	0.0531323	0.1034399
0.0882266	367396.42	11.039345	68.106207	11.546325	0.5866973	0.0631173	0.1100087

Table 20: U=60 mph, h/b=0.05

Mach No.	Re No.	q_c	Uoo	alpha_c	C_L	C_D_c	Cm_cg_c_w
0.0878673	365899.87	10.949593	67.828784	-5.3337948	-0.4934122	0.0362124	-0.1044673
0.0878775	365942.6	10.952151	67.836704	-4.3504798	-0.4272792	0.0306678	-0.0818598
0.0878791	365949.07	10.952538	67.837905	-3.2695584	-0.3378878	0.0261103	-0.0558508
0.0878294	365742.01	10.940147	67.79952	-2.1895989	-0.2484044	0.0222617	-0.0329504
0.0878995	366034	10.957623	67.853649	-1.1092203	-0.1603274	0.019224	-0.0134782
0.0879399	366202.55	10.967716	67.884893	-0.0320459	-0.077587	0.0171998	0.0044567
0.0878659	365894.19	10.949254	67.827731	0.9580701	0.0025909	0.0171179	0.0211217
0.0878946	366013.81	10.956414	67.849906	2.1195443	0.0787937	0.0166742	0.0359997
0.0879674	366316.75	10.974558	67.906063	3.1049536	0.1499971	0.0180378	0.0491244
0.0878429	365798.57	10.943532	67.810006	4.1769343	0.217742	0.0197591	0.0612537
0.0879027	366047.25	10.958416	67.856104	5.2454578	0.2795375	0.0221139	0.0720795
0.0878483	365820.72	10.944857	67.814112	6.3153132	0.3421365	0.0256089	0.0822973

Table 21: U=80 mph, h/b=0.93 (OGE)

Mach No.	Re No.	q_c	Uoo	alpha_c	C_L	C_D_c	Cm_cg_c_w
0.1135256	477012.22	18.47842	87.80386	-8.3950958	-0.3246622	0.0267817	-0.0793588
0.1134721	476787.35	18.461001	87.762467	-6.3616688	-0.2437315	0.0182695	-0.0620131
0.1134653	476758.78	18.45879	87.75721	-4.2379745	-0.15489	0.0128594	-0.0414245
0.1134468	476681.07	18.452772	87.742904	-2.1129214	-0.0627588	0.0095276	-0.020782
0.1134053	476506.37	18.439249	87.710747	0.010876	0.026332	0.0081677	0.0009023
0.1135782	477233.16	18.495541	87.844529	2.136655	0.1202209	0.0092027	0.022312
0.1138108	478210.32	18.57136	88.024395	4.1735547	0.2095595	0.0124688	0.042825
0.1138867	478529.34	18.596146	88.083117	6.298045	0.300328	0.0182342	0.0621571
0.1139898	478962.31	18.629812	88.162813	8.3344164	0.3883877	0.0271564	0.0801304

Table 22: U=80 mph, h/b=0.3

Mach No.	Re No.	q_c	Uoo	alpha_c	C_L	C_D_c	Cm_cg_c_w
0.1183958	497475.63	20.097842	91.570569	-7.3499575	-0.3219064	0.0239747	-0.0748529
0.1183793	497406.4	20.092249	91.557827	-6.3769536	-0.2807378	0.0198621	-0.0660732
0.1184245	497596.41	20.107602	91.592801	-4.2500249	-0.1840655	0.0139694	-0.044481
0.1184581	497737.25	20.118987	91.618726	-2.1221812	-0.085178	0.0104484	-0.0227457
0.1185552	498145.57	20.152009	91.693886	0.0044069	0.0106696	0.0088905	-0.000241
0.1187092	498792.29	20.204368	91.812928	2.1326515	0.1105278	0.0096963	0.0220911
0.1186915	498718.18	20.198365	91.799287	4.172043	0.2058994	0.0127929	0.0432002
0.1185856	498273.35	20.162349	91.717406	6.2974945	0.2989952	0.0185571	0.0624637
0.1184239	497593.63	20.107377	91.592289	7.3599201	0.3460269	0.0224835	0.0711328

Table 23: U=80 mph, h/b=0.15

Mach No.	Re No.	q_c	Uoo	alpha_c	C_L	C_D_c	Cm_cg_c_w
0.1190355	495656.66	20.096498	91.900471	-5.3428349	-0.3046617	0.022464	-0.0643911
0.119049	495712.76	20.101048	91.910873	-4.2748952	-0.2442797	0.019379	-0.050728
0.119084	495858.75	20.112889	91.937941	-2.1404591	-0.129431	0.014987	-0.0243636
0.1190707	495803.23	20.108385	91.927646	-0.0073857	-0.0178816	0.0127662	0.001695
0.1192273	496455.46	20.161325	92.048578	2.1260379	0.0945154	0.0133935	0.0274501
0.1191347	496069.83	20.130016	91.977078	4.1711718	0.2037902	0.0167178	0.0500295
0.1191052	495946.85	20.120037	91.954275	5.2356858	0.2558782	0.0192129	0.0605048
0.1190077	495540.93	20.087114	91.879012	6.3016549	0.3090681	0.0225594	0.0702218

Table 24: U=80 mph, h/b=0.10

Mach No.	Re No.	q_c	Uoo	alpha_c	C_L	C_D_c	Cm_cg_c_w
0.1186701	494169.94	19.97221	91.606882	-4.2980018	-0.3002234	0.0219597	-0.057995
0.118652	494094.62	19.966122	91.592918	-2.1537123	-0.1615185	0.0168119	-0.0260842
0.118693	494265.31	19.97992	91.624561	-0.0127737	-0.0309268	0.014089	0.0031676
0.1187284	494412.71	19.991838	91.651885	2.1270981	0.0970823	0.0145929	0.0310872
0.1187141	494353.17	19.987024	91.640849	4.1761079	0.2157412	0.0177931	0.0548928
0.1186485	494079.98	19.964939	91.590205	6.3100319	0.3293498	0.0239302	0.0751337

Table 25: U=80, h/b=0.05

Mach No.	Re No.	q_c	Uoo	alpha_c	C_L	C_D_c	Cm_cg_c_w
0.118176	492112.49	19.80625	91.225482	-3.2746529	-0.3502222	0.0242969	-0.0602632
0.1181629	492058.21	19.801881	91.21542	-2.1928686	-0.2563207	0.0206904	-0.0359462
0.1182146	492273.28	19.819195	91.255287	-1.1110859	-0.1648444	0.0179007	-0.0153658
0.1182087	492248.88	19.81723	91.250765	-0.0326367	-0.0790174	0.016058	0.004117
0.1182273	492326.28	19.823463	91.265113	0.9594491	0.0059297	0.0156724	0.0216222
0.1182607	492465.32	19.834662	91.290888	2.1218648	0.084412	0.0155605	0.0370434
0.1180905	491756.66	19.777618	91.159519	3.1075059	0.1561767	0.0166432	0.0508475
0.1180784	491706.26	19.773565	91.150177	4.1795792	0.2241456	0.0182679	0.0628508
0.1181152	491859.36	19.785879	91.178557	5.2487791	0.2875787	0.0206057	0.0738153

Table 26: U=100 mph, h/b=0.93 (OGE)

Mach No.	Re No.	q_c	Uoo	alpha_c	C_L	C_D_c	Cm_cg_c_w
0.141231305	593425.9012	28.59820711	109.2321803	-5.21124914	-0.19671408	0.014447095	-0.0510674
0.141167017	593155.7752	28.57217736	109.182458	-4.23836948	-0.15584636	0.012224947	-0.04180464
0.141115703	592940.1639	28.55140925	109.1427704	-2.11223095	-0.0610872	0.00899534	-0.02115824
0.141209104	593332.6167	28.58921674	109.2150093	0.01182641	0.02863318	0.007706787	0.000727298
0.141353997	593941.4288	28.647917	109.3270737	2.138266302	0.124121969	0.008755936	0.023149852
0.14156359	594822.0991	28.73293573	109.4891791	4.177115971	0.218181756	0.011889424	0.04412849
0.141598418	594968.4366	28.74707516	109.5161155	4.265491509	0.2215121	0.012046845	0.044865116

Table 27: U=100 mph, h/b=0.3

Mach No.	Re No.	q_c	Uoo	alpha_c	C_L	C_D_c	Cm_cg_c_w
0.147571682	620066.9059	31.22359583	114.1360023	-4.25380002	-0.19320559	0.013880798	-0.04678565
0.147651361	620401.7038	31.25732257	114.1976287	-2.12311445	-0.08743748	0.010419231	-0.02437402
0.147788464	620977.7822	31.31539794	114.3036677	0.005412058	0.013103251	0.008949285	-0.00065881
0.147757897	620849.3466	31.30244547	114.2800265	2.13591104	0.118419593	0.009844068	0.023892663
0.147885749	621386.5533	31.35663949	114.3789104	3.200124827	0.169780757	0.011164261	0.035251169
0.147783907	620958.6355	31.31346686	114.3001434	4.178249131	0.220925273	0.012940881	0.046110574

Table 28: U=100 mph, h/b=0.15

Mach No.	Re No.	q_c	Uoo	alpha_c	C_L	C_D_c	Cm_cg_c_w
0.146818981	611345.3488	30.57255403	113.3504901	-3.21084875	-0.19574467	0.016916351	-0.03966358
0.146860937	611520.0503	30.5900297	113.3828817	-2.14228444	-0.13385038	0.015018615	-0.02626131
0.146899832	611682.006	30.60623485	113.4129102	-1.07392477	-0.07487263	0.013648389	-0.01234084
0.146830287	611392.423	30.57726245	113.3592182	-0.00650675	-0.01575363	0.012884893	0.001473495
0.146826409	611376.2784	30.57564761	113.3562248	1.061904483	0.045770059	0.012786065	0.016172127
0.146911178	611729.2502	30.61096287	113.4216698	2.130658903	0.105703527	0.01348142	0.029515747
0.146831176	611396.1278	30.57763302	113.3599051	3.110482643	0.163383707	0.014768572	0.041690309

Table 29: U=100 mph, h/b=0.10

Mach No.	Re No.	q_c	Uoo	alpha_c	C_L	C_D_c	Cm_cg_c_w
0.146520132	610144.1688	30.44657276	113.1056347	-3.1414843	-0.23844251	0.018372928	-0.04301614
0.146433566	609783.688	30.41060696	113.0388105	-2.15700624	-0.16949364	0.016523885	-0.02856014
0.146529868	610184.7122	30.45061918	113.1131505	-1.08419422	-0.09973624	0.014905483	-0.01274157
0.146457637	609883.9247	30.42060561	113.0573919	-0.01253696	-0.03035352	0.013946574	0.003036746
0.146454673	609871.5834	30.41937448	113.0551041	0.973661318	0.040339083	0.013925471	0.019069941
0.146520782	610146.8733	30.44684267	113.1061361	2.131578385	0.107929705	0.01444742	0.033408456
0.146405417	609666.4681	30.3989163	113.0170808	3.113643483	0.171036488	0.015559293	0.046464367

Table 30: U=100 mph, h/b=0.05

Mach No.	Re No.	q_c	Uoo	alpha_c	C_L	C_D_c	Cm_cg_c_w
0.145747349	606926.117	30.12625415	112.5090875	-1.11609281	-0.17696661	0.017819193	-0.01799912
0.145673662	606619.269	30.09579956	112.4522055	-0.03404163	-0.08241894	0.016082691	0.003630719
0.145695435	606709.9367	30.1047967	112.4690131	0.961528214	0.010963359	0.015509789	0.02350601
0.145713014	606783.1381	30.11206161	112.4825828	1.047710958	0.011405805	0.01532111	0.023549131
0.145701497	606735.1795	30.10730184	112.4736925	2.126305179	0.095162632	0.01546496	0.040480999
0.14560401	606329.222	30.06702662	112.398438	3.11445585	0.173003327	0.016334041	0.05478849

Appendix F: MATLAB© Data Reduction Program

```
%*********************************************************************
%*********************************************************************
%**********      Lt. Gebbie & Capt Anthony DeLuca    ***************************
%******   Adapted for the Balance AFIT 1 by Lt. Rivera Parga **********************
%*********    re-adapted by Troy Leveron, ENS, USNR   ***************************
%****** re-adapted by Brett Jones, ENS, USNR for UCAV Ground Effects Test**********
%***************Calculation of Lift, Drag, Moments    **************************
%*********************************************************************
%*********************************************************************
%*********************************************************************


%This Code will transfer measured Forces and Moments on the AFIT-1 balance to Wind
%(earth) centered frame of reference by correcting for tare effects, balance
%interactions, and wind tunnel irregularities, then gives a file with all the
%corrected data

clear;
clc;
close all;
format long
%##################################################################
%                    INPUT DECK
%FIRST FILL THE FOLLOWING INFORMATION

Masskg=1.235;                              % Mass of the UCAV in KGS (~3lbs for now until I weigh it)
T_room = mean([73.4 74 74.7]) + 459.67      %deg R  ****Changed for each day of testing****
P_barro = mean([28.6823 28.6130 28.6228]) * 0.4911541   %Psi   ****Changed for each day of
testing****

% INPUT DATA FILE AND INPUT DATA TARE FILE
load tarefile.txt;                 %tarefile GP42005tearA-10to+20B0model
TareFile = tarefile(:,1:9);
load datafile.txt;                 %datafile (Raw Data file name here)
DataFile = datafile(:,1:9);

%Offset distances from the Mounting Block to the Model C.G. (inches)
Y_cmb =  0;
X_cmb = 1.3725;                     %inches  (from origin @ balance center w/ + right)
Z_cmb = 0;


% Required for the Solid body blockage corrections due to wing
% and fuselage
Body_Volume = 63.39038 / 12^3 ;     %ft^3: From Solid Works "Mass Properties"
Wing_Area = 87.3958 / 12^2          %ft^2


%##################################################################
%I.-  Room Conditions and Model Specifics :
%     UNITS are in Ft, Sec, lbm, Psf, Rankine, fps
%##################################################################
```

```matlab
Mass = (Masskg * 1000) * 0.0022046;          %lbm (UCAV)
Gas_Const = 1716;                            %ft-lbf/Slug-R
Density = (P_barro * 144)/(1716 * T_room);   %lbm/ft^3 or lbf-s^2/ft^4
Root_Chord = 7.42/12;                        %ft
Span = 16 / 12;                              %ft
Aspect_Ratio = Span^2 / Wing_Area;
Kinematic_Viscosity = .372e-6;               %slug/ft-s
Speed_of_Sound = sqrt(1.4 * T_room * Gas_Const);   %fps


%###########################################################################
%II.-    Solid body blockage corrections due to wing and fuselage (Pope
%pg 369
%###########################################################################

K_1 = 1.04;                      % t/c=.15, 4 digit airfoil
delta = 0.3636;                  %boundary correction factor (b/B) (Ch. 10)
Tau_1 = 0.86;                    %factor from pg 369, fun. of tunnel shape and b/B
X_Section = (31/12)*(44/12);     %ft^2
Wing_Volume = Body_Volume;       %ft^3   Flying Wing UCAV
Epsilon_sb_w = (K_1*Tau_1*Wing_Volume) / X_Section^(3/2)
Epsilon_tunnel_correction = 1.090034;    %from Hot-wire data... ratio between hotwire and transducer vel
Epsilon_sb_gp = 1.076696;                %Plane # Vel / Open Tunnel Vel as measured by the hot-wire
Epsilon_tot = Epsilon_sb_w+ (Epsilon_sb_gp*Epsilon_tunnel_correction-1)


%###########################################################################
% III.-  Load the static tare data for the alpha sweep w/o the wind ,
%        separate each force from the file, and fit a 4th order poly
%        as an x-y plot (AoA vs.Force) for each of the 6 force sensors.
%###########################################################################

%load tare1.txt;                 %Raw tare data file to be read in.
FILE=TareFile(:,1:9);            %GP42005tearA-10to+20B0model

j=1;
k=1;
L=length(FILE);

for i=1:L                        %Run for all data points # of rows
   if i~=L                       %if current row is not last row, go to next
      NEXT=i+1;                  %set next equal to the value of the next row
      VALUE2=FILE(NEXT,1);       %set value2 as next row column 1
   else if i==L                  %unless the it is the last value
      VALUE2=50;                 %value2 set to 50 to end the sequence
   end
   end
   A(j,:)=FILE(i,:);             %set row j of A equal to row i of FILE
   VALUE1=FILE(i,1);             %set value1 equal to row i column 1 of FILE
   if VALUE1==VALUE2             %if value1 equals value2, go to next row
      j=j+1;
   else if VALUE1~=VALUE2        %if value1 and value2 are different check
      if length(A(:,1))<5        %if less than 20 values, ignored due to angle change
         j=1;
         clear A;
      else if length(A(:,1))>5   %if more than 20 values
```

98

```matlab
            C=length(A(:,1));            %find length of A
            for m=1:9                    %Average all rows of the like values in A
                B(k,m)=mean(A(4:C,m));   %disregarding first 10 for vibrations
            end
            j=1;
            k=k+1;
            clear A
        end
        end

    end
    end
end

if B(k-1,1)<B((k-2),1)
    B=B(1:(k-2),:)
end

tare=[B];

%_____End of inserted code
[row,col] = size(tare);


for k = 1:row;

theta_tare(k,:,:)  = tare(k,1).* (pi/180);
NF_tare(k,:,:)     = tare(k,4);
PM_tare(k,:,:)     = tare(k,5);
SF_tare(k,:,:)     = tare(k,7);
YM_tare(k,:,:)     = tare(k,8);
AF_tare(k,:,:)     = tare(k,6);
RM_tare(k,:,:)     = tare(k,9);

end

NF_poly = polyfit(theta_tare,NF_tare,4);
PM_poly = polyfit(theta_tare,PM_tare,4);
SF_poly = polyfit(theta_tare,SF_tare,4);
YM_poly = polyfit(theta_tare,YM_tare,4);
AF_poly  = polyfit(theta_tare,AF_tare,4);
RM_poly  = polyfit(theta_tare,RM_tare,4);

%#############################################################################
%IV.- Load the specific test run files,
%#############################################################################

clear ('AA','B','C','L')

%load data1.txt;              %Raw data file to be read in:
FILE=DataFile(:,:);          %Same as above

j=1;
k=1;
```

```matlab
L=length(FILE);

for i=1:L                          %Run for all data points # of rows
  if i~=L                          %if current row is not last row, go to next
     NEXT=i+1;                     %set next equal to the value of the next row
     VALUE2=FILE(NEXT,1);          %set value2 as next row column 1
  else if i==L                     %unless the it is the last value
     VALUE2=50;                    %value2 set to 50 to end the sequence
  end
  end
  A(j,:)=FILE(i,:);                %set row j of A equal to row i of FILE
  VALUE1=FILE(i,1);                %set value1 equal to row i column 1 of FILE
  if VALUE1==VALUE2                %if value1 equals value2, go to next row
     j=j+1;
  else if VALUE1~=VALUE2           %if value1 and value2 are different check
     if length(A(:,1))<5           %if less than 20 values, ignored due to angle change
        j=1;
        clear A;
     else if length(A(:,1))>5               %if more than 20 values
           C=length(A(:,1));                %find length of A
           for m=1:9                        %Average all rows of the like values in A
             B(k,m)=mean(A(4:C,m));         %disregarding first 10 for vibrations
           end
           j=1;
           k=k+1;
           clear A
        end
     end
  end
  end
end

if B(k-1,1)<B((k-2),1)
   B=B(1:(k-2),:)
end

sample_data=[B];

%_____End of inserted code
[row2,col2] = size(sample_data);


for i = 1:row2;

%Angles of the model during test runs (Roll, Pitch {AoA}, Yaw {Beta}):

phi            = 0;
theta(i,:)     = sample_data(i,1) .* (pi/180);           %radians
si(i,:)        = sample_data(i,2) .* (pi/180);           %radians
Wind_Speed(i,:) = sample_data(i,3) .* (5280/3600);  %fps

%Flight Parameters (Re#, Ma#, Dynamic Pressure):

q = (.5 * Density) .* Wind_Speed.^2;                     %lbf/ft^2
```

```matlab
q_Corrected = q .* (1 + Epsilon_tot)^2;                              %lbf/ft^2
Wind_Speed_Corrected = Wind_Speed .* (1 + Epsilon_tot);             %fps
Wind_Speed_Corrected_mph = Wind_Speed_Corrected.*(3600/5280);
Mach_Number = Wind_Speed_Corrected ./ Speed_of_Sound;               %NonDimensional
Reynolds_Number = ((Density * Root_Chord) .* Wind_Speed_Corrected) ./ Kinematic_Viscosity;
%NonDimensional
Flight_Parameters = [Mach_Number Reynolds_Number q_Corrected];


%individual forces and moments for each sensor:

%NEW NOTATION
NF_test(i,:,:)    = sample_data(i,4);
PM_test(i,:,:)    = sample_data(i,5);
SF_test(i,:,:)    = sample_data(i,7);
YM_test(i,:,:)    = sample_data(i,8);
AF_test(i,:,:)    = sample_data(i,6);
RM_test(i,:,:)    = sample_data(i,9);


%#############################################################################
%V.-   Subtract the effect of the static
%      weight with the tare polynominals above
%#############################################################################

%Evaluating the actual test theta angle (AoA) in the tare polynominal to
%determine the tare values for the angles tested in each run.

NF_eval = polyval(NF_poly,theta);
PM_eval = polyval(PM_poly,theta);
SF_eval = polyval(SF_poly,theta);
YM_eval = polyval(YM_poly,theta);
AF_eval  = polyval(AF_poly,theta);
RM_eval  = polyval(RM_poly,theta);

%The Time-Averaged (raw) forces and momentums NF,AF,SF,PM,YM AND RM measurd in the wind
%tunnel (body axis) with the tare effect of the weight subtracted off.

NF_resolved = NF_test - (NF_eval);
PM_resolved = PM_test - (PM_eval);
SF_resolved = SF_test - (SF_eval);
YM_resolved = YM_test - (YM_eval);
AF_resolved  = AF_test -  (AF_eval);
RM_resolved  = RM_test -  (RM_eval);

Forces_minus_tare = [NF_resolved, AF_resolved, PM_resolved, RM_resolved, YM_resolved,
SF_resolved]';

%#############################################################################
%VI.- CORRECT FORCES AND MOMENTS FOR BALANCE INTERATIONS (body axis)
%#############################################################################

%USING THE REDUCTION EQUATIONS
%LET US SET A MAXIMUN NUMBER OF INTERATIONS (FOR AVOIDING AN INFINIT LOOP)
MAXIT=100;
```

```
%SET THE LIMIT FOR THE DIFFERENCE BETWEEN INTERATIONS(CRITERIA FOR FINISH
%THE INTERATIONS)
LIMIT= 10E-14;

%MATCHING EACH NAME WITH  THE DATA
% Prof. Reeder added :i
MNF=NF_resolved(i);
MAF=AF_resolved(i);
MPM=PM_resolved(i);
MRM=RM_resolved(i);
MYM=YM_resolved(i);
MSF=SF_resolved(i);

%INPUT OF THE CONSTANTS VALUES FROM THE MATRIX FOR SENSITIVITIES AND
%INTERATIONS
K=[0  -1.3567E-03  -3.8021E-03  -4.2814E-03  -1.6966E-03   1.7567E-03 ...
   5.3167E-05  -1.3867E-04  -5.5629E-05  3.5181E-05  1.0601E-05  -2.5271E-04...
   5.6693E-05  -1.9537E-04   1.7908E-05  -3.6606E-05  -4.9934E-05  4.1205E-05...
   2.5648E-05  -1.9289E-05  8.9661E-05  -1.9594E-05  -4.9859E-04  -1.1599E-03...
   5.7163E-05  8.9798E-05  -7.8591E-05  9.3187E-03  0  -3.8421E-03  3.5740E-03...
   9.7714E-05  -2.7776E-03  -1.3552E-04  5.1538E-04  2.2082E-04  -1.2706E-05...
  -2.3637E-05  1.3686E-05  1.1085E-04  -3.6557E-06  4.9876E-06  8.1085E-06...
   3.7381E-05  1.2791E-04  -9.4527E-06  -2.3083E-06  -1.2046E-06  7.8161E-04...
  -1.1997E-03  -3.0560E-05  -6.6202E-05  3.7227E-04  -2.1469E-04  4.8386E-03...
  -3.7387E-03  0  -1.8479E-02  3.9077E-03  9.9165E-04  -1.4825E-05  -1.4830E-06...
   6.0845E-05  8.0667E-05  1.8547E-05  -5.0212E-05  1.0539E-04  -2.2676E-04...
   4.3793E-05  -1.0456E-05  -8.1186E-06  -2.1653E-05  -3.3070E-05  1.7280E-05...
  -7.4509E-05  -3.4399E-05  -8.2999E-04  -6.7962E-04  4.0521E-05  -5.1604E-05...
   9.1132E-06  -5.7360E-03  -2.2213E-04  9.9131E-04  0  -9.5790E-03  6.7114E-03...
   3.6824E-05  1.0056E-04  -3.7105E-05  -9.0295E-05  -7.4580E-05  1.4814E-04...
   7.2634E-05  -8.4778E-06  6.3486E-05  5.6328E-05  -1.3617E-04  2.2196E-05...
   1.3606E-05  -3.6689E-05  8.3283E-05  1.1865E-04  1.8544E-05  -1.9831E-05...
   1.7894E-05  -6.8164E-05  -7.0892E-05  1.2378E-03  1.6961E-03  -6.5102E-03...
  -9.3202E-03  0  5.1349E-03  1.3612E-05  -1.3175E-04  7.2442E-06  5.6705E-04...
  -1.4723E-05  -4.8656E-05  -1.4282E-04  5.9711E-05  5.9046E-05  -3.6490E-04...
   7.4881E-05  5.4601E-06  1.0129E-03  -1.3867E-04  8.1617E-05  6.6053E-05...
  -1.3417E-05  9.0025E-05  -4.5362E-05  -4.4672E-06  9.5087E-05  -3.4077E-02...
   7.9142E-04  1.6667E-03  -6.6512E-03  8.1538E-03 0  -1.4185E-05  7.3209E-05...
  -2.5849E-05  1.2325E-03  -4.1696E-05  4.6266E-05  8.6146E-05  2.1436E-05...
   5.0874E-05  -3.2738E-04  2.2218E-04  8.6478E-06  7.3395E-04  -4.1453E-05...
   3.5719E-05  2.5313E-05  1.5182E-04  3.6007E-05  -2.8844E-05  8.9741E-05...
  -7.3257E-05];

%COMPUTE THE UNCORRECTED FORCES AND MOMENTS BY
%CONSIDERING THAT THE PRIME SENSITIVITY CONSTANTS ARE ALREADY APLIED:

NF1=MNF;
AF1=MAF;
PM1=MPM;
RM1=MRM;
YM1=MYM;
SF1=MSF;

%FOR THE FIRST INTERACTION LET US INIZIALICE THE VALUES OF FORCES AND
```

%MOMENTS WITH THE VALUES OF THE UNCORRECTED FORCES AND MOMENTS

NF(1)=NF1;
AF(1)=AF1;
PM(1)=PM1;
RM(1)=RM1;
YM(1)=YM1;
SF(1)=SF1;

%DOING THE INTERACTION EQUATIONS:

for n=2:MAXIT;

NF(n)=NF1-((K(2)*AF(n-1))+(K(3)*PM(n-1))+(K(4)*RM(n-1))+(K(5)*YM(n-1))+(K(6)*SF(n-1))+(K(7)*NF(n-1)^2)+...
    (K(8)*(NF(n-1)*AF(n-1)))+(K(9)*(NF(n-1)*PM(n-1)))+(K(10)*(NF(n-1)*RM(n-1)))+(K(11)*(NF(n-1)*YM(n-1)))+...
    (K(12)*(NF(n-1)*SF(n-1)))+(K(13)*(AF(n-1)^2))+(K(14)*(AF(n-1)*PM(n-1)))+(K(15)*(AF(n-1)*RM(n-1)))+...
    (K(16)*(AF(n-1)*YM(n-1)))+(K(17)*(AF(n-1)*SF(n-1)))+(K(18)*(PM(n-1)^2))+(K(19)*(PM(n-1)*RM(n-1)))+...
    (K(20)*(PM(n-1)*YM(n-1)))+(K(21)*(PM(n-1)*SF(n-1)))+(K(22)*(RM(n-1)^2))+(K(23)*(RM(n-1)*YM(n-1)))+...
    (K(24)*(RM(n-1)*SF(n-1)))+(K(25)*(YM(n-1)^2))+(K(26)*(YM(n-1)*SF(n-1)))+(K(27)*(SF(n-1)^2)));

AF(n)=AF1-((K(28)*NF(n-1))+(K(30)*PM(n-1))+(K(31)*RM(n-1))+(K(32)*YM(n-1))+(K(33)*SF(n-1))+(K(34)*NF(n-1)^2)+...
    (K(35)*(NF(n-1)*AF(n-1)))+(K(36)*(NF(n-1)*PM(n-1)))+(K(37)*(NF(n-1)*RM(n-1)))+(K(38)*(NF(n-1)*YM(n-1)))+...
    (K(39)*(NF(n-1)*SF(n-1)))+(K(40)*(AF(n-1)^2))+(K(41)*(AF(n-1)*PM(n-1)))+(K(42)*(AF(n-1)*RM(n-1)))+...
    (K(43)*(AF(n-1)*YM(n-1)))+(K(44)*(AF(n-1)*SF(n-1)))+(K(45)*(PM(n-1)^2))+(K(46)*(PM(n-1)*RM(n-1)))+...
    (K(47)*(PM(n-1)*YM(n-1)))+(K(48)*(PM(n-1)*SF(n-1)))+(K(49)*(RM(n-1)^2))+(K(50)*(RM(n-1)*YM(n-1)))+...
    (K(51)*(RM(n-1)*SF(n-1)))+(K(52)*(YM(n-1)^2))+(K(53)*(YM(n-1)*SF(n-1)))+(K(54)*(SF(n-1)^2)));

PM(n)=PM1-((K(55)*NF(n-1))+(K(56)*AF(n-1))+(K(58)*RM(n-1))+(K(59)*YM(n-1))+(K(60)*SF(n-1))+(K(61)*NF(n-1)^2)+...
    (K(62)*(NF(n-1)*AF(n-1)))+(K(63)*(NF(n-1)*PM(n-1)))+(K(64)*(NF(n-1)*RM(n-1)))+(K(65)*(NF(n-1)*YM(n-1)))+...
    (K(66)*(NF(n-1)*SF(n-1)))+(K(67)*(AF(n-1)^2))+(K(68)*(AF(n-1)*PM(n-1)))+(K(69)*(AF(n-1)*RM(n-1)))+...
    (K(70)*(AF(n-1)*YM(n-1)))+(K(71)*(AF(n-1)*SF(n-1)))+(K(72)*(PM(n-1)^2))+(K(73)*(PM(n-1)*RM(n-1)))+...
    (K(74)*(PM(n-1)*YM(n-1)))+(K(75)*(PM(n-1)*SF(n-1)))+(K(76)*(RM(n-1)^2))+(K(77)*(RM(n-1)*YM(n-1)))+...
    (K(78)*(RM(n-1)*SF(n-1)))+(K(79)*(YM(n-1)^2))+(K(80)*(YM(n-1)*SF(n-1)))+(K(81)*(SF(n-1)^2)));

RM(n)=RM1-((K(82)*NF(n-1))+(K(83)*AF(n-1))+(K(84)*PM(n-1))+(K(86)*YM(n-1))+(K(87)*SF(n-1))+(K(88)*NF(n-1)^2)+...

    (K(89)*(NF(n-1)*AF(n-1)))+(K(90)*(NF(n-1)*PM(n-1)))+(K(91)*(NF(n-1)*RM(n-1)))+(K(92)*(NF(n-1)*YM(n-1)))+...

    (K(93)*(NF(n-1)*SF(n-1)))+(K(94)*(AF(n-1)^2))+(K(95)*(AF(n-1)*PM(n-1)))+(K(96)*(AF(n-1)*RM(n-1)))+...

    (K(97)*(AF(n-1)*YM(n-1)))+(K(98)*(AF(n-1)*SF(n-1)))+(K(99)*(PM(n-1)^2))+(K(100)*(PM(n-1)*RM(n-1)))+...

    (K(101)*(PM(n-1)*YM(n-1)))+(K(102)*(PM(n-1)*SF(n-1)))+(K(103)*(RM(n-1)^2))+(K(104)*(RM(n-1)*YM(n-1)))+...

    (K(105)*(RM(n-1)*SF(n-1)))+(K(106)*(YM(n-1)^2))+(K(107)*(YM(n-1)*SF(n-1)))+(K(108)*(SF(n-1)^2)));

YM(n)=YM1-((K(109)*NF(n-1))+(K(110)*AF(n-1))+(K(111)*PM(n-1))+(K(112)*RM(n-1))+(K(114)*SF(n-1))+(K(115)*NF(n-1)^2)+...

    (K(116)*(NF(n-1)*AF(n-1)))+(K(117)*(NF(n-1)*PM(n-1)))+(K(118)*(NF(n-1)*RM(n-1)))+(K(119)*(NF(n-1)*YM(n-1)))+...

    (K(120)*(NF(n-1)*SF(n-1)))+(K(121)*(AF(n-1)^2))+(K(122)*(AF(n-1)*PM(n-1)))+(K(123)*(AF(n-1)*RM(n-1)))+...

    (K(124)*(AF(n-1)*YM(n-1)))+(K(125)*(AF(n-1)*SF(n-1)))+(K(126)*(PM(n-1)^2))+(K(127)*(PM(n-1)*RM(n-1)))+...

    (K(128)*(PM(n-1)*YM(n-1)))+(K(129)*(PM(n-1)*SF(n-1)))+(K(130)*(RM(n-1)^2))+(K(131)*(RM(n-1)*YM(n-1)))+...

    (K(132)*(RM(n-1)*SF(n-1)))+(K(133)*(YM(n-1)^2))+(K(134)*(YM(n-1)*SF(n-1)))+(K(135)*(SF(n-1)^2)));

SF(n)=SF1-((K(136)*NF(n-1))+(K(137)*AF(n-1))+(K(138)*PM(n-1))+(K(139)*RM(n-1))+(K(140)*YM(n-1))+(K(142)*NF(n-1)^2)+...

    (K(143)*(NF(n-1)*AF(n-1)))+(K(144)*(NF(n-1)*PM(n-1)))+(K(145)*(NF(n-1)*RM(n-1)))+(K(146)*(NF(n-1)*YM(n-1)))+...

    (K(147)*(NF(n-1)*SF(n-1)))+(K(148)*(AF(n-1)^2))+(K(149)*(AF(n-1)*PM(n-1)))+(K(150)*(AF(n-1)*RM(n-1)))+...

    (K(151)*(AF(n-1)*YM(n-1)))+(K(152)*(AF(n-1)*SF(n-1)))+(K(153)*(PM(n-1)^2))+(K(154)*(PM(n-1)*RM(n-1)))+...

    (K(155)*(PM(n-1)*YM(n-1)))+(K(156)*(PM(n-1)*SF(n-1)))+(K(157)*(RM(n-1)^2))+(K(158)*(RM(n-1)*YM(n-1)))+...

    (K(159)*(RM(n-1)*SF(n-1)))+(K(160)*(YM(n-1)^2))+(K(161)*(YM(n-1)*SF(n-1)))+(K(162)*(SF(n-1)^2)));

% SET THE LIMIT FOR THE DIFFERENCE BETWEEN INTERATIONS(CRITERIA FOR FINISH THE INTERATIONS)

DIFFNF(n)=abs(NF(n)-NF(n-1));
DIFFAF(n)=abs(AF(n)-AF(n-1));
DIFFPM(n)=abs(PM(n)-PM(n-1));
DIFFRM(n)=abs(RM(n)-RM(n-1));
DIFFYM(n)=abs(YM(n)-YM(n-1));
DIFFSF(n)=abs(SF(n)-SF(n-1));

if DIFFNF(n)&DIFFAF(n)&DIFFPM(n)&DIFFRM(n)&DIFFYM(n)&DIFFSF(n) < LIMIT
 break

```matlab
end

end

Corrected_Data(:,i)= [NF(n);AF(n);PM(n);RM(n);YM(n);SF(n)];

%#########################################################################
%VII.- Calculation of the Axial, Side, & Normal Forces from the corrected balance
%      forces in the Body Axis reference frame
%#########################################################################

Forces_b(:,i) = [Corrected_Data(2,i); Corrected_Data(6,i); Corrected_Data(1,i)];

%Calculation of the Drag, Side, & Lift Forces in the Wind Axis reference
%frame

Forces_w = [Forces_b(1,:).*cos(theta').*cos(si')+Forces_b(2,:).*sin(si')+Forces_b(3,:).*sin(theta').*cos(si');
        -Forces_b(1,:).*sin(si').*cos(theta')+Forces_b(2,:).*cos(si')-Forces_b(3,:).*sin(theta').*sin(si');
        -Forces_b(1,:).*sin(theta')+Forces_b(3,:).*cos(theta')];

%First entry is the moments calculated by the balance or direct calculation
%in the Body Reference Frame.  Balance measures Roll (l), Yaw is about the
%z-axis (n), and Pitch is about the y-axis (m).  Distances from strain
%gages to C.G. are in INCHES.  Moments are in-lbf

m = Corrected_Data(3,i);

n = Corrected_Data(5,i);

l = Corrected_Data(4,i);

Moments_b(:,i) = [l; m; n];

%Second entry is the conversion from the "Balance Centeric" moments to the
%Wind Reference monments with respect to the Balance Center (bc)

Moments_w_bc = [Moments_b(1,:).*cos(theta').*cos(si')-Moments_b(2,:).*sin(si') +Moments_b(3,:).
*sin(theta').*cos(si');

Moments_b(1,:).*sin(si').*cos(theta')+Moments_b(2,:).*cos(si')+Moments_b(3,:).*sin(theta').*sin(si');
        -Moments_b(1,:).*sin(theta')+Moments_b(3,:).*cos(theta')];

%Finally, the balance centered moments are converted to moments about the
%Model's Center of Mass (cm) or Center of Gravity (CG)

cgdist=sqrt((X_cmb)^2+(Z_cmb)^2);  %Obtaining the direct distance between the center of the balance and
%the center of mass
w=atan(-Z_cmb/X_cmb);              %Obtaining the angle between cgdist and the x axes at zero angle of
%attack

X_cm(i,:)= cos(theta(i,:)+w)*cos(si(i,:))*(cgdist);
Y_cm(i,:) = Y_cmb + X_cm(i,:)*tan(si(i,:));
Z_cm(i,:)= -sin(theta(i,:)+w)*(cgdist);
```

```matlab
Moments_w_cg_u = [Moments_w_bc(1,:) + Z_cm(i,:)*Forces_w(2,:) + Forces_w(3,:)* Y_cm(i,:);
         Moments_w_bc(2,:) - Forces_w(3,:)* X_cm(i,:) + Forces_w(1,:)* Z_cm(i,:);
         Moments_w_bc(3,:) - Forces_w(1,:)* Y_cm(i,:) - Forces_w(2,:)* X_cm(i,:)];

%###########################################################################

%VIII.- Calculation of the actual Lift and Drag nondimensional Coefficients, uncorrected for tunnel effects,
%(Cl and Cd)
%###########################################################################

C_D_u = Forces_w(1,:) ./ (q_Corrected' .* Wing_Area);
C_Y_u = Forces_w(2,:) ./ (q_Corrected' .* Wing_Area);
C_L_u = Forces_w(3,:) ./ (q_Corrected' .* Wing_Area);  %Keuthe & Chow pg 178
Coefficients = [C_L_u; C_D_u; C_Y_u]';
 Ave_Cl = mean(Coefficients(:,1));
 Ave_Cd = mean(Coefficients(:,2));

end

%###########################################################################
%IX       Drag Coefficient Correction
%###########################################################################

C_D_o = min(Coefficients(:,2));
C_L_u_sqrd = Coefficients(:,1).^2;
Delta_C_D_w = ((delta * Wing_Area) / X_Section) .* C_L_u_sqrd;
C_D_Corrected = C_D_u' + Delta_C_D_w;

%###########################################################################
%X.- Angle of Attack due to upwash Correction
%###########################################################################

alpha = sample_data(:,1);
Delta_alpha_w = ((delta * Wing_Area) / X_Section) .* (57.3 * C_L_u);
alpha_Corrected = alpha + Delta_alpha_w';

%###########################################################################
%XI.- Pitching Moment Correction
%###########################################################################

c_bar = (mean([7.42, 7.42, 7.42, 3.7442, 0])) / 12; %ft = Mean Chord of wing taken at five equal stations

Cl_w_cg =  Moments_w_cg_u(1,:) ./ (q_Corrected' .* (Wing_Area * Span*12));
Cm_w_cg_u = Moments_w_cg_u(2,:) ./ (q_Corrected' .* (Wing_Area * c_bar*12));
Cn_w_cg =  Moments_w_cg_u(3,:) ./ (q_Corrected' .* (Wing_Area * Span*12));

Cm_w_cg_corrected = Cm_w_cg_u;       %No Tail
Corrected_Moment_Coefficients = [Cl_w_cg' Cm_w_cg_corrected' Cn_w_cg'];

%OBTAINING THE MOMENTS COEFFICIENTS CORRECTED ABOUT THE CENTER OF THE
%BALANCE

Cl_w_bc =  Moments_w_bc(1,:) ./ (q_Corrected' .* (Wing_Area * Span*12));
Cm_w_bc_u = Moments_w_bc(2,:) ./ (q_Corrected' .* (Wing_Area * c_bar*12));
```

```
Cn_w_bc =   Moments_w_bc(3,:) ./ (q_Corrected' .* (Wing_Area * Span*12));

Cm_w_bc_corrected = Cm_w_bc_u;
Corrected_Moment_Coefficients_bc = [Cl_w_bc' Cm_w_bc_corrected' Cn_w_bc'];
```

```
alpha = sample_data(:,1);

fprintf('   Mach Number Reynolds Number Dynamic Pressure(Psf)\r')
Flight_Parameters
fprintf(' \r');
fprintf(' Loads are in lbf and arranged [D S L] across the top and increments of alpha down the side \r')
Forces_w'
fprintf(' \r')
fprintf(' Moments are in in-lbf and arranged [L M N] down the side and increments of alpha along the top
\r')
Moments_w_cg_u
fprintf(' \r')
fprintf('      Cl_u         Cd_u          CY_u \r');
Coefficients
fprintf(' \r')
fprintf('    Del_CD_w      CD_u     CD_Corrected \r');
Compare_CD = [Delta_C_D_w C_D_u' C_D_Corrected]
fprintf(' \r')
fprintf('    Del_alpha_w    alpha_g    alpha_Corrected \r');
Compare_alpha = [Delta_alpha_w' alpha alpha_Corrected ]
fprintf(' \r')
fprintf('    Cl_cg_wind   Cm_cg_corrected_w    Cn_cg_wind \r');
Corrected_Moment_Coefficients
fprintf(' \r')
fprintf('    M#        Re#        q_c        Uoo      alpha_c     C_L       C_D_c      Cl_cg_w
Cm_cg_c_w   Cn_cg_w      C_Y\r');
YY=[Flight_Parameters (Wind_Speed_Corrected .* (3600/5280)) alpha_Corrected C_L_u' C_D_Corrected
Corrected_Moment_Coefficients C_Y_u']%pressure]
```

```
wk1write('output.xls',YY,2,1)
```

Bibliography

1. Pendleton, Linda D. "Ground Effect." *AV Web.* Aviation Publishing Group, 2005. 2 April 2005 http://www.avweb.com/news/airman/185905-1.html.

2. van Opstal, Edwin and others. *The WIG Page*. 2 April 2005 http://www.se-technology.com/wig/index.php.

3. Cole, William. "The Pelican: A Big Bird for the Long Haul," *Boeing Frontiers Online*, 1 (5) (September 2002) n.pag. 7 April 2005 http://www.boeing.com/news/frontiers/archive/2002/september/i_pw.html.

4. Wyatt, Earl C. and Michael J. Hirschberg. "Transforming the Future Battlefield: The DARPA / Air Force Unmanned Combat Air Vehicle (UCAV) Program," *AIAA/ICAS International Air and Space Symposium and Exposition: The Next 100 Years*, AIAA 2003-2616: 1-8 (July 2003).

5. "Joint Unmanned Combat Air Systems." Excerpt from unpublished article. n.pag. 6 April 2005 http://www.darpa.mil/j-ucas/.

6. Curry, Robert E. *Dynamic Ground Effect for a Cranked Arrow Wing Airplane*. NASA TM 4799, 1997.

7. Tirpak, John A. "The Robotic Air Force," *Journal of the Air Force Association,* 80 (9) (September 1997) n.pag. 4 April 2005 http://www.afa.org/magazine/sept1997/0997robot.asp.

8. Reed, Shad A. *Subsonic Aerodynamic Stability and Control Assessment of Advanced Aerial Vehicle Configurations*. MS thesis, School of Graduate Studies, Wright State University, Dayton, OH, March 1998.

9. Wieselsberger, C. *Wing Resistance Near the Ground.* NACA TM 77, 1922.

10. Fink, Marvin P. and James L. Lastinger. *Aerodynamic Characteristics of Low-Aspect-Ratio Wings in Close Proximity to the Ground.* NASA TN D-926, 1961.

11. Le Sueur, Maurice. *Ground Effect on the Take-off and Landing of Airplanes.* NACA TM 771, 1934.

12. Recant, Isidore G. *Wind-tunnel Investigation of Ground Effect on Wings with Flaps.* NACA TN 705, 1939.

13. McCormick, Barnes W. *Aerodynamics, Aeronautics, and Flight Mechanics.* New York: John Wiley and Sons, Inc, 1995.

14.   Raymond, Arthur E. *Ground Influence on Aerofoils.* NACA TN 67, 1921.

15.   Schweikhard, William. "A Method for In-Flight Measurement of Ground Effect on Fixed-Wing Aircraft," *Journal of Aircraft,* 4 (2): 101-104 (March-April 1967).

16.   Chang, Ray Chung and Vincent U. Muirhead. "Effect of Sink Rate on Ground Effect of Low-Aspect-Ratio Wings," *Journal of Aircraft,* 24 (3): 176-180 (March 1986).

17.   Baker, Paul A., William G. Schweikhard, and William R. Young. *Flight Evaluation of Ground Effect on Several Low-Aspect-Ratio Airplanes.* NASA TN D-6053, 1970.

18.   Corda, Stephen and others. *Dynamic Ground Effects Flight Test of an F-15 Aircraft.* NASA TM 4604, 1994.

19.   McDonnell Douglas Corporation, *USAF Stability and Control DATCOM,* U.S. Air Force Flight Dynamics Laboratory, Wright-Patterson AFB, OH, Oct. 1960 (Revised Apr. 1976).

20.   Lee, Pai Hung, C. Edwards Lan, and Vincent U. Muirhead. *An Experimental Investigation of Dynamic Ground Effect.* NASA CR 4105, 1987.

21.   Curry, Robert E. and Lewis R. Owens. *Ground-Effect Characteristics of the Tu-144 Supersonic Transport Airplane.* NASA TM 2003-212035, 2003.

22.   Turner, Thomas R. "Endless-belt Technique for Ground Simulation," *Proceedings of Conference on VTOL/STOL Aircraft,* NASA SP 116, Paper 25: 445, (1966).

23.   Kemmerly, Guy T. and John W. Paulson, Jr. *Investigation of a Moving-Model Technique for Measuring Ground Effects.* NASA TM 4080, 1989.

24.   *Eden 333.* Technical Specifications. Stratasys Inc. © 2003. 3 May 2005 http://www.stratasys.com/NA/pdfs/PS_eden333.pdf.

25.   *FullCure™ 700 Series.* Technical Specifications. Stratasys Inc. © 2005. 25 March 2005 http://www.stratasys.com/NA/pdfs/Eden_FullCure700.pdf.

26.   DeLuca, Anthony M. *Experimental Investigation into the Aerodynamic Performance of Both Rigid and Flexible Wing Structured Micro-Air-Vehicles.* MS thesis, AFIT/GAE/ENY/04-M06, Department of Aeronautics and Astronautics, Air Force Institute of Technology (AU), Wright-Patterson AFB, OH, March 2004.

27.   Barlow, Jewel B. and others. *Low-Speed Wind Tunnel Testing* (3rd Edition)*.* New York: John Wiley and Sons, 1999.

28. Gebbie, David A. *Experimental Study of the Subsonic Aerodynamics of a Blended Wing Body Air Vehicle with a Focus on Rapid Technology Assessment.* MS thesis, AFIT/GAE/ENY/05-M09, Department of Aeronautics and Astronautics, Air Force Institute of Technology (AU), Wright-Patterson AFB, OH, March 2005.

29. Rivera Parga, Jose R. *Wind Tunnel Investigation of the Static Stability and Control Effectiveness of a Rotary Tail in a Portable UAV.* MS thesis, AFIT/GAE/ENY/04-D02, Department of Aeronautics and Astronautics, Air Force Institute of Technology (AU), Wright-Patterson AFB, OH, December 2004.

30. Bertin, John J. *Aerodynamics for Engineers* (4th Edition). New Jersey: Prentice-Hall, 2002.

31. Schlichting, Hermann. *Boundary-Layer Theory* (6th Edition). New York: McGraw-Hill Book Company, 1968.

32. Kuethe, Arnold M. and Chuen-Yen Chow. *Foundations of Aerodynamics* (4th Edition). New York: John Wiley and Sons, 1986.

33. Belik, L. "The Secondary Flow about Circular Cylinders Mounted Normal to a Flat Plate," *Aeronautical Quarterly,* 24: 47-54 (February 1973.

Vita

 Brett Lewis Jones was born in Visalia, CA. He graduated from Tulare Union High School in 1999 and received an appointment to the United States Naval Academy in 2000. He earned a degree in Ocean Engineering and received a Commission into the United States Navy designated a Navy pilot. After graduation in May 2004, he began his officer career at the Air Force Institute of Technology. Brett enjoys competitive sports, recreational activities, and long walks along the beach.

REPORT DOCUMENTATION PAGE			Form Approved OMB No. 074-0188

1. REPORT DATE (DD-MM-YYYY) 13 Jun 05	2. REPORT TYPE **Master's Thesis**	3. DATES COVERED (From – To) 28 JUN 04 – 26 MAY 05

4. TITLE AND SUBTITLE	5a. CONTRACT NUMBER
Experimental Investigation Into the Aerodynamic Ground Effect of a Tailless Chevron-shaped UCAV	5b. GRANT NUMBER
	5c. PROGRAM ELEMENT NUMBER

6. AUTHOR(S)	5d. PROJECT NUMBER
JONES, BRETT L., Ensign, USNR	5e. TASK NUMBER
	5f. WORK UNIT NUMBER

7. PERFORMING ORGANIZATION NAMES(S) AND ADDRESS(S) Air Force Institute of Technology Graduate School of Engineering and Management (AFIT/EN) 2950 Hobson Way WPAFB OH 45433-7765	8. PERFORMING ORGANIZATION REPORT NUMBER AFIT/GAE/ENY/05-J04

9. SPONSORING/MONITORING AGENCY NAME(S) AND ADDRESS(ES) AFRL/VAAA Attn: Mr. Dieter Multhopp 3550 Aberdeen Rd. SE WPAFB OH 45433 DSN: 246-2871	10. SPONSOR/MONITOR'S ACRONYM(S)
	11. SPONSOR/MONITOR'S REPORT NUMBER(S)

12. DISTRIBUTION/AVAILABILITY STATEMENT APPROVED FOR PUBLIC RELEASE; DISTRIBUTION UNLIMITED.

13. SUPPLEMENTARY NOTES

14. ABSTRACT This experimental study adequately identified the ground effect region of an unmanned combat air vehicle (UCAV). The AFIT 3' x 3' low-speed wind tunnel and a ground plane were used to simulate the forces and moments on a UCAV model in ground effect. The chevron planform used in this study was originally tested for stability and control and the following extends the already existing database to incude ground effects. The ground plane was a flat plate mounted with cylindrindrical legs. To expand the capabilities of the AFIT 3' x 3' low-speed wind tunnel, hot-wire measurements and flow visualization revealed an adequate testing environment for the use of the ground plane. Examination of the flow through the test section indicated a significant difference in test section transducer velocity and the hot-wire measured velocity. This disparity along with the velocity difference due to the ground plane were accounted for as wind tunnel blockage. In addition, the flow visualization revealed the horseshoe vortices that built up on the front two mounted legs of the ground plane.
The ground effect region for the chevron UCAV was characterized by an increase in lift, drag, and a decrease in lift-to-drag ratio. These trends were also noted in previous studies of similar aspect ratio and wing sweep.

15. SUBJECT TERMS Ground Effect, Ground Plane Flow Analysis, Chevron UCAV

16. SECURITY CLASSIFICATION OF:			17. LIMITATION OF ABSTRACT	18. NUMBER OF PAGES	19a. NAME OF RESPONSIBLE PERSON MILTON E. FRANKE
REPORT U	ABSTRACT U	c. THIS PAGE U	UU	128	19b. TELEPHONE NUMBER (Include area code) (937) 255-6565, e-mail: MILTON.FRANKE@afit.edu

Standard Form 298 (Rev: 8-98)
Prescribed by ANSI Std. Z39-18